The Effect of Alloys, Powder, and Overhanging Geometries in Laser Powder Bed Additive Manufacturing

Submitted in partial fulfillment of the requirements for the degree of

Doctor of Philosophy

In

Mechanical Engineering

Colt James Montgomery

B.S. Mechanical Engineering, South Dakota School of Mines and Technology

M.S. Mechanical Engineering, Carnegie Mellon University

Carnegie Mellon University

Pittsburgh, PA

December 2017

Copyright © Colt Montgomery, 2017

All Rights Reserved

Acknowledgements

This thesis would not have been possible without the support from many people. Firstly, I would like to thank my advisor, Dr. Jack Beuth, for the guidance and support that he has provided throughout my time at Carnegie Mellon University (CMU). I would also like to thank my committee members, Dr. Fred Higgs III, Dr. Jonathan Malen, and Dr. Albert To; their suggestions and support have defined the work in this dissertation and my time here at CMU and in Pittsburgh. The many members of the department of Mechanical Engineering staff have been crucial to my success. I am eternally thankful for their support and for being able to work with each of them.

Financial support for this research is provided by the National Institute of Standards and Technology (2012-NIST-MSE-01), the NextManufacturing Center at Carnegie Mellon University, and the United States Department of Energy in conjunction with Oregon State University (Award Number: DE-FE0024064, Subaward: G0148A-A).

I would like to give special thanks to all of my friends that I've made during my tenure here; you've made the experience a wonderful one and have helped me leave Carnegie Mellon and Pittsburgh as a better person than when I arrived, years ago.

I would also like to particularly thank all of the current and past students of Dr. Beuth's lab group that have been present during my time at CMU: Dr. Joy Gockel, Dr. Jason Fox, Dr. Zack Francis, Dr. Sneha Narra, Daniel Christiansen, Greg LeMon, Luke Scime, Brian Fisher, Debbie Basu, and Jose Veintimilla. All of these students have helped shape my research in a meaningful way. I would also like to thank Ross Cunningham from the department of Material Science and Engineering for help with SEM and sample preparation.

Collaborators from various organizations have helped expand my understanding as well as provide valuable insight. Special acknowledgement must be made to Shawn Moylan of NIST, Luke Sheridan and Nathan Klingbeil at Wright State University (for helping with imaging of the IN625 samples), Oberg Industries, Matthews International, the machinists at the University of Pittsburgh, and Sean Goodrich of EOS-NA.

Finally I must thank Dr. Sandra DeVincent Wolf and Dr. Anthony Rollett for all of their support and guidance above and beyond what was required of them. Without you none of this work would have been possible.

Abstract

Additive manufacturing (AM) shows great promise for the manufacturing of next-generation engineering structures by enabling the production of engineered cellular structures, overhangs, and reducing waste. Melt-pool geometry prediction and control is critical for widespread implementation of laser powder bed processes due to speed and accuracy requirements. The process mapping approach used in previous work for different alloys and additive manufacturing processes is applied to the selective laser powder bed process for IN625 and 17-4 stainless steel alloys. The ability to predict the resulting steady state melt-pool geometry in terms of process parameters, specifically power and velocity, is explored in detail numerically and experimentally verified. A finite element model was created that simulates powder at the macro scale. This model correlates well with current experiments in showing that small amounts of powder relative to melt-pool depth have negligible effects on resulting geometry. Results indicate that the effect of powder may be negligible when comparing steady state widths of the no powder and one layer of powder cases. The work in this thesis investigates the effect of powder on the resulting steady-state melt-pool geometries for IN625 and 17-4 alloys. This analysis has been extended to the production of overhanging and cellular structures. The successful analysis will allow for better predictions and possible correction for cellular structure production issues as well as overhanging features.

Table of Contents

Table of Figures

Table of Tables

Nomenclature

AM – Additive Manufacturing

L-PBF - Laser powder bed fusion

A - Melt-pool cross-sectional area

D - Melt-pool depth

L - Melt-pool length

W - Melt-pool width

t - Time

S_t - Solidification time

V – Beam scan velocity

T - Temperature

α - Thermal diffusivity

ρ - Density

k – Thermal conductivity

C_p – Specific Heat

L_H – Latent Heat

ε – Void fraction

k_g – Thermal conductivity of gas

k_s – Thermal conductivity of solid

k_{eff} – Effective thermal conductivity

ψ - Effective thickness of the fluid film in the void between the particles

β - Ratio of the average distance between particle centers in the direction of heat flow to the mean diameter of packing

S – Sorptivity

G – Gravitational acceleration

L_{diff} – Thermal diffusion length

$x_{kinematic}$ - Distance traveled by the molten melt-pool due to kinematics

$x_{wicking}$ - Distance traveled by the molten melt-pool due to capillary wicking

Chapter 1 Introduction

1.1 Motivation and Applications

Additive Manufacturing (AM) of solid objects is rapidly becoming a viable mainstream manufacturing technique due to technological advances, and is being called "Industry 4.0" or a digital revolution in manufacturing due to the entirely new approach to design and production [1]. The major impediment to wide spread adoption of the technology can be attributed to a lack of understanding of the process capabilities and of the resulting properties. The motivation for this research is to better understand the process capabilities, and attempt to expand them by varying process parameters, as well as to better understand the resulting part properties of AM produced parts.

Applications for this research include (1) an improved understanding of the effect of powder in the laser powder bed fusion (L-PBF) process, (2) the ability to make larger unsupported overhanging features with a better surface finish, and (3) the ability to tailor deposition parameters to a desired outcome, in particular higher geometric tolerance or deposition rate. These results have applications for faster part qualification, production of wave-guides, heat exchangers, and other complex geometry with internal features requires the knowledge of how to produce unsupported structures.

1.2 Additive Manufacturing

Additive Manufacturing, colloquially known as "3-D Printing," is a manufacturing technique that builds parts by adding material in 2-dimensional layers to produce a finished 3-dimensional part. This is in stark contrast to traditional subtractive manufacturing, which removes material to create a final geometry. AM is inherently a less wasteful process than conventional manufacturing because of the use of only required material [2]. The layer-by-layer approach also lends itself to creating complex geometries, both external and internal, that may be difficult or impossible to manufacture by traditional means without incurring additional cost [3]. These unique attributes make AM well suited for the aerospace, biomedical, energy, and automotive industries [4]. This thesis is focused on the direct metal additive manufacturing processes (i.e. powder bed fusion, powder stream, and wire feed), the laser powder bed fusion process, in particular, although there are other types of AM for both metal and polymers currently available on the market.

Powder bed fusion (PBF) is classified into two types and differs mainly in the heat source, either an electron beam (EBM, EBAM or EB-PBF) or a laser (DMLS, SLM, L-PBF). Since this thesis is focused on the laser based processes the operation of these systems will be discussed here in detail. The process begins with a 3-dimensional data file generated in a computer aided design (CAD) package or scanned via a 3-D measurement system. This file is then sliced into 2-D layers, usually between 20-60 μm thick. These sliced files are then submitted to control software to have path planning for the laser done before being uploaded to the machine. Once a job is programmed the build chamber is purged with an inert gas, such as argon or nitrogen. The inert gases help reduce oxidation and work as a shield gas. While this is happening, the building platform is being preheated to between 30-200 °C which is done to help reduce residual stresses. The next step is to spread a single layer of powder across the build plate. This is done by lowering the building platform by one layer thickness and having the recoater blade (or roller) sweep powder from a dispenser (or hopper) across the build plate. Excess powder is collected in a bin known as a collector on the other side of the build platform. Once this is complete the laser scans the programmed path, and thus melts a 2-D cross-section of the part being printed. This process is repeated until the entire part has been deposited. The part is then uncovered from the unexposed powder and is complete. A labeled image of the process chamber for the EOS M290 can be seen in Figure 1 and a diagram of the process workflow can be seen in Figure 2.

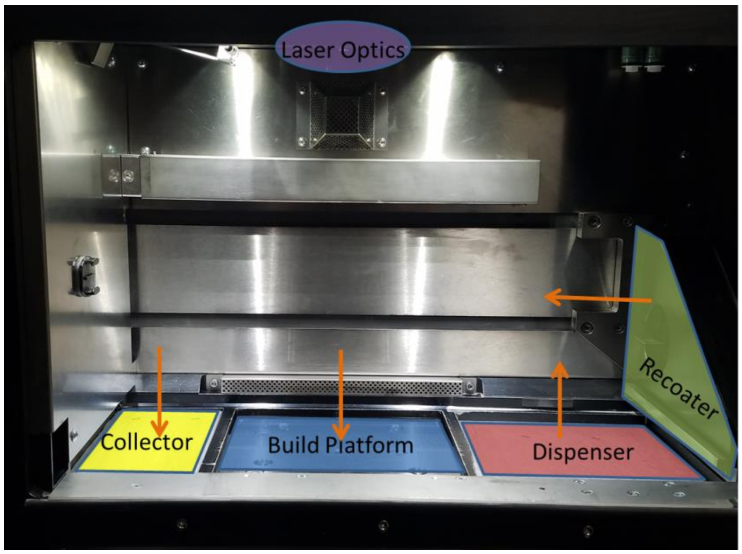

Figure 1: EOS M290 process chamber

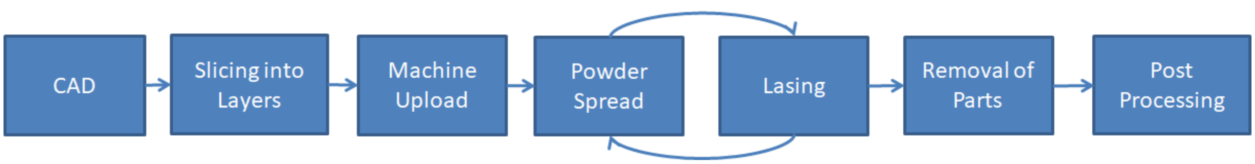

Figure 2: EOS L-PBF process workflow

In comparison, the electron beam melting (EBM) process is very similar in operation to the laser powder bed fusion (L-PBF) process with a few key differences. In EBM the process is performed under vacuum and with a sintering step that preheats the powder to higher temperatures (around and above 750 °C). This preheating step is intended to remove residual stresses as well as to increase the effective electrical conductivity of the powder to avoid charging the powder bed when doing the melting pass. The EBM process is generally faster, however the layer thicknesses and powder diameters are larger so therefore the surface roughness is usually higher when compared to L-PBF. The L-PBF process has many alloys available to it from the manufacturers, including steels, titanium alloys, aluminum alloys, and nickel alloys, this is in stark contrast with the EBM process that only currently has a few alloys available to it although there are more in development [5] [6]. EBM has unique challenges in alloy development due to the need to be electrically as well as thermally conductive, while L-PBF materials must only be able to absorb the incident laser radiation provided by the laser source in sufficient amounts to melt.

Other direct metal processes include powder stream and wire feed systems. These systems are faster in overall build time since their deposition rate is much higher, compared to the previously discussed EBM and L-PBF systems, due to the higher powers, however usually require more post-processing to get a final part. These processes either use a wire or stream of powder that is directly struck by the heat source. These systems allow for repair work on existing parts as well as larger parts since less material is required than with a powder bed system [7] [8]. There is also work in development of layer based exposure techniques at Lawrence Livermore National Laboratory (LLNL) [9]. An example of the regions of processing space that each direct metal process operates in can be seen in Figure 3 with the L-PBF region highlighted in red.

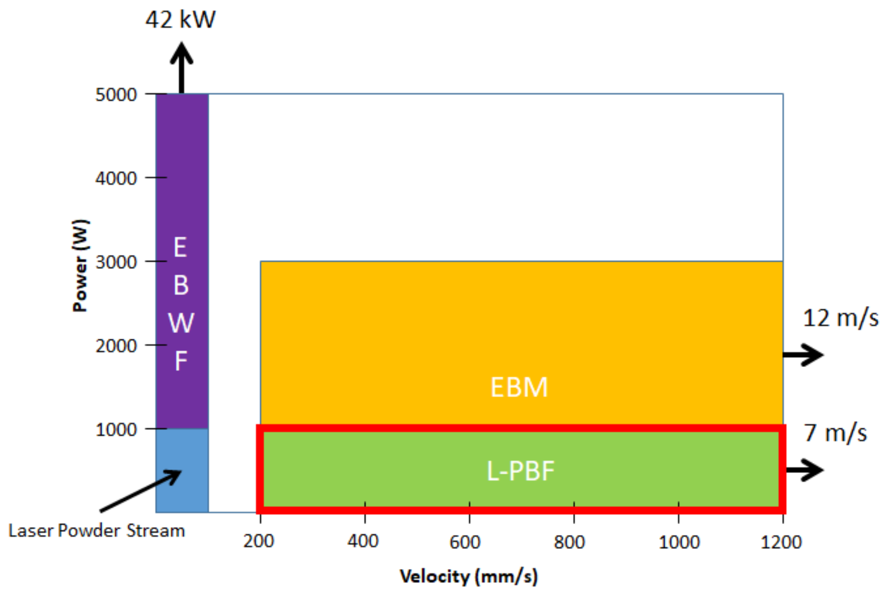

Figure 3: Different direct metal processes and their regions of Power-Velocity space

1.3 Materials

Many materials are currently available for the L-PBF process but the work in this thesis is focused on two alloys of particular interest for additive applications, Inconel 625 and 17-4 Stainless Steel.

1.3.1 Inconel 625

Inconel Alloy 625 (IN625) is an engineered Nickel-Chrome superalloy with high strength, high corrosion resistance, and considerable fatigue resistance [10]. These properties make IN625 an excellent candidate for marine and nuclear applications where corrosion is of major concern. IN625 maintains these properties over a wide range of temperatures, making it suitable for aerospace applications and chemical plants [10]. Conventional machining has difficulty in processing IN625 because of excessive wear on the tooling and slow material removal rates, from the extreme strain hardening that occurs when processing this material. These factors make it an ideal candidate for AM technologies [11] [12]

1.3.2 17-4 Stainless Steel

17-4 stainless steel, also known as GP-1 Steel in the EOS system, is a martensitic precipitation hardened stainless steel. This is a general purpose steel ideally suited for applications where high ductility and toughness are required. Traditional uses for this alloy are in the aerospace, petrochemical, and food processing industries [5] [13]. Understanding steels such as 17-4 help give mainstream appeal to AM technologies for building functional prototypes.

1.4 Literature Review

1.4.1 Process Parameter Effects

There are a variety of process parameters to consider during any AM process, and choosing the proper parameters can be the difference between a successful and failed part. The parameters include heat source power, travel velocity of the heat or deposition source, layer thickness (or feed rate), preheat or background temperature, scan strategy, support structures, and feature geometry. These parameters affect microstructure, melt-pool geometry, residual stress, flaw formation, deposition rate, surface finish, density, and ability to build a part [14].

Residual stress can be affected by varying process parameters. It has been found that by changing the dwell time between layers IN625 and Ti-6Al-4V alloys can have reduced residual stresses [15]. Residual stresses can also be reduced by manipulating scan strategy [16] [17]. Similar to other processing parameters, scan strategy can also influence density of the resulting part [18].

Process mapping is an approach developed by Beuth et al. [19] to illustrate the process outcomes of an AM process based on process input parameters. These parameters are often conveniently displayed as two independent variables, power and velocity (P-V), while the other variables such as preheat temperature, feed rate (or layer thickness), and feature geometry remain fixed [19], with the resulting outcome of these parameters shown on the resulting 2-D plot. Commonly plotted are curves of constant cross-sectional area which show what power and velocity combinations will result in similar melt-pool cross-sectional areas for a given process, Figure 4 shows an example plot along with example curves of constant length to depth (L/D) ratio. The process mapping approach has been applied to geometry control [19] [20] [21] [22] [23], microstructure control [24] [25] [26] [27] [28], and transient response [29] [30] [31]. An optimization framework for determining optimal processing parameters to get desired features based on fundamental equations has been developed by Clymer et al. [32].

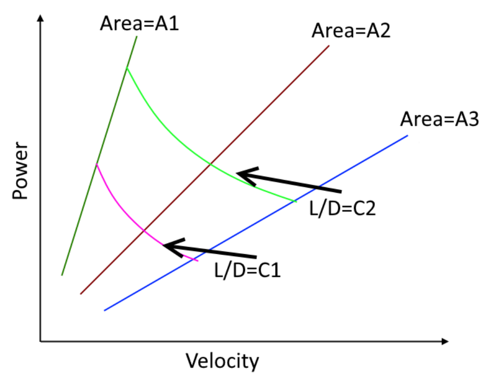

Figure 4: Example P-V plot of curves of constant area and L/D ratio

1.4.2 Microstructure Control

Understanding the microstructure produced by AM is critical to the practical application in parts due to mechanical requirements. Microstructure controls the properties of the resulting part, from toughness, to strength, to magnetic properties. Extensive research has been done at present into the effects of processing parameters on microstructural development for Ti-6Al-4V. Kobryn et al. investigated the correlation between power and velocity to grain size [33] [34]. Bontha et al. investigated the process parameter effects on thermal gradients and cooling rates and used them to determine grain morphology [28] [35] [36]. Gockel investigated the relationship between process parameters and microstructure production in AM produced Ti-6Al-4V in the Arcam and Sciaky processes [37]. Narra et al. utilized processing parameters to control microstructural evolution in different regions of an AM produced part [38] [39]. Carter et al. were able to affect the crystallographic orientation by manipulation of the scan strategy in the SLM process [40]. Although only basic microstructural observations are made throughout this work it is important to know that there is extensive work being done to characterize this aspect of AM produced parts.

1.4.3 Modeling

Many of the additive processes are akin to welding; as such most analytical models have been applied welding models. Rosenthal et al. derived an analytical moving point source model that was then non-dimensionalized by Vasinota et al. [41] [23]. This solution was first applied to AM by Dykhuizen and Dobranich for the powder feed laser deposition process [42] [43]. Eagar and Tsai were able to modify the Rosenthal solution to account for a Gaussian heat distribution, which is most commonly associated with real world lasers, using superposition of solutions [44]. These models are all limited in that they assume constant thermophysical properties and a constant temperature substrate, which is not the case in a powder bed system.

The application of the finite element method has refined the ability to simulate AM processes. Michaleris simulated the LENS process to determine the thermal and residual stress fields [45]. Residual stress was modeled analytically and tested experimentally by Mercelis et al. [46]. Residual stress control through preheating was investigated by Aggarangsi et al. [47].

Roberts et al. simulated the powder bed process for the temperature field after powder layer addition using an element birth and death method [48]. Modeling has been done to simulate the microstructural growth of AM produced alloys. IN718 microstructural evolution in the laser cladding process was investigated by Nie et al. using a finite element model [49]. Kelly simulated the alpha growth in Ti-6Al-4V due to the cyclic heating in the LENS process [50]. Microstructural evolution in AM has been simulated by a number of other groups [51] [52] [53] [54] [55] [56].

A number of models considering powder effects have been developed to simulate laser processing on a powder bed [57] [58] [59] [60] [61]. Lawrence Livermore National Laboratory (LLNL) developed code to simulate the local effects of the melt-pool, such as balling and splattering [61] [62], however, these models are often unwieldy and require extensive computational power to run. Single track formation and resulting melt-pool instabilities have been studied by Yadroitsev et al. [63].

Radiation and convection were found to be negligible compared to conduction mode heat transfer with temperatures less than 3000 K; even at these elevated temperatures and being in the LENS process, which has a large amount of convection by nature of the process, conduction still dominates with 80% of the power dissipation [64] [65]. King et al. found that the majority of the power absorption happens at or near the surface and hence a volumetric power distribution is not required for modeling many phenomena and was utilized in the models presented in this work [61].

1.4.4 Powdered Metals in AM

Research has been done on how powder morphology affects part quality in AM. Traditionally gas atomized (GA) powders are used in the DMLS process due to the uniform spherical shape that is produced. Water atomized powders result in irregularly shaped plates however this was found to increase density and vertical surface finish quality due to changing the melting characteristics via different residual elements from the manufacturing process [66] [67]. Gan et al. found that powder morphology also can affect the effective thermal conductivity, although for fine particles this was less prominent [68]. All of the work presented in this thesis was performed with GA produced powders, but it is important to note that the powder manufacturing method plays a key role in resulting surface quality and part density. Recycling of powder has an effect on particle size distribution which can also affect part quality [69].

The thermal properties of metal powders are important to understand in order to anticipate how that material will react in an AM process since thermal control of the powder bed has a strong influence on part quality and dimensional tolerances. There has been very little research investigating the thermal properties of metal powders in relation to AM at this time so other metallic powder thermal investigations are used to draw insight into the characteristics of the powders for AM. There is internal work being done at Carnegie Mellon University (CMU) to investigate thermal conductivity of AM specific powders [70].

The thermal properties of metal powders have been investigated experimentally and a number of analytical models have been proposed [71] [72] [73] [74] [75] [76] [77] [78] [79] [80]. Most of these models are not universally accurate at the size scales under investigation when compared to experimental results. The best models appear to still be off by 30% at the current time [76] [77].

The powder model implemented in this work is based off of the model proposed by Yagi et al. and is a theoretically derived effective medium model [71]. This is based off of fundamental assumptions and heat transfer mechanisms and verified with experimental results for a number of different powdered metals. The group came to the conclusion that the gas will dominate the conductivity of the multi-phase system and thus the model is heavily dependent on the thermal conductivity of the gas used.

Laser interaction with powders is different from interaction with a bulk substrate. The presence of powder creates voids and a rougher surface, so is seen by the laser as a diffuse body. Multiple reflections result in a higher penetration depth of the laser than expected from bulk material and result in an effectively higher absorptivity of the beam when compared to beam on a bulk surface [81] [82].

1.4.5 Overhanging Structures

AM allows for the potential production of internal overhanging structures and complex cellular lattices that cannot be produced through any traditional manufacturing method, however in reality there are limits to the size and angles of the overhanging structures when produced without support [83]. LLNL investigated the effect of powder on overhangs and the resulting “dross” structure [61] [60]. Dross is defined as an undesired sagging of the overhanging surface resulting from overpenetration, melt-pool motion, and adhesion of powder particles. Calignano et al. experimentally found the limits of construction of overhanging structures without supporting material in the DMLS process [84]. Work by Wang et al. was done to experimentally help choose best process parameters for 316 stainless steel overhangs in the SLM process space [85]. The surface roughness of overhanging structures was examined and a model was developed by Strano et al. [86]. It has been found by Thijs et al. that a surface roughness height variation greater than twice the layer thickness create pores and thus affect mechanical properties [87]. Surface roughness has been initially evaluated with respect to processing parameters by Fox et al. but work is ongoing to determine what the correlation is [88]. There has been little work done on attempting to increase the unsupported build distance and thus allow for a broader range of complex engineering designs with internal cavities, which is what this work focused on.

1.4.6 Cellular Lattice Structures

Cellular lattices are a useful engineering structure that can be utilized to reduce weight and increase functionality while maintaining strength. Stochastic lattices and foams are easily created using traditional casting processes by injecting air or a foaming agent into the molten metal [89] [90]. These foams are useful for heat exchangers and other high surface area applications, however to be useful for many engineering applications an ordered lattice is needed to achieve the required strength. Additive manufacturing gives a design freedom that has never been available to engineers in the past and has only been theorized. The application of additively manufactured cellular structures has been studied by various groups [91] [92] [93]. Zhang et al. experimentally analyzed the effect of angle of the struts and processing parameters on the manufacture of titanium struts [94]. Hussein investigated the effect of volume fraction and cell sizing of cellular structures but did not examine the effect of modifying process parameters in order to correct defects [91]. Currently there are limitations as to the size of lattices that are able to be produced successfully. A number of studies have found an upper limit of approximately 5 mm unit cell size (these are strut lengths of approximately 5 mm for the truss geometry discussed) before sagging begins to occur within the struts and a lower limit of approximately 3 mm (in a gyroid structure) before over-melting occurs or powder gets trapped inside the lattice due to the large cross-section of the struts [95] [96] [97]. Currently the lasing parameters are not adjusted for cellular lattice structures, but optimizing parameters for this could allow easier creation of a variety of lattice sizes which is the focus of this work.

1.5 Contributions

This work focuses on extending the existing knowledge of the effect of process parameters on AM produced parts. The major contributions of this thesis are:

1. In this work, melt-pool geometry control is examined for both Inconel 625 and 17-4 stainless steel. An end user can use this knowledge to manipulate process parameters to produce parts with less porosity, faster deposition rates, and potentially higher as-built tolerances.
2. A design methodology is proposed and implemented to develop new alloy processing parameters for the L-PBF process using the process mapping approach. Using this methodology, development of processing parameters for candidate AM alloys can be streamlined.
3. The existence of a varying effective absorptivity within the process space is investigated and proven. A varying effective absorptivity provides a better correlation between simulations and experiments, further reducing the need for experimentation.
4. A faster alloy development process is investigated to further reduce parameter development time.

5. The effect of layer thickness on resulting melt-pool geometry is analyzed and a simple powder simulation code has been proposed and implemented. Knowing the nominal melt-pool geometry an end user can quickly transition to another layer thickness and thus increase deposition rates further.
6. The application of the effects of powder is analyzed in relation to overhanging and cellular structures in order to determine a viable processing window for producing these geometries.

1.6 Organization

This thesis is divided into six chapters. The first chapter consists of an introduction into the background of additive manufacturing, applications, and the process mapping approach, as well as various modeling approaches and powder literature. A comprehensive literature review of relevant research is performed and the importance of the work done for this dissertation is demonstrated.

The second chapter is focused on process mapping of melt-pool geometry of IN625 in the L-PBF process. Finite element models are used to predict melt-pool geometries and create process maps. Models with the addition of 20 µm of powder are illustrated as well. Experiments are preformed to validate the models and compared by using an effective absorptivity. The effect of a single layer of powder of IN625 is discussed.

The third chapter is concentrated on process mapping of melt-pool geometry of 17-4 stainless steel in the L-PBF process. Finite element models are again created and used to predict melt-pool geometries and create process maps with and without 20 µm of added powder. Experiments are preformed and an attempt is made to circumvent the single layer pad geometry and move directly to bulk geometry from single bead results. The models are validated similarly to those for IN625 using an effective absorptivity and the powder effect of a single layer of 17-4 is discussed.

The fourth chapter is on the effects of powder on the melt-pool geometry of IN625 produced in L-PBF. Finite element models are used to determine when the layer thickness of powder starts to have an effect on melt-pool geometry. A series of experiments are performed to validate the model and see what the layer thickness effect is on single bead geometries.

The fifth chapter is the application of the knowledge from the powder work in the previous chapters to overhanging and cellular lattice structures. Internal overhangs which cannot be supported due to difficulty in removal of additional structures are examined in three configurations. The first configuration is a two point “bridge” style structure. A detailed simulation is run to better understand the development of the melt-pool area for these partially free structures. The second configuration is an enclosed structure supported from 4 sides. The final configuration is a circular hole that is capped. A method to produce the structures is determined and discussed along with implications for surface finish.

The sixth and final chapter summarizes the conclusions found throughout this work. Major contributions are highlighted and future work recommendations are made.

Chapter 2 Process Mapping IN625

2.1 Overview

This chapter explores the process mapping of geometry and basic microstructural analysis of IN625 produced via L-PBF. Knowledge of the effect of process parameters on the resulting geometry and melt quality is critical to being able to properly produce a part with minimal porosity, higher deposition rates, and/or achieving high tolerances [14]. Even when using standard parameter sets given by the manufacturer, knowing the melt geometry can provide insight into the feature sizes and flaws that can realistically occur.

A methodology is proposed and implemented within this chapter to quickly map melt-pool geometry for a new alloy system by progressing from single bead depositions to bulk parts. A finite element model was developed for use throughout this work to predict and better understand the thermal conditions that are occurring during and after deposition. The addition of a single layer of powder is examined in relation to beam on plate experiments and conclusions about the effects of powder are drawn.

2.2 Methods

2.2.1 Finite Element Models

Finite element models were designed to run in the commercial finite element package Abaqus FEA by Dassault Systems to simulate the AM heat transfer process. In general, the model is used for single bead deposition however the model is able to simulate raster patterns. The model is based on works by Soylemez and updated by Fox [98] [31]. The author has updated these models further to include the ability to implement radiation and convection as well as to improve the application of heat flux. Finite element models have the advantage over analytical models such as Rosenthal because of the ability to simply incorporate distributed heat sources, latent heat, and temperature dependent thermophysical properties as well as easily simulate various scan patterns. The temperature dependent properties used here are density, specific heat, and thermal conductivity.

The models used in this research are 3D transient heat transfer models and include a circular distributed heat flux, in a top-hat distribution, although a Gaussian distribution would be more faithful to many of the DMLS processes. A Gaussian distribution would likely result in higher temperatures along the centerline of the beam path due to a higher power density. Research appears to show that the melted area is not drastically changed with different beam profiles; however a Gaussian beam can have slightly more penetration due to aforementioned higher power density [99]. A representative model can be seen in Figure 5. The model simulates a preheated build plate by initializing all nodes to the preheat temperature (80 °C for the alloys under investigation in this thesis) and holding the nodes on the bottom face of the model at a constant temperature using boundary conditions. The nodes on the upper surface can be set to a radiation or convection boundary condition if desired. All the remaining nodes on external faces are set to an adiabatic boundary condition.

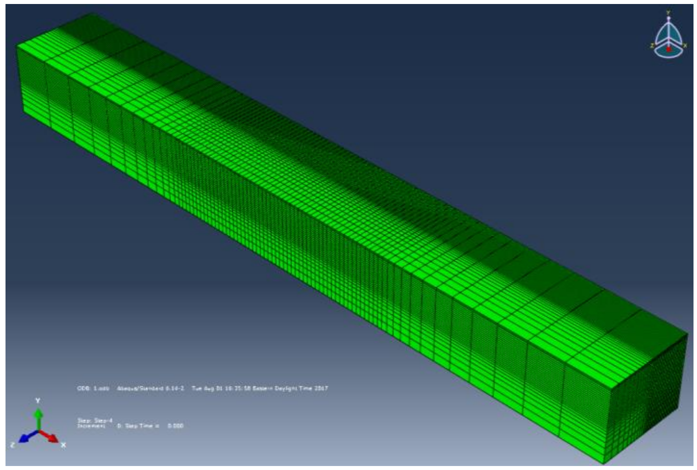

Figure 5: Finite element model used for melt-pool simulation

The geometry of the model is a simple box with biased mesh regions and a fine mesh region. The biased regions are included to eliminate edge effects for the model and to accurately model a steady state melt-pool. The model simulates the laser by moving a distributed heat flux along the x-direction. The flux is applied for a time determined by the velocity and element size and then advanced to the next set of elements in the next computational step. For single bead simulations this is stepped through the biased region and through the fine region before being terminated. The steady state melt-pool geometry is then determined from the melt-pool dimensions within this fine mesh region. When single beads are being simulated a symmetry condition is used to reduce the computation time.

Key dimensions that are often measured include the melted depth of the melt-pool (D), melt-pool length (L), and melt-pool width (W). An example of a simulated melt-pool with labeled dimensions is shown in Figure 6. Most of the work presented here is in terms of melt-pool cross-sectional area (A) perpendicular to beam travel direction (Figure 7). It should be noted that when the symmetry boundary condition is being used the half width is measured rather than the full width and this value is doubled to obtain the full width.

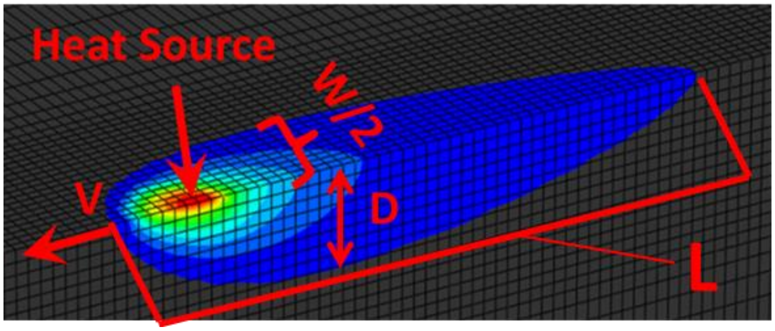

Figure 6: Relevant melt-pool dimensions

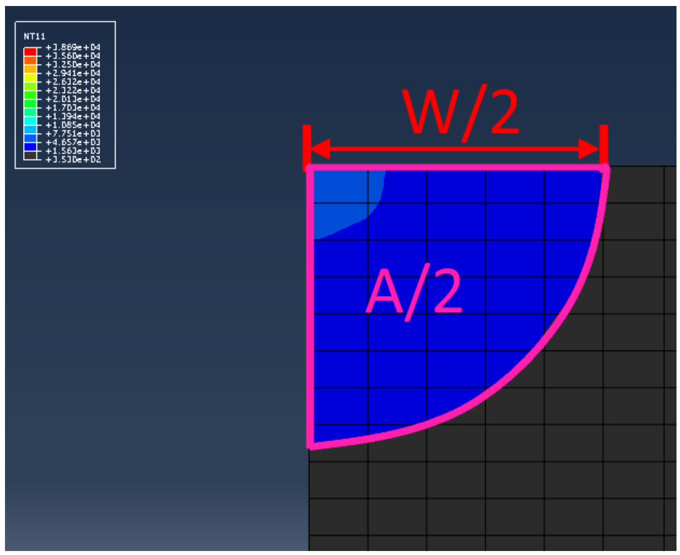

Figure 7: Cross-sectional area example

The finite element solution is, at its core, solving a fundamental energy balance problem. The solution is based on the heat equation (Equation 1). The model developed includes latent heat, so the equation becomes Equation 2 to account for this energy loss. The boundary conditions that are relevant for solving these equations are presented in Equation 3, Equation 4, and Equation 5.

Equation 1: Heat Equation

$$\frac{\partial}{\partial x}\left(k(T)\frac{\partial T}{\partial x}\right)+\frac{\partial}{\partial y}\left(k(T)\frac{\partial T}{\partial y}\right)+\frac{\partial}{\partial z}\left(k(T)\frac{\partial T}{\partial z}\right)=\rho(T)c_p(T)\frac{\partial T}{\partial t}$$

Equation 2: Heat Equation including latent heat

$$\frac{\partial}{\partial x}\left(k(T)\frac{\partial T}{\partial x}\right)+\frac{\partial}{\partial y}\left(k(T)\frac{\partial T}{\partial y}\right)+\frac{\partial}{\partial z}\left(k(T)\frac{\partial T}{\partial z}\right)=\rho(T)c_p(T)\frac{\partial T}{\partial t}+\rho(T)L_H$$

Equation 3: Insulated/Symmetry boundary condition

$$\frac{\partial T}{\partial x}=0$$

Equation 4: Flux boundary Condition

$$q=P$$

Equation 5: Constant temperature boundary condition

$$T_{base}=T_{preheat}$$

Where equations k(T), ρ(T), and $C_p(T)$ are the temperature dependent thermal conductivity, density, and specific heat, respectively. $T_{preheat}$ is the preheat temperature and P is the input power in W/m^2.

To solve these equations Abaqus FEA discretizes the equations based on the meshing. A DC3D8 type element is used, which simplifies the equations since hexahedral elements are less computationally expensive when compared to tetrahedral or mixed elements. Abaqus FEA uses a backward difference numerical scheme in the time domain, chosen because of the simplicity in implementation. This method is conditionally stable, but is typically preferred for long time periods because of the stability compared to the central difference method [100]. The resulting system of equations is solved using a modified Newton method [100].

To examine powder effects a powder material model is also created. The powder model is implemented by using the same base model as the no powder model but with key material differences. The powder model uses the theoretical model derived by Yagi and Kunii from fundamental heat transfer aspects of the powder problem. These heat transfer aspects are: conduction through the solid and the contact surface between particles, radiation between particles, radiation between voids, conduction through the fluid film, and convection between the fluid and particles [71].

For this application to the AM process, since the powder diameters are fine and the fluid is motionless in the L-PBF process within the powder-bed, the equation used simplifies to Equation 6.

Equation 6: Yagi-Kunii effective conductivity of powder

$$\frac{k_{eff}}{k_g} = ß\frac{1-\varepsilon}{\frac{k_g}{k_s}+\psi}$$

Where ß is the ratio of the average distance between particle centers in the direction of heat flow to the mean diameter of packing, and for practical purposes ß is assumed to be unity for this problem. ε is the void fraction of the powder, in our case around 0.5-0.6 [69] [101]; k_s is the conductivity of the solid bulk material; k_g is the conductivity of the fluid between the particles; and ψ is the effective thickness of the fluid film in the void between the particles. This can be derived from experimental results or from theoretical models, for the work presented, the relationship for ψ used is that presented by Bugeda et al. of $\psi = 0.02 \times 10^{2\left(0.7-\frac{\rho p}{\rho s}\right)}$ [102]. While this model is not the most accurate, it is one of the fundamental equations for high temperature powder conductivity found in literature that most other models compare themselves to. This is still a topic under research and as newer models are being developed these can be easily implemented into the framework that the author has produced. These different models will change the behavior slightly but the overall trends should remain the same. Likely the overall increase in dimensions from the powder will decrease with a more accurate high temperature powder model.

For the powder model, the program flows in a way such that each step is completed and then a macro analyzes the temperature field and exports all elements with nodes that are greater than the melting temperature of the alloy under investigation. This list of elements is then exchanged for elements that have the bulk material thermal properties and the original elements deactivated. The temperature field, being nodal, is unchanged at the beginning of the next step. This process repeats until the model is complete.

In order to conserve mass the model does not use a different temperature dependent density while using the same mesh that was used for the powder and no powder elements. Instead, the density discrepancy is accounted for by instead modifying the thermal conductivity of the powder, by scaling the value based on packing factor, to account for a larger thickness than is being shown in the mesh. This allows for a mathematical compensation instead of a physical one. A packing factor of approximately 0.5 was used for the powder, in literature the packing is usually considered a random packing and to be approximately 0.55-0.6, so this is a conservative value [69].

The model for the powder assumes a half thickness for the powder layers compensated for by scaling the thermal conductivity. This approximation can potentially cause issues with radial heat spreading for certain cases such as extremely thick powder layers or overhanging geometries. To ensure that radial spreading was not an issue for most scenarios, a set of simulations were run to compare the temperature field of the approximation and the actual properties under the spot size below melting temperature. The results show that the average temperatures below the beam spot are the same so this approximation should be valid for most cases.

Radial heat spreading shouldn't be a major issue except during initial melting steps in a simulation because of the conversion to solid material. This radial heat spreading concern could affect the thermal lead on the melt-pool. To quantify this effect it should be investigated further in future work. Issues can also arise when looking at overhanging structures, because of the lack of solid substrate to dominate the heat transfer. However, since the material being examined is all above the melting temperature the heat path should be predominantly in the direction of the solid material in these cases as well. These models would need to be modified to look at any temperature fields below melting temperature in the powder region of the part.

The powder model convergence was tested to confirm the minimum number of elements across the melt-pool width to reach a steady state solution. The results of this convergence study indicate that with 9 elements across the melt-pool width the solution is within 2% of the final values for melted area and width.

To verify the effects of radiation and convection are negligible, a series of simulations were run incorporating various convective coefficients with and without radiation. The parameters tested along with the results can be seen in Table 1. This brief study verified that the model going forward would not need to include either of these effects as they were both minimal. Radiation did have a slightly larger effect but this is due to the higher order of the equation. For the sake of completeness, unless otherwise noted, the models presented in this work implemented the radiation and convection effects with a radiative emissivity of $\varepsilon = 0.5$ and convection coefficient of h = 10 W m^{-2} K^{-1}, even though the difference was not substantial in terms of melt-pool geometry.

Table 1: Effects of radiation and convection on model

Power (W)	Velocity (mm/s)	Powder Layer Thickness (μm)	Radiation Emissivity (ε)	Convection h (W / (m² K))	Area (m²)	Width (m)	Depth (m)	Full Length (m)
40	822.8	20	0	0	2.602E-09	1.005E-04	3.473E-05	3.608E-04
40	822.8	20	0.5	0	2.594E-09	1.005E-04	3.460E-05	3.588E-04
40	822.8	20	0.5	10	2.594E-09	1.005E-04	3.460E-05	3.588E-04
40	822.8	20	0.5	100	2.593E-09	1.005E-04	3.460E-05	3.587E-04

2.2.2 Experimental Design and Measurement

Single bead process mapping for the IN625 samples was performed to cover the entire available process space for the EOS M270 at the National Institute for Standards and Technology (NIST) in September of 2013. The M270 is a piece of L-PBF equipment that operates at up to 200 W and 7 m/s, although these speeds are often too fast to be useful for deposition and are not commonly used. For these tests the process space examined was from 50-195 W and 200-1200 mm/s, in 25 W and 200 mm/s increments, respectively, resulting in 42 different power and velocity combinations, throughout process space. Note that 42 combinations are more than are strictly needed, however this adds more data points for a smoother data fit, as well as assurance if a parameter was not input correctly into the software.

The experiments were performed on surface-ground 5” by 5” by ½” IN625 plates that were affixed to the build plate and then leveled and brought to a zero layer thickness height. Using a modified plate allows for quick experimental changeover, analysis, and easier material handling than using an entire standard build plate for every experiment. The leveling and zeroing procedure for the EOS M series equipment is discussed here. The first step to establish a level is to run a dial indicator along the ground rail on the recoater arm and adjust x and y levels until the indicator does not deviate as the recoater moves left to right as well from front to back. Once a level surface is achieved (this assumes your plate is perfectly flat, which for such a large plate is an optimistic assumption at best), the gapping procedure can begin. To set the zero, or “gap”, the build plate and establish an initial powder layer feeler gauges are used. A gauge is slid between the recoater blade and the build platform and the largest gauge size that fits is determined. Once this gauge is found the build platform is raised up in small (i.e. <10 µm) increments until the gauge is tight but can still slide the length of the recoater blade. The recoater is then moved out of the way and the building platform raised the height of the feeler gauge thickness. This new position is “zero” and when starting a build with powder the platform is then lowered one layer thickness (20 µm in this case) and a layer of powder is spread across. The use of feeler gauges makes the process hard to quantify the error in gapping, so often the build plate is “scratched” at the zero position to be confident that a near zero is actually achieved.

The parameters chosen can be seen in Figure 8 and an example experimental plate can be seen in Figure 9. The experiments were performed with no added powder (build height = 0 µm) and with one 20 µm layer of added powder (build height = 20 µm).

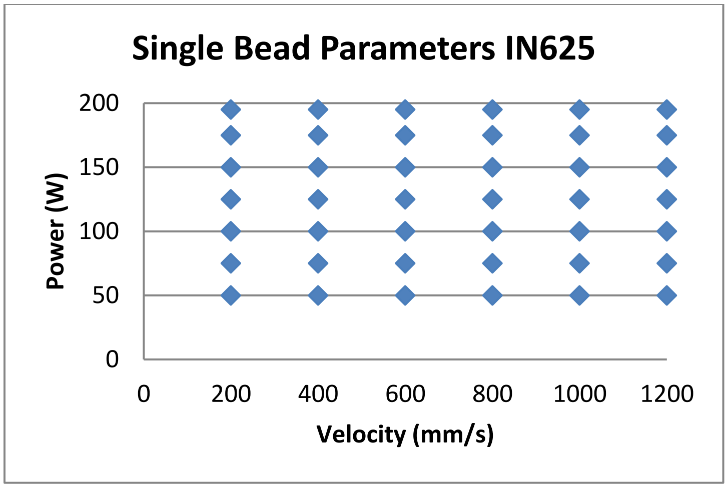

Figure 8: Single bead experiment parameters for IN625

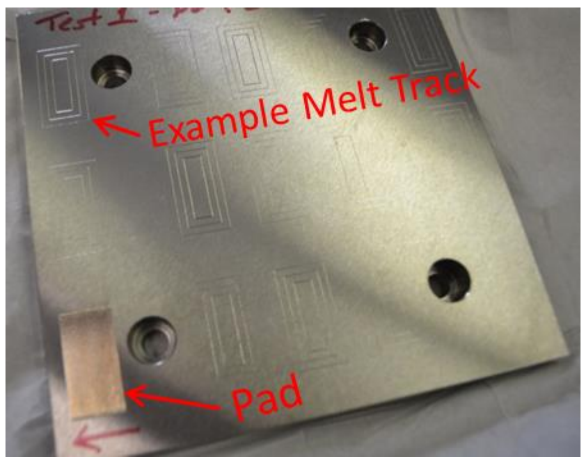

Figure 9: Single bead experimental plate

In order to produce many single bead melt-pool tracks the contour parameters were used, this allowed many tests to be performed with minimal geometry creation. The geometry was created to be 25.4 mm (1.0 in) by 12.7 mm (0.5 in) and the contour was lased around this geometry, with no "skin" (raster) parameters. The experimental layout can be seen in Figure 10, with the exposure orders labeled. Each subsequent contour was offset from the previous contour by 2 mm to avoid affecting neighboring melt-pools with heat buildup. At the time these experiments were run no experiments were done by the author or the author's group on the EOS system so this was a conservative estimate.

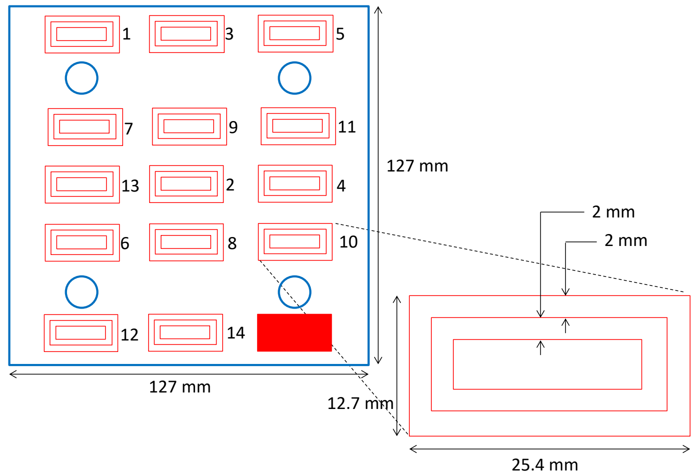

Figure 10: Single bead experiment layout IN625

The resulting experiments were then imaged using a Zeiss Axiovision AX10 light optical microscope and then analyzed for width data and melt-pool issues with ImageJ. Fifteen measurements were taken along the melt-pool path and averaged to determine the width from above (Figure 11).

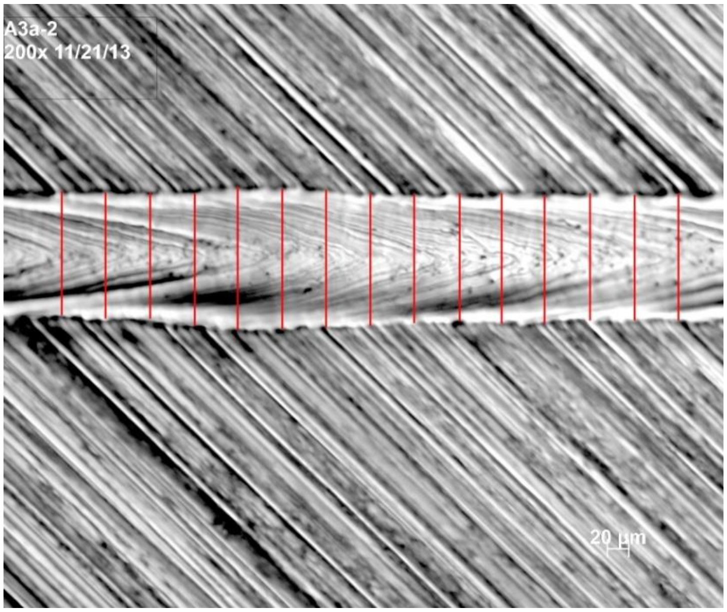

Figure 11: Example measurement points on above view micrograph

After above view information was gathered the samples were cross-sectioned perpendicular to the laser travel direction using wire-cut electrical discharge machining (EDM) and then ground and polished according to recommendations by Buehler on an EcoMet 250 Autopolisher, the polishing procedure is noted in Appendix A. These samples were then imaged using Scanning Electron Microscopy (SEM) (Quanta 200) for cross-sectional information. ImageJ was again used to take cross-sectional measurements. A representative image with points of interest marked can be seen in Figure 12. The reason SEM was used for these samples was because of difficulty in etching the highly corrosion resistant nickel alloy using traditional chemical etching techniques, at a later time an electroetching procedure was determined that was extremely effective.

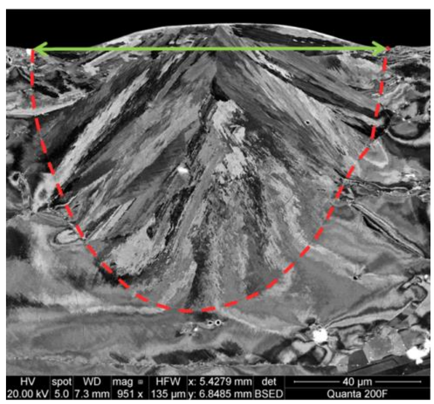

Figure 12: SEM cross-section of IN625 melt-pool, width is marked in green, area in red.

Since the current measurement method relies on human tracing of the melt-pool there is a certain amount of uncertainty in each measurement. A raw image of the melt-pool cross-section can be seen in Figure 13. The melt-pool boundary (approximately 1.2 µm thick) is highlighted between the green bounding box and this is where the measurement is taken (note that the boundary box is made larger than actual measurement error for ease of viewing). The human factor can result in a measurement error of approximately 1.1% based on the max difference in measured area from 10 different measurements of various images across process space. This measurement error is similar in magnitude for the 17-4 samples as well.

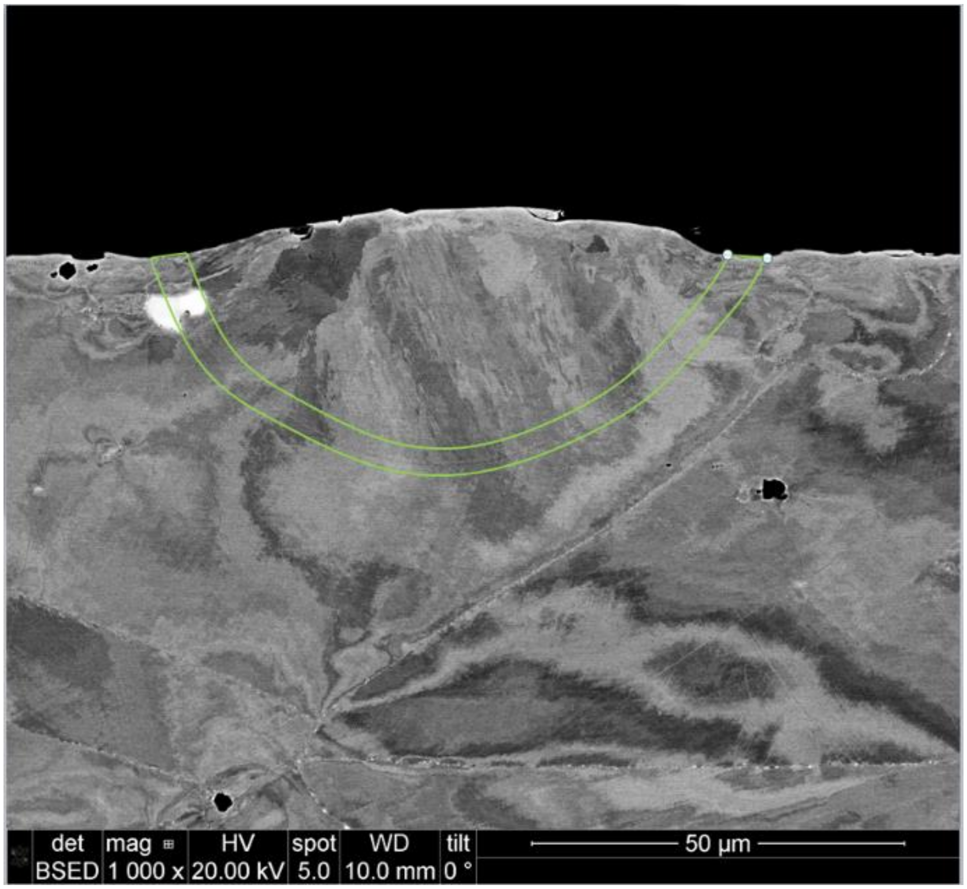

Figure 13: Melt-pool cross-section with melted boundary highlighted

The results from these single bead experiments influenced parameter selection for the next set of experiments which were single layer pads (rectangular raster geometries of only one deposition pass). These pads were deposited on 5” by 5” by ½” ground plates, similar to the single beads. The parameters chosen are based off of the single bead results with hatch spacing, or the distance between raster scans, scaled to be 76% of the single bead widths, resulting in a nominally 24% overlap of the beads (Figure 14). This amount of overlap was based on the nominal parameter pads created in the single bead experiment. The pads were chosen to be 12.7 mm by 19 mm to create a large bulk geometry free of edge effects. In order to fit on a single plate there were 24 pads created. This is still enough to thoroughly map the space and see trends. The parameters chosen can be seen in Table 2. These same pads were built up with no added powder, 20 μm (single layer) of powder, and 10 layers of powder. The build was terminated after 10 layers because the collaborators at NIST did not want to risk their equipment with larger deposition heights.

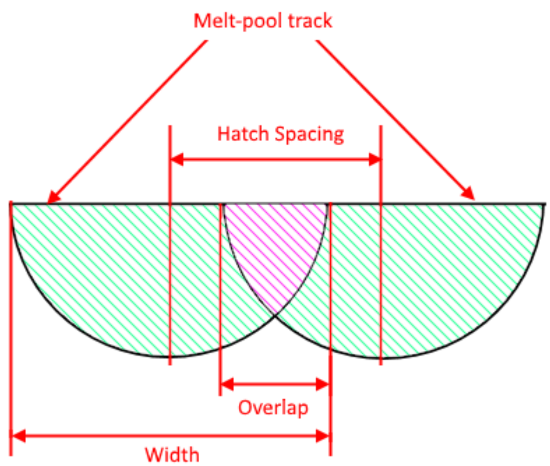

Figure 14: Illustration of hatch spacing

Table 2: IN625 Pad experiment parameters

Test	Power (W)	Velocity (mm/s)	Hatch Spacing Used (μm)
1	100	600	70
2	50	1000	40
3	50	400	60
4	50	600	50
5	150	600	100
6	100	400	100
7	150	1200	50
8	100	1000	60
9	100	800	60
10	50	1200	40
11	150	1000	60
12	195	600	110
13	50	800	50
14	100	1200	50
15	100	200	140
16	195	1200	70
17	150	400	130
18	150	800	80
19	50	200	80
20	195	800	100
21	195	400	140
22	150	200	160
23	195	1000	80
24	195	200	200

2.3 Results

2.3.1 Single Bead Widths

A process map of constant melt-pool widths was produced and can be seen in Figure 15. The process map shows a linear trend in width as expected. There is, however, a slight amount of curvature as power increases appears to be present. A constant effective absorptivity factor was calculated by dividing the absorbed power required for a given area by the source power from experiments to get the same area. An effective absorptivity of $\alpha = 0.51$ and this appears to fit reasonably well for width data across P-V space for IN625. This absorptivity is within the results found for literature of pure absorption of a similar wavelength laser (Nd:YAG) for a comparable alloy (IN718, a derivative of IN625) which, since this also includes other factors, is deemed a suitable fitting parameter [103].

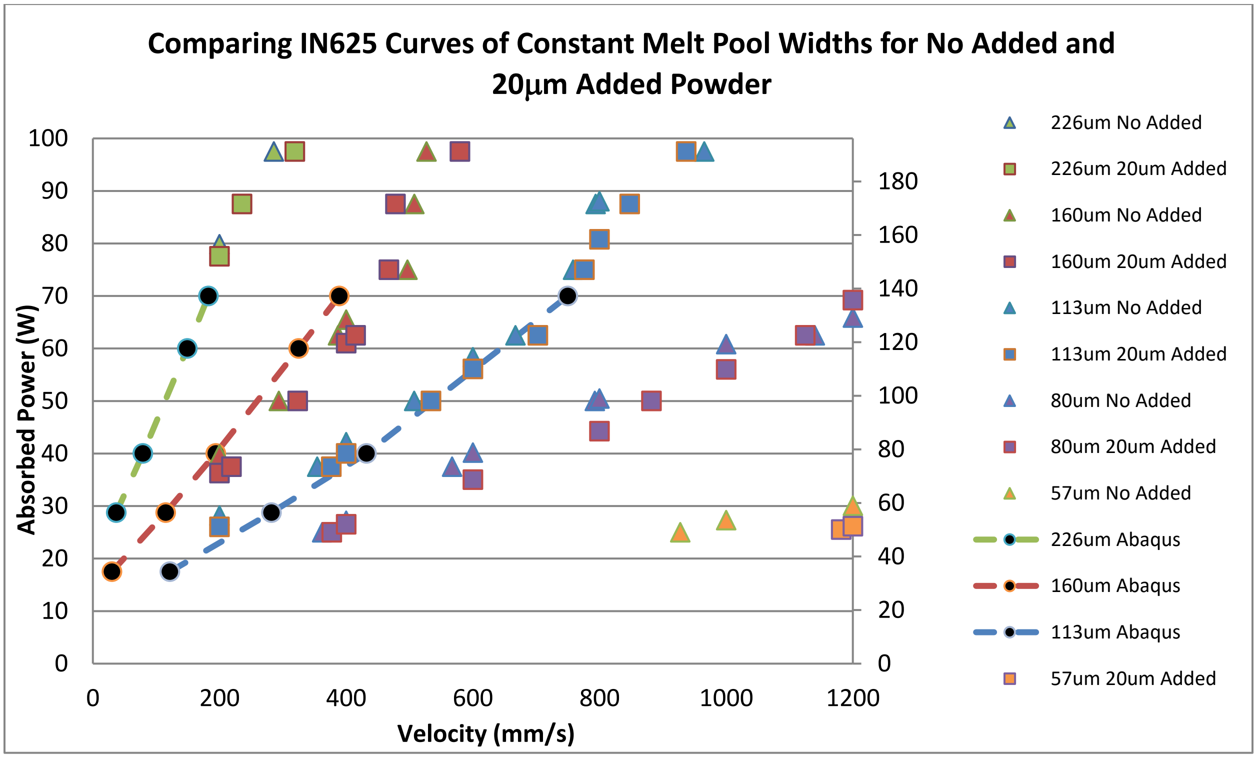

Figure 15: Curves of constant melt-pool width IN625 (constant absorptivity)

Comparing the experimental added and no added material results, it appears that powder had little effect on the melt-pool geometry. The no added material and 20 µm added material widths were nearly identical and appear to oscillate around each other, within the margin of error of the results.

An initial pad was created and then widths measured from above to calibrate further pad tests in terms of overlap percentage. The above view of the added material pad can be seen in Figure 16 and it can be seen that there is approximately 24% overlap in width when compared to single beads. All of the future pad experiments have hatch spacing scaled to this based on single bead widths.

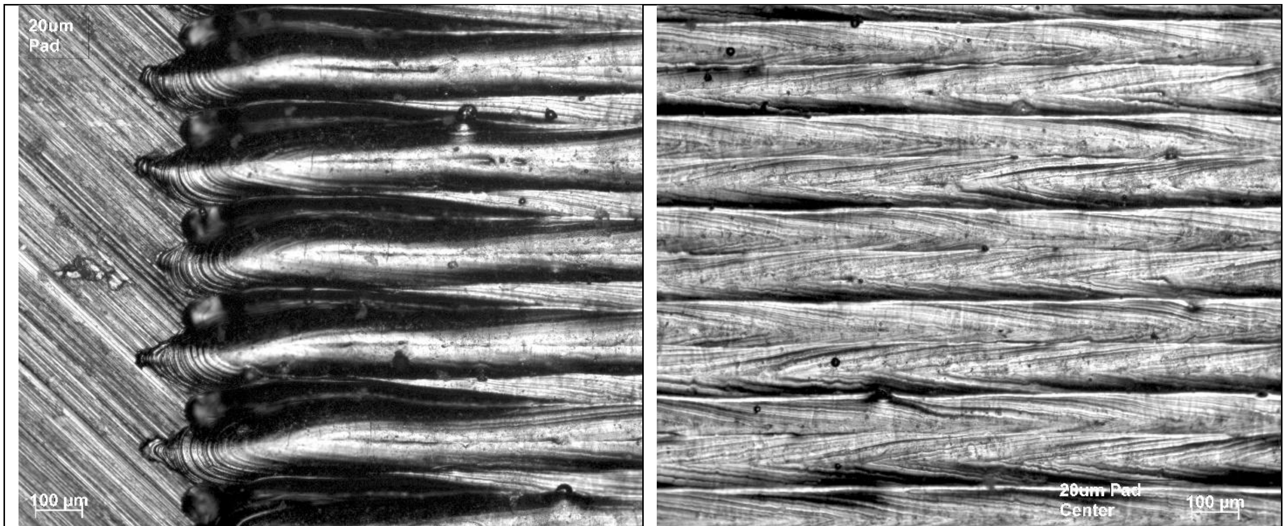

(a) (b)

Figure 16: Above view pad images showing bead overlap (a) at the edge and (b) in the middle of the pad

Another feature that was noted with the single bead above view images was the presence of splatter from ejecta from the melt-pool, and partially fused powder particles Figure 17. This is not of concern for single beads, but has adverse effects on surface finish as well as part quality. If these ejecta aren't the same chemical composition as the solidified material this could result in impurities in the final part. Ejecta is thought by some groups to be caused by recoil pressure of the laser, but recent work out of LLNL has shown that the air flow within the chamber created from vaporization of metal material may dominate in terms of ejecta formation by carrying metallic particles [104]. The partially melted particles sticking to the melt-pools are unavoidable and are inherent in the powder bed process, as the melt-pool cools particles touching the melt-pool can be partially trapped in the molten material.

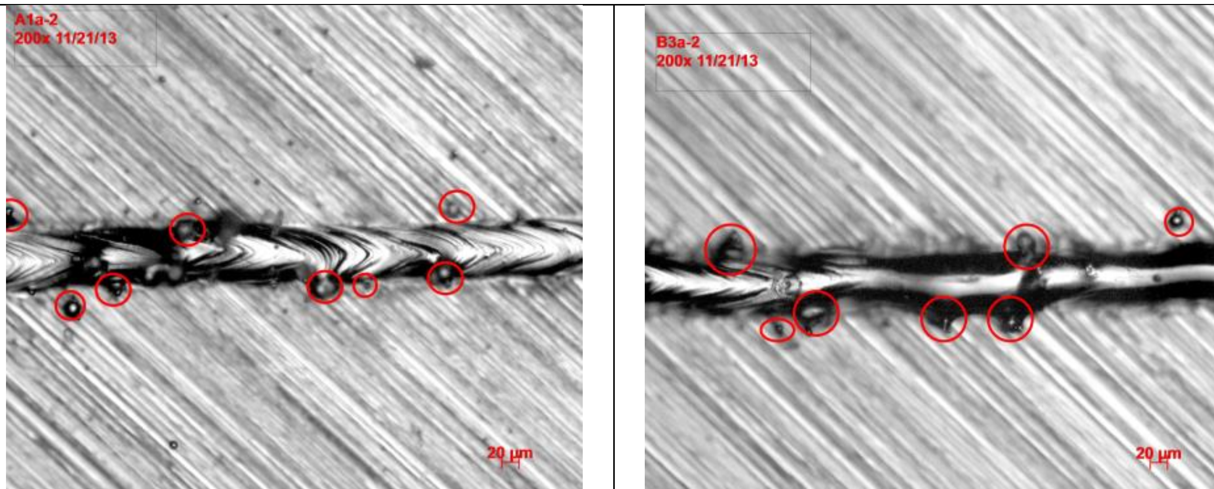

Figure 17: Melt-pool ejecta and fused particles seen from above

A final feature that was noticed from these above view images was the inconsistency at the beginning of the laser path. Occasionally the beam appears to overshoot where it should stop, but this could be calibration issues inherent with changing process parameters and not accounting for the scan path. An example image of what was seen compared to what is expected is shown in Figure 18. This illustrates the importance of knowing melt geometries if tolerances are important in the final part since path planning may have to be optimized for the new parameters chosen.

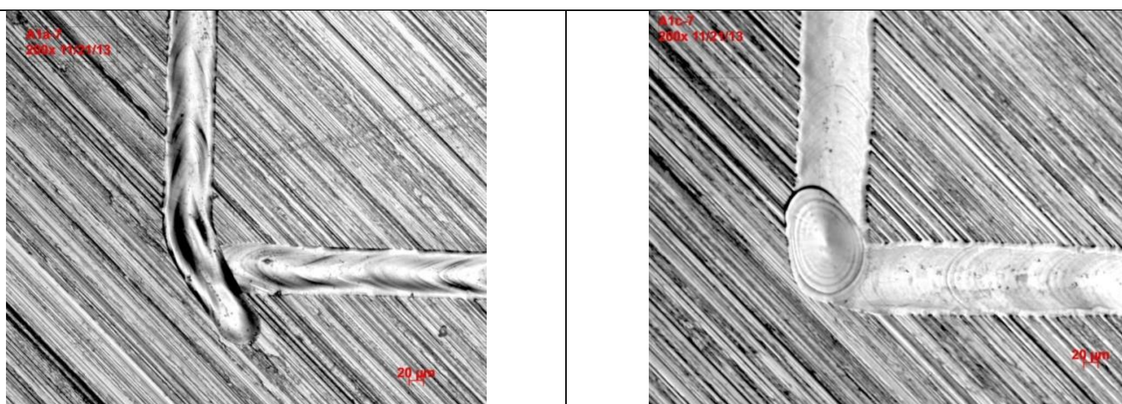

(a) (b)

Figure 18: Laser start and stop tracks (a) overshooting (b) ideal

2.3.2 Single Bead Areas

Process maps of cross-sectional area were developed for IN625 in the EOS M270 process space. Points in processing space were identified to help determine the usable range of the processing window (Figure 19). Although many points produced sufficient melting some points trip out of conduction mode welding and into a keyhole mode welding regime. Keyhole mode welding is a phenomenon where the applied power density is too great and vaporization of the base material occurs, resulting in higher penetration of the beam than pure conduction would allow [105]. A keyhole is defined as a melt-pool where the cross-sectional width is less than twice the depth. This can be helpful in penetrating to layers below, as well as potentially improving surface finish for vertical surfaces in the powder bed processes, because of the more vertical edge shape of the melt-pool. On the other hand, it can result in gas entrapment induced porosity due to rapid solidification around the vaporized hole [106] [107]. There are also regions of processing space where the melt-pool does not penetrate deep enough to bond to the layer beneath it. For IN625 this is when the melt-pool does not penetrate at least 20 µm (in practice this could be upwards of 40 µm in layer thickness in the steady state build condition due to powder consolidation, but for simplicity 20 µm is the ideal and nominal case). An outlier at 50W, 1000 mm/s was seen and this is likely balling and not actually keyholing, although mathematically it is labeled as such.

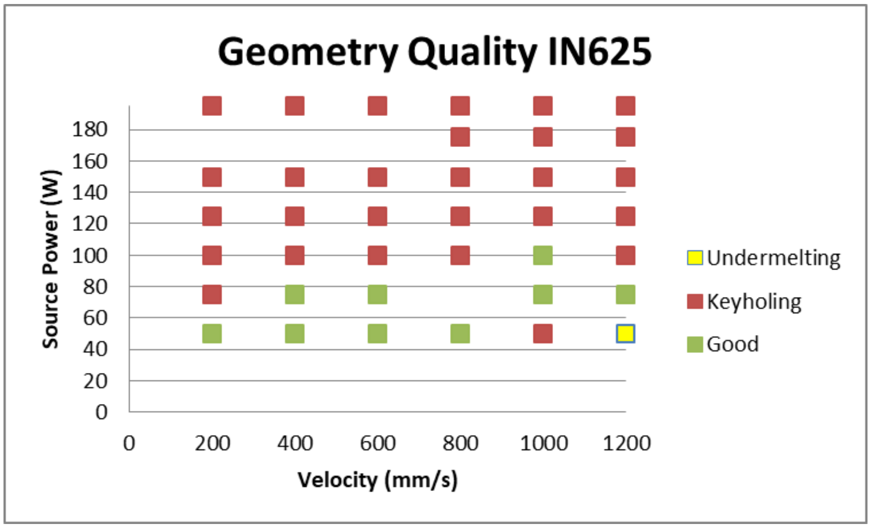

Figure 19: P-V map of geometry quality IN625

The keyholing region can be reduced by changing the spot size, thus expanding processing space, as suggested by Francis [108]. The spot size is fixed for most current EOS machines, however, so this is not investigated in this thesis. Note the outlier at 50 W, 1000 mm/s, this point seemed to be missing one of the melt tracks and was also barely keyholing based on the definitions presented above, this could just be a fluctuation in laser power or an error in programming the parameter set. Operating on the edge of minimal melting is not advised either due to slight fluctuations in the laser power potentially resulting in under-penetration and thus inter-layer defects such as lack-of-fusion. The processing window is seen to be very narrow with current focus settings on the M270.

From the cross-sectional results a P-V map was created for cross-sectional areas Figure 20. The plot clearly shows a linear trend for all given cross-sectional areas. This is congruent with the results that were seen for Ti-6Al-4V for the Sciaky Electron Beam Wire Feed process [98]. Looking at the plot in Figure 20 it is evident that the addition of 20 µm of powder has very little effect on the resulting melt-pool cross-sectional area. The curves corresponding to these two cases appear to oscillate around each other and are within measurement error of each other.

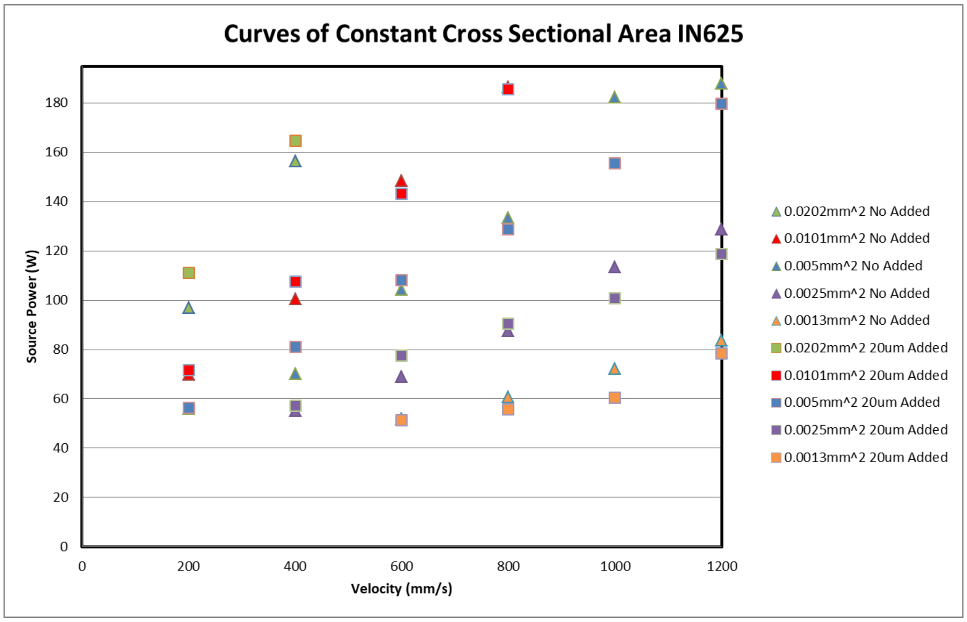

Figure 20: IN625 experimental curves of constant cross-sectional area

The simulations for the addition of 20 µm of powder are compared to the simulations without any addition of material (Figure 21) in terms of melt-pool depth. The curves can clearly be seen to be negligibly different with the addition of 20 µm powder requiring slightly higher velocities compared to no added material. Overall the points overlap almost perfectly and thus powder appears to be negligible from the simulations performed.

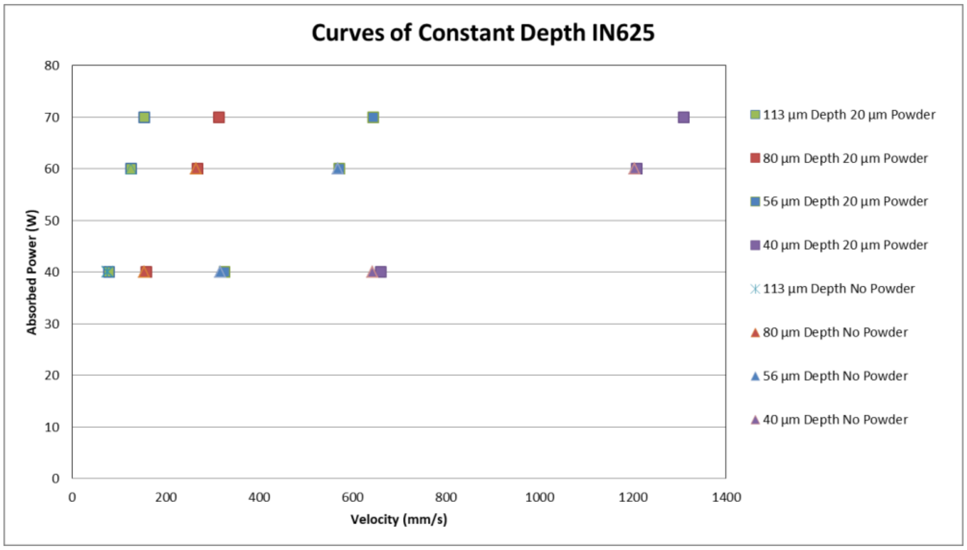

Figure 21: Curves of constant depth from simulations for 20 µm of powder compared to no added powder IN625

To correlate experiments with simulations, a constant effective absorptivity of 0.57 is applied across P-V space by averaging the absorptivity required for each point. The fit can be seen in Figure 22 and provides a reasonable approximation between simulations and experimental curves across P-V space. This is not very realistic since as mentioned previously keyholing is not modeled and thus any points that are keyholing are not accurately modeled with a purely conduction mode model.

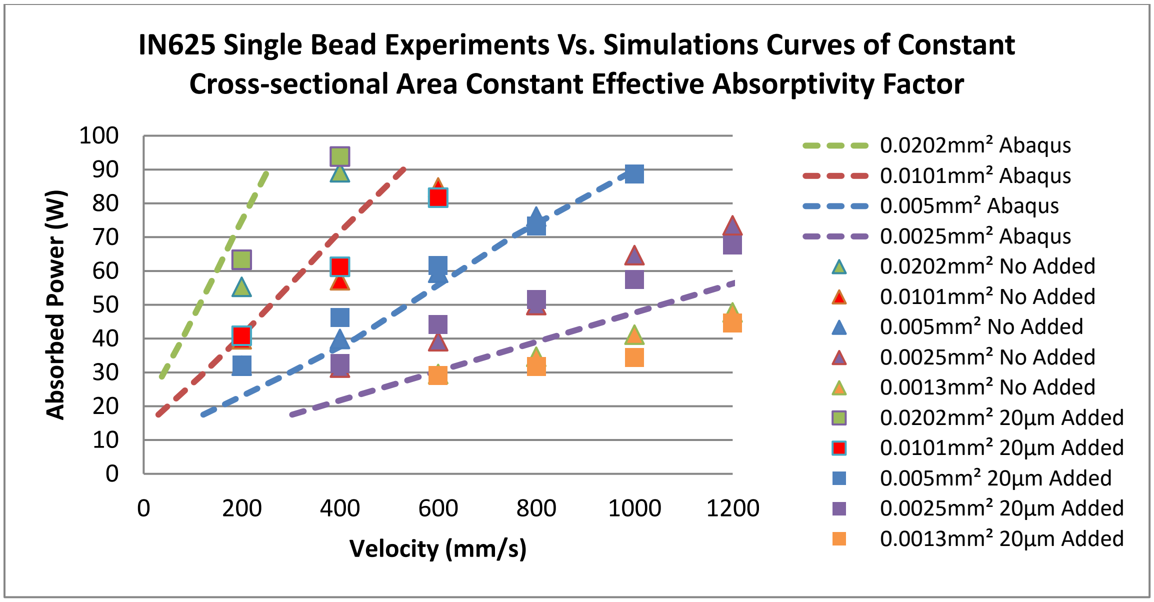

Figure 22: IN625 curves of constant cross-sectional area fitted with constant effective absorptivity

A better correlation can be achieved by limiting the curves to only those that are not keyholing. By doing this and varying effective absorptivity with cross-sectional area (from α = 0.50 to α = 0.42) the correlation becomes much stronger between the simulations and experiments (Figure 23). Effective absorptivity increases with increase in cross-sectional area; this is thought to be because of spot size and laser interaction with the molten material which is at a higher temperature than the material that is not being melted. Higher surface temperatures result in a higher absorptivity for the laser (0.33 at low temperatures up to 0.55 at high temperatures) [103]. Recent literature suggests that changes in melt-pool morphology change absorptivity [109]. This literature doesn't correlate melt-pool size with absorptivity directly but this can be extrapolated when looking at these results and comparing them to the results in presented here.

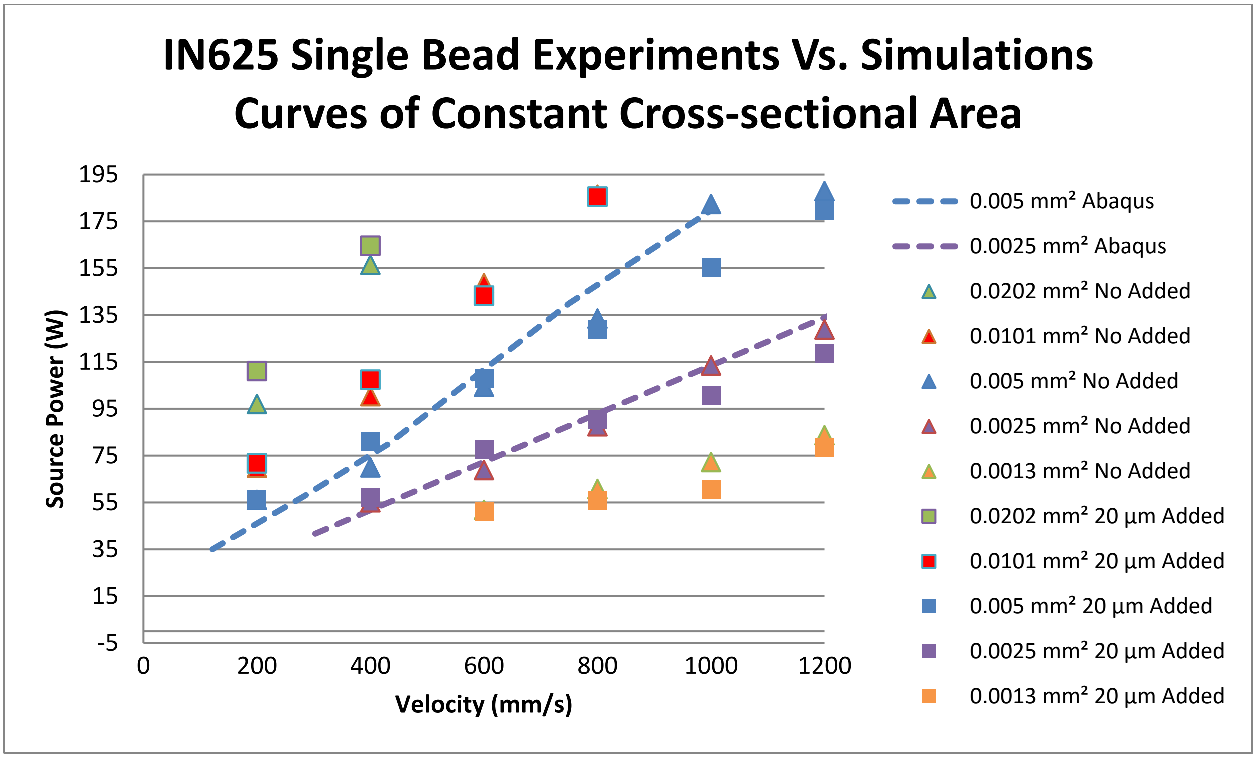

Figure 23: IN625 curves of constant cross-sectional area fitted with varied effective absorptivity

In an attempt to confirm this hypothesis of surface temperature dependence, simulations of IN625 and prior work in AlSi10Mg by Narra [110] were examined to determine the temperature of the material directly under the laser spot and average volumetric temperature of the melt-pool for two different melt-pool areas. The measurement, comparing the results to literature are plotted in Figure 24 [103] [111]. Absorptivity appears to increase with increasing spot and volumetric temperature, although the spot temperature difference is more prominent. This agrees with the hypothesis that increased spot temperature for the laser is the cause of the increased absorptivity of the melt-pool and with literature that molten metal has a higher absorptivity than bulk material [112]. The spot temperatures are extremely high due to the application of heat flux at these nodes. Looking at the volumetric average temperature of the melt-pool is a way to approximate molten material convection within the melt-pool as well mixed. Using the volumetric average temperature brings the values closer to what is reported in literature, compared with the average spot temperatures. This indicates that there are still other effects that are not being accounted for in the thermal model, such as higher radiative/convective or kinetic losses that would reduce the temperature further. The lower absorption than predicted could also be a result of an oxide layer that is forming within the process or the vaporized material plume interacting with the laser that is inhibiting the laser absorption compared to what is expected at these temperatures.

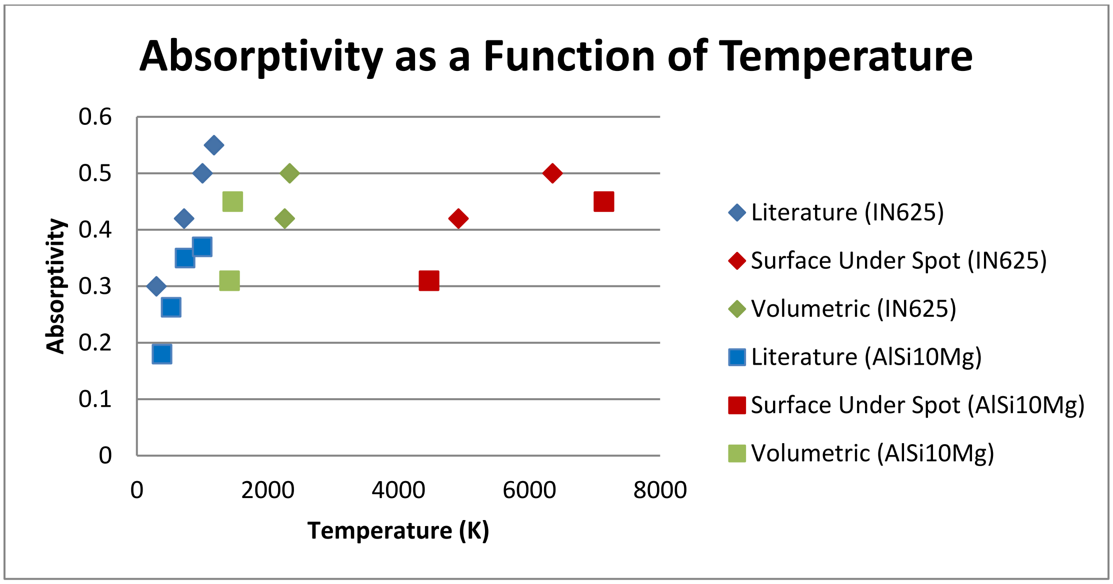

Figure 24: Absorptivity vs Temperature for IN625 and AlSi10Mg (Simulations and Literature)

Nominal parameter results can be seen outlined in red in Figure 25 and it is apparent that the nominal case is in a transition keyhole regime [113]. These are likely chosen as the nominal parameters because of an increase in penetration to the layer below, but consequently could also result in porosity. To reduce the chances of porosity it is often recommended that the parameters be shifted to a higher velocity and out of the keyhole regime.

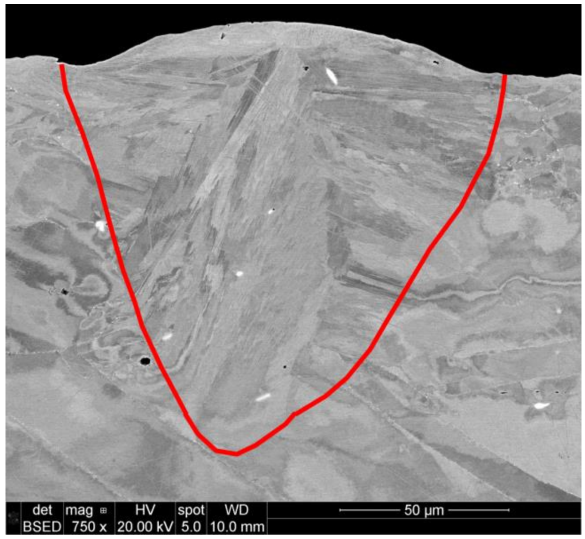

Figure 25: Nominal IN625 melt-pool

This process map showed with great confidence that for small layer thicknesses the effect of powder on melted geometry was negligible. This is promising because it potentially reduces the simulation and experimentation requirements for alloy development.

2.3.3 Single Layer Pads

A comparison of a no added material single layer pad and a 20 µm single layer pad for the same process parameters can be seen in Figure 26. These melt-pools are of similar size and shape to each other and both appear to be porosity free and not keyholing. The melt-pool geometries are hard to get full widths and measurements from due to the overlapping nature of the pads. However, the results, based on the overlap distance, can be calculated and the widths and depths are similar to the single bead results.

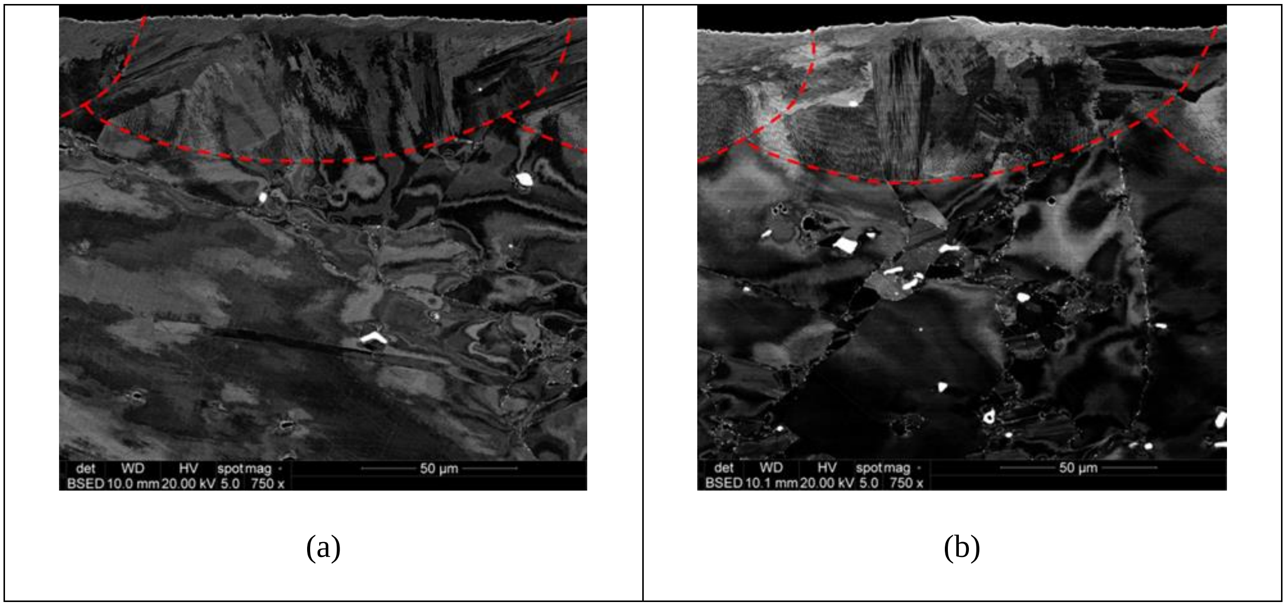

Figure 26: (a) No added material pad and (b) 20 μm pad for the same parameter combination

When comparing the single 20 μm layer results to single bead results the melt-pool geometries seem to be on similar scales and of similar morphology. Even when keyholing in the single bead experiments the melt-pool is still keyholing when scaled to the pad geometry and is of similar dimensions (Figure 27).

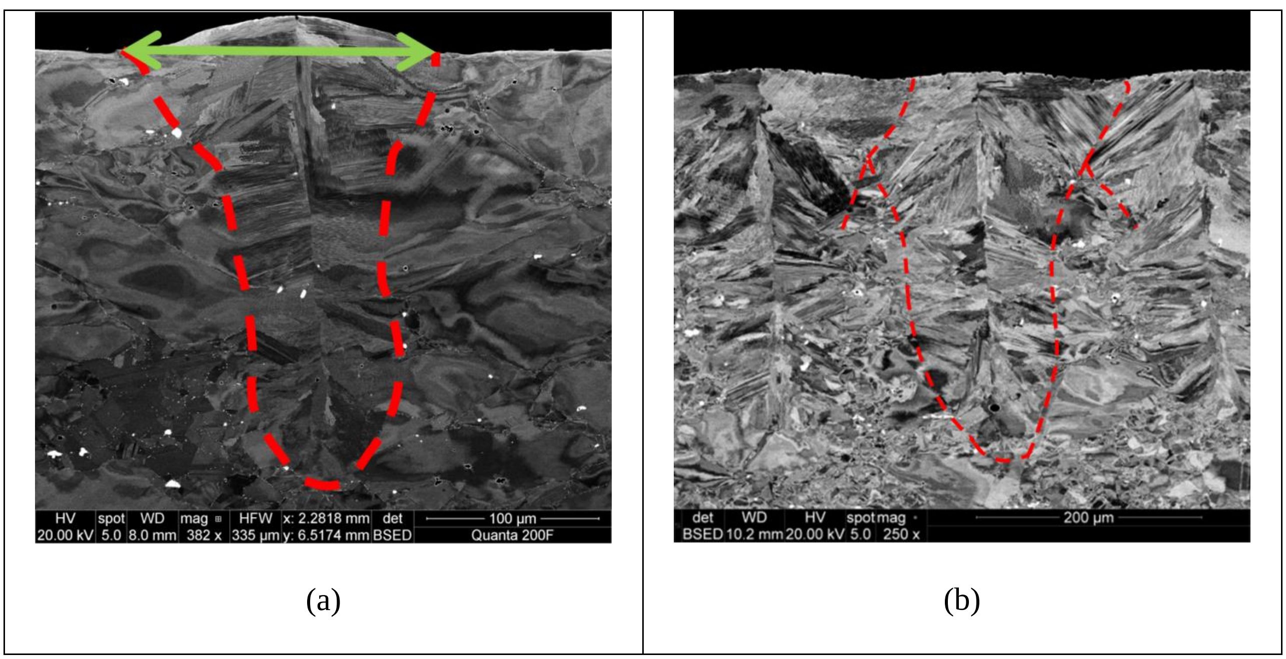

Figure 27: (a) 20 μm Single bead (b) 20 μm pad for the same 195W, 200 mm/s parameters

2.3.4 Multi-Layer Pads

Multi-layer pads were examined for geometry and flaws. The geometries that were able to be seen were similar to those expected based on single bead and single pad experimentation. From the limited number of deposited layers (10) from the multi-layer experiments for this alloy system it is hard to see any induced porosity because many of the keyholes penetrate through the entirety of the 10 layers and the undermelting cases don't become severe enough in 10 layers to cause a large issue.

From the micrographs it is apparent that grains are growing through multiple layers, this is a promising result since it shows that there will not be segregation between layers in terms of strength (Figure 28). This is also an intriguing result because by having grains growing through multiple layers the grains increase in size and thus increases the ductility of the part. Without an increase in grain size the grains would be very small and the resulting microstructure would be strong yet brittle.

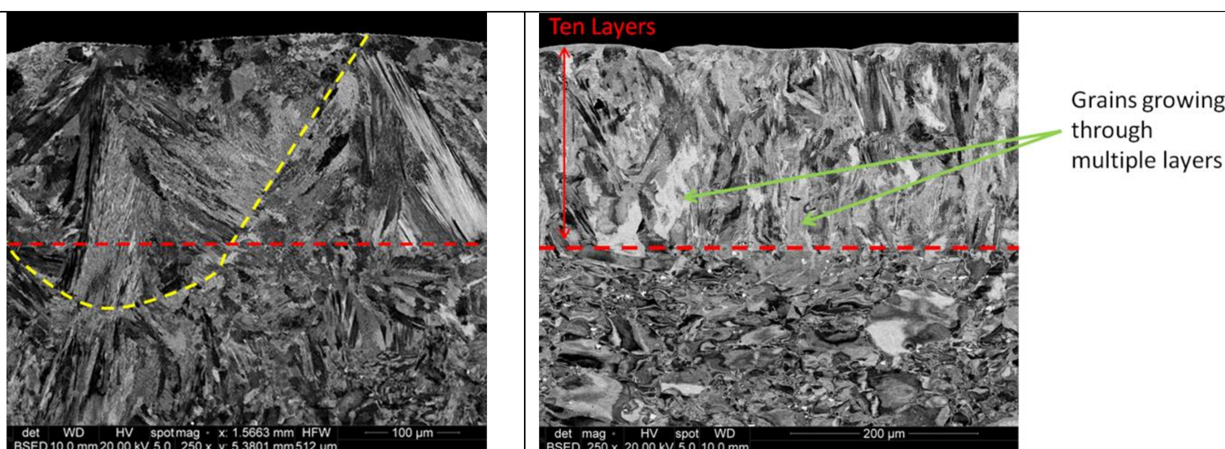

(a) (b)

Figure 28: Multilayer pad images (a) beads penetrating all 10 layers, (b) grains growing through layers

2.3.5 Conclusions

Inconel 625 has been process mapped for the L-PBF process with respect to melt-pool geometry. The curves of constant width and area are similar to what was expected from previous work in other processes and alloys. Varying the effective absorptivity with cross-sectional area was found to provide the most effective fit between simulation and experimental results. The effect of a single 20 μm layer of powder was determined to be negligible throughout the majority of processing space with the greatest deviation happening at low power high velocity range where melt-pools are inherently smaller (and measurement deviations are largest). These results make sense since the powder should allow for more reflections of the beam and thus a higher absorbed percentage of the incident radiation.

Basic microstructural observations were made and it was found that grains are growing through layers of material and not confined to a single layer or melt track. Single bead and single layer pad results translate well to multi-layer pad bulk geometries. This test methodology has been proven to be well suited for developing process parameters for any new alloy system in the L-PBF process.

Chapter 3 Process Mapping 17-4 Stainless Steel

3.1 Overview

This chapter explores process mapping of the geometry of 17-4 Stainless Steel produced via L-PBF. The ability to move directly from single bead geometries to multi-layer pad geometries is investigated as a way to streamline process parameter development. Simulations are compared to experimental results to determine the ability to simulate the additive manufacture of 17-4 reliably. The addition of a single layer of powder is examined in relation to beam on plate experiments and conclusions about the effects of powder are drawn for 17-4. Finally, comparisons are made between the process maps of 17-4 and IN625 and conclusions about rapid process development are drawn.

3.2 Methods

Single bead experiments were performed on the EOS M270 at the National Institute of Standards and Technology (NIST) in September of 2015. As with IN625, 42 different single bead combinations were chosen and then lased on a 17-4 Stainless Steel plate with a ground finish in order to simulate a bulk material deposit. The parameters chosen can be seen in Figure 29 and span a large region of processing space. Low powers at high velocity were excluded because it is assumed that insufficient melting will occur and the parameters won't be useful. High power low velocity points were also excluded because this is a region known to exhibit severe keyholing, which is also undesirable to the end user.

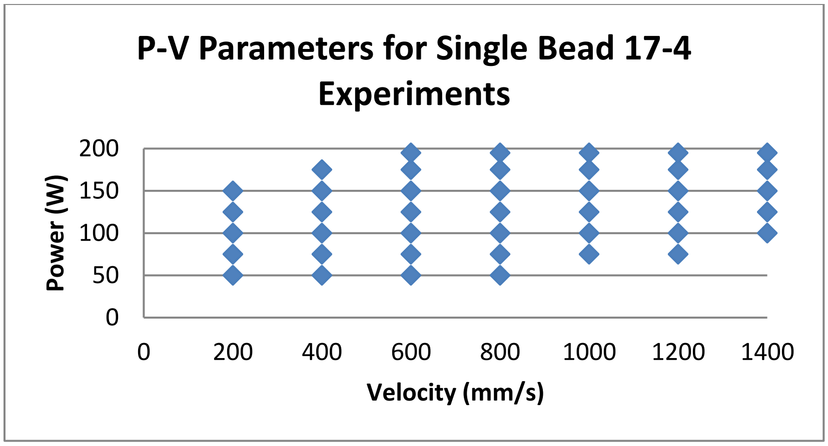

Figure 29: Single bead experiment parameters for 17-4

EOS GP-1 (UNS 17-4) gas atomized powder was used, which is roughly spherical with a mean particle diameter of 36 µm and a bottom end of 24.4 µm [69]. This clustered size distribution and lower 10% limit is important to note for 17-4 as our experiments were performed with an initial layer of nominally 20 µm, which means that only a very small fraction (<10%) of the particles were spread on the plate. All other particles were either swept off the build plate or deposited in defects in the baseplate. Since this is a known phenomenon it's common to provide excess powder on this initial spread to ensure an even spread of 20 µm of powder across the plate.

As research progressed analysis methods evolved as well. To measure above view widths an image analysis code was created that measured the width of the melt-pool throughout the entire image. The code works by finding the top edge of the melt-pool, which is indicated by a red line that is manually traced onto the image, and then counting the number of pixels until the bottom edge of the melt-pool, also indicated by a red line, is found. This method does not remove all human error because it still requires a human to trace the melt-pool to begin with. However, this gives a better result since the program can generate thousands of data points along the melt track to minimize the effect of human error, and give better statistical properties. After imaging from above the single bead experiments were sectioned using a wire EDM and then mounted, ground, and polished using the procedure by Buehler (Appendix A). The samples were then electrolytically etched using the procedure in Appendix A. A representative micrograph of the sectioned and polished 17-4 single bead sample with key dimensions labeled is shown in Figure 30, where all notation is consistent with work presented previously.

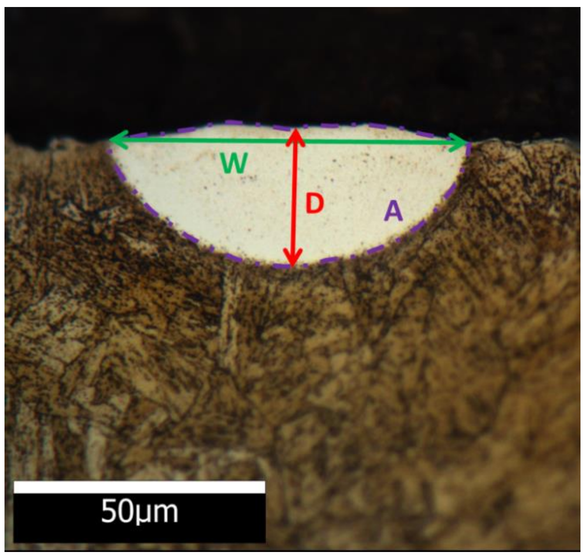

Figure 30: 17-4 Cross-section of single bead with labeled dimensions

It was hypothesized that the single layer pad experiments were not strictly needed after single beads, if the hatch spacing percentage was known. To test this hypothesis the author decided to progress directly to multi-layer pad experiments. These experiments were performed at CMU on an EOS M290, which is a newer variant of the equipment that had been used for the single bead experiments at NIST. In order to maintain congruency with previous single bead experiments on the M270 only powers up to 195W were used. For the multi-layer experiments only 24 parameter combinations are used to reduce sample size while still providing sufficient data points to accurately map the process space. The parameters chosen for the pad geometry can be seen in Table 3. Hatch spacing was scaled to be 30% based on single bead widths. This amount of scaling allows for sufficient overlap to avoid most lateral porosity by accounting for fluctuations in the melt-pool width [114].

Table 3: 17-4 Pad experiment parameters

Pad Number	Power (W)	Velocity (mm/s)	Assigned Hatch Spacing (μm)
1	50	200	60
2	50	400	50
3	50	600	40
4	50	800	40
7	50	1000	40
8	100	200	120
9	100	400	90
10	100	600	60
11	100	800	50
12	100	1000	50
13	100	1200	40
6	100	1400	40
14	150	200	150
15	150	400	110
16	150	600	100
17	150	800	70
18	150	1000	60
19	150	1200	60
20	150	1400	60
5	195	600	110
21	195	800	80
22	195	1000	70
23	195	1200	60
24	195	1400	60

The multilayer pads were created on a ground 6” by 6” by ¼” 17-4 PH plate purchased from McMaster-Carr. This plate was affixed to a modified build plate and deposited upon with 20 μm layers for a total height of approximately 0.375”. The thicker bulk geometry was done because the author was confident that no machine damage would come from any recoater impact and the greater thickness allows for more accurate conclusions about bulk depositions when compared to 10 layers which a keyholing melt-pool could potentially penetrate through all of them. The resulting samples can be seen in Figure 31. The samples were angled to minimize interaction with the recoater blade. Contours were left enabled to default parameters since edge effects were not under investigation and the contours could affect the buildability, or ability to build, the pads.

Figure 31: 17-4 Multi-layer pad experiments

The resulting multilayer samples were sectioned with a slow speed saw and then ground, polished, and electroetched using an oxylic etchant. These samples were then examined using the Alicona InfiniteFocus microscope at CMU. The multilayer samples were analyzed for expected and unexpected flaws based on the single bead results.

Computational methods were also utilized in this chapter. The models discussed previously were updated to include the material properties of 17-4 stainless steel and then run to generate process maps of constant cross-sectional area [13] [5].

3.3 Results

3.3.1 Single Bead Widths

An experimental process map of the single bead widths was created for 17-4 by interpolating between experimental results Figure 32. The curves are again extremely linear across P-V space for the new alloy system. Comparing the powder and no powder results, as was seen in Chapter 2, there again appears to be little difference. The 20 µm added material points and the no added material points are extremely close to each other and are both within each other's margin of error represented by the error bars. The error bars correspond to the curve of constant width determined by the maximum power data point and the minimum power data point at a given velocity, while the points themselves represent the mean width. This suggests that the trend is alloy independent and not a phenomenon only associated with IN625, at least with respect to single bead widths.

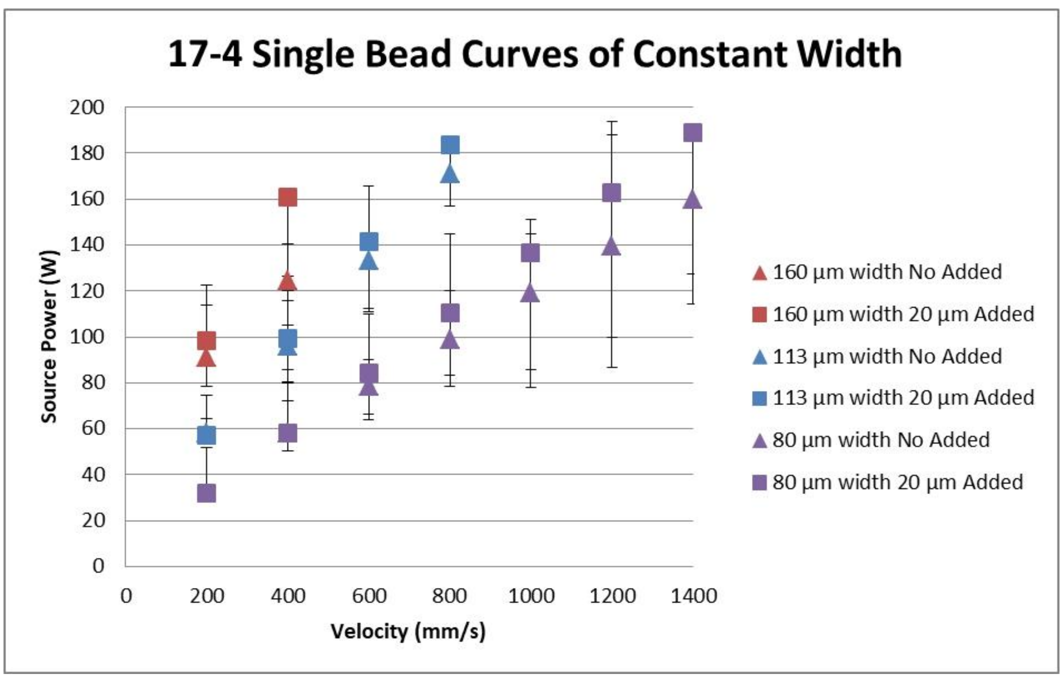

Figure 32: 17-4 Curves of constant width

Balling, or "bead-up" is observed at generally high velocity and high power points and is a phenomena thought to occur during solidification due to high surface tension in the liquid state [115]. This phenomenon is characterized by a discontinuous melt track where the beads "ball" in an attempt to lower surface energy an example can be seen in Figure 33. Points that were balling are high velocity and high power parameters, and are highlighted in Figure 34. The IN625 beads did not appear to have as aggressive balling (only visible in the 195W 1200 mm/s case) but this is likely due to slight surface tension differences of the material compared to 17-4, as well as the slightly larger processing window investigated with 17-4. The surface tension values are highly dependent on chemical composition of the alloy powder as well as oxygen concentration, so depending on powder quality and processing conditions during the build this value could change significantly [116].

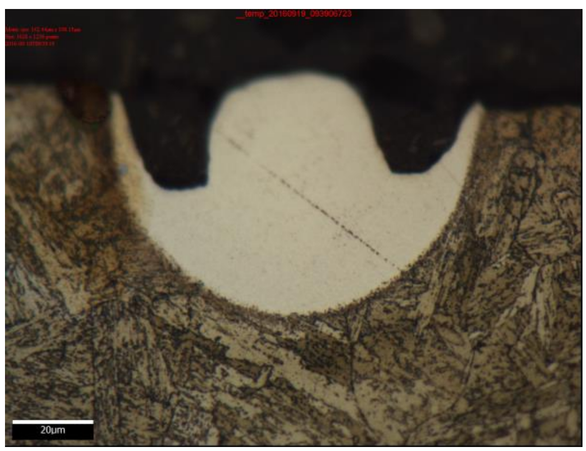

Figure 33: Cross-sectional example of bead-up

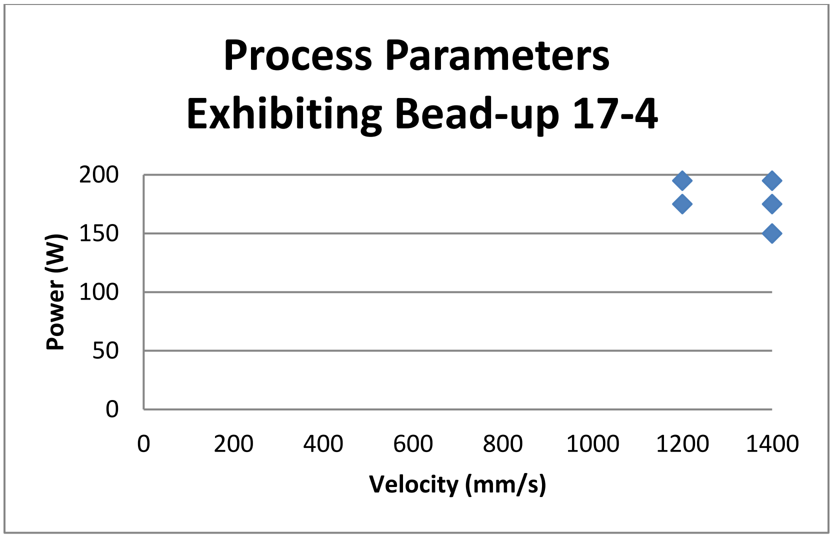

Figure 34: Points exhibiting bead-up in 17-4 single bead experiments

3.3.2 Single Bead Areas

Simulations were run to determine the effect of 20 µm of powder on the new alloy system and a process map of constant cross-sectional area was produced for both cases (Figure 35). The powder simulations appear to indicate a slightly larger cross-sectional area for a given parameter combination. This is in agreement to what was seen from both simulations and experiments in the IN625 alloy system investigated in Chapter 2.

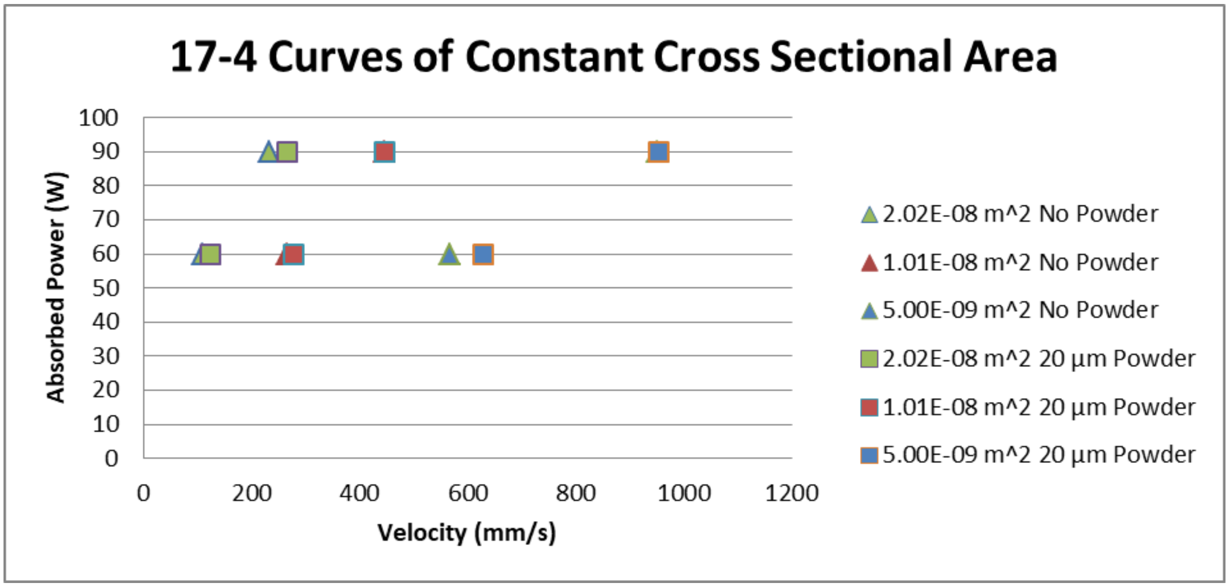

Figure 35: Curves of constant area from simulations for 20 µm of powder compared to no added powder 17-4

The cross-sectional samples were measured to find key melt-pool dimensions and features. A summary of the geometric features observed in the 17-4 cross-sections was created (Figure 36) for both the 20 µm added material and no added material single bead experiments. The undermelting region is larger than was seen previously with IN625 (Chapter 2). The undermelting region decreases slightly with the addition of powder, but upon examination of these points in the data the increase in small enough to be within measurement error. Most importantly it becomes readily apparent that the "good" melting range is greater for the 17-4 alloy when compared to the previous work with IN625. The proper processing window is still relatively narrow within the overall operating space available to the equipment. Note that with the 20 µm layer of powder single beads that the points on the edge of keyholing in the no added material experiments are sometimes pushed into extremely mild keyholing with the addition of powder, due to the insulating properties of the powder.

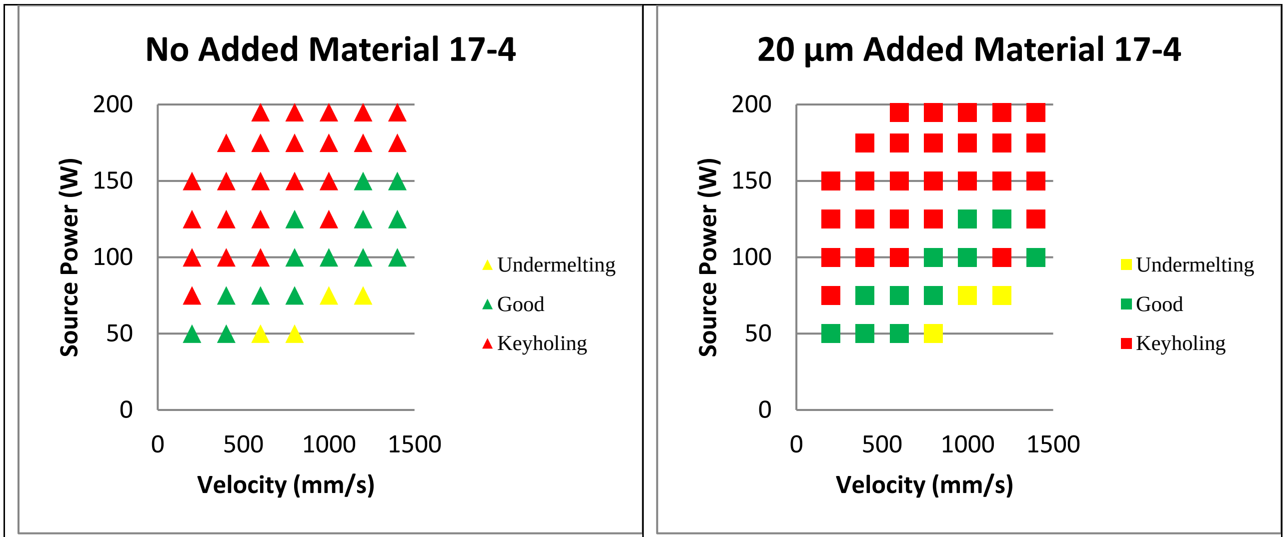

(a) (b)

Figure 36: Process map of geometric quality for 17-4 single beads with (a) No added material and (b) 20 µm added material

The nominal parameters that EOS provides (195 W, 1000 mm/s) are again within the keyholing region of process space. The nominal parameter melt-pool for both no added and 20 µm added can be seen in Figure 37 and appears to be of a transition keyhole geometry. Their parameters chosen do not appear to be resulting in large scale porosity evident as a result of the keyhole weld, within the single bead. The resultant melt-pools appear to exhibit milder keyholing than the nominal parameters for IN625.

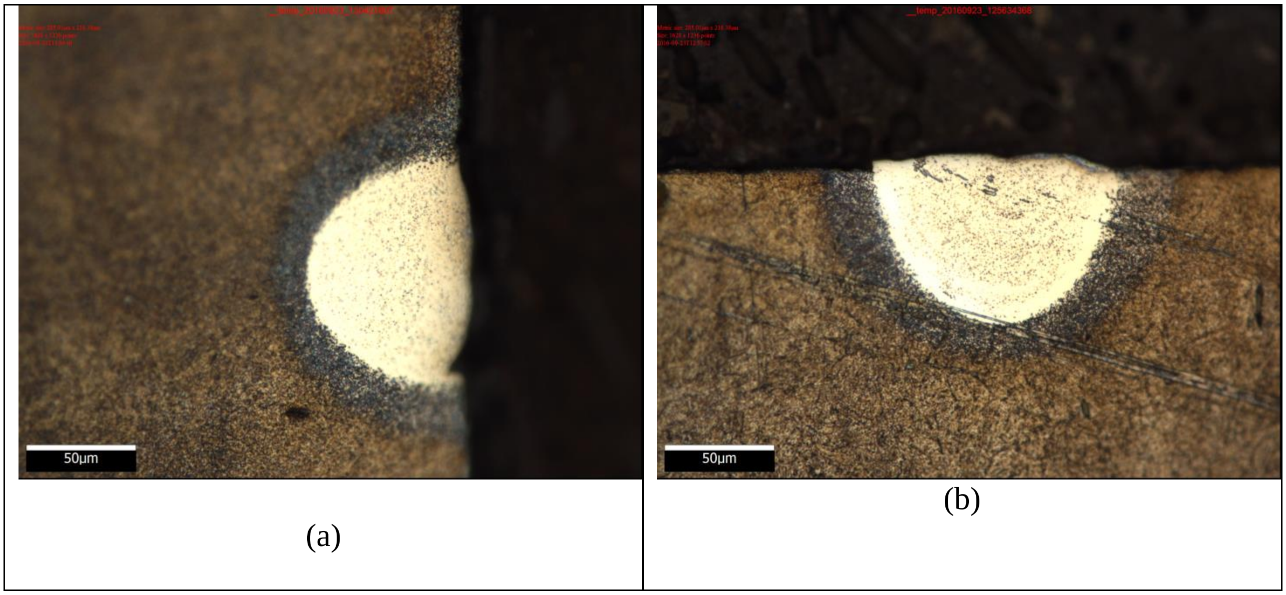

Figure 37: 17-4 Nominal single bead cross-sections (a) No added material and (b) 20 µm added material

Figure 38 shows the experimental process map for cross-sectional area for the 17-4 alloy along with fitted no added material simulation results. Simulation results are scaled by an effective absorptivity (α = 0.47) which if held constant results in a poor fit overall.

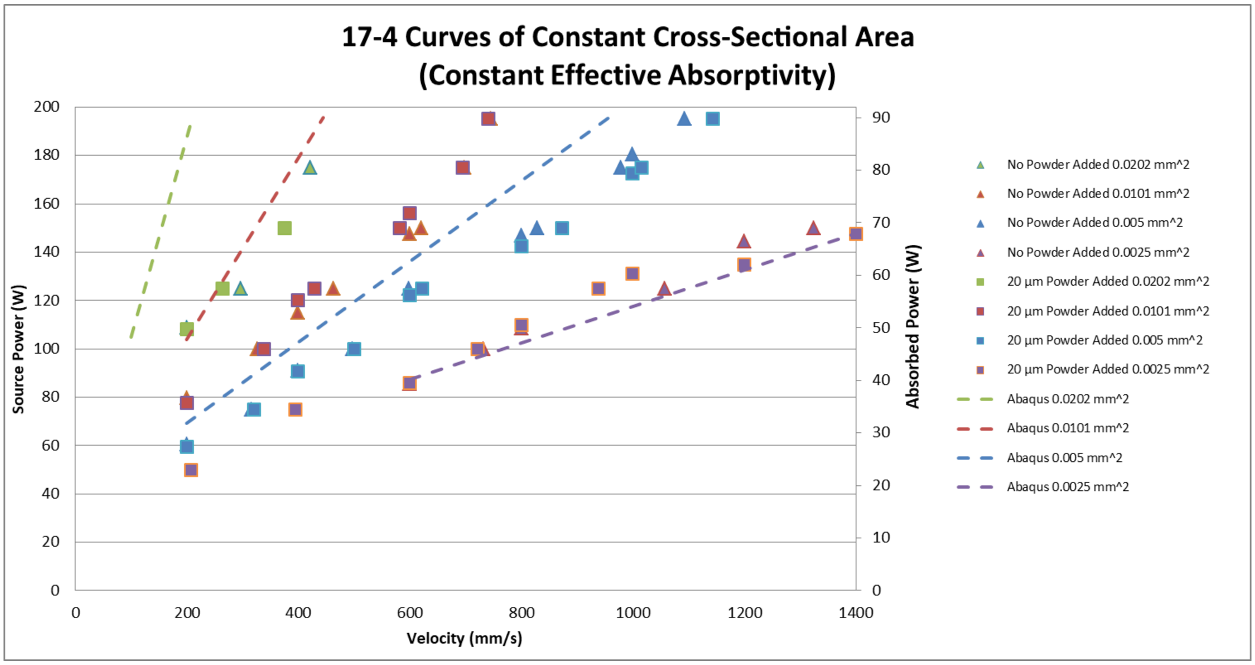

Figure 38: 17-4 Curves of constant cross-sectional area with a constant effective absorptivity (α = 0.47)

Scaling the no added material simulation results with an effective absorptivity that varies with cross-sectional area again provides a much better fit across all of processing space (Figure 39). The effective absorptivities range from α = 0.52 (A = 0.0050 mm^2) to α = 0.44 (A = 0.0025 mm^2) for 17-4, which is slightly higher when compared to the values of IN625 for the same cross-sectional areas. This is likely because the optical properties are slightly more favorable for 17-4, since thermally the materials are very similar [5] [10]. As with IN625 the simulation curves are only plotted for the cases that are not in the keyholing regime, since the models do not account for the vaporization phenomena.

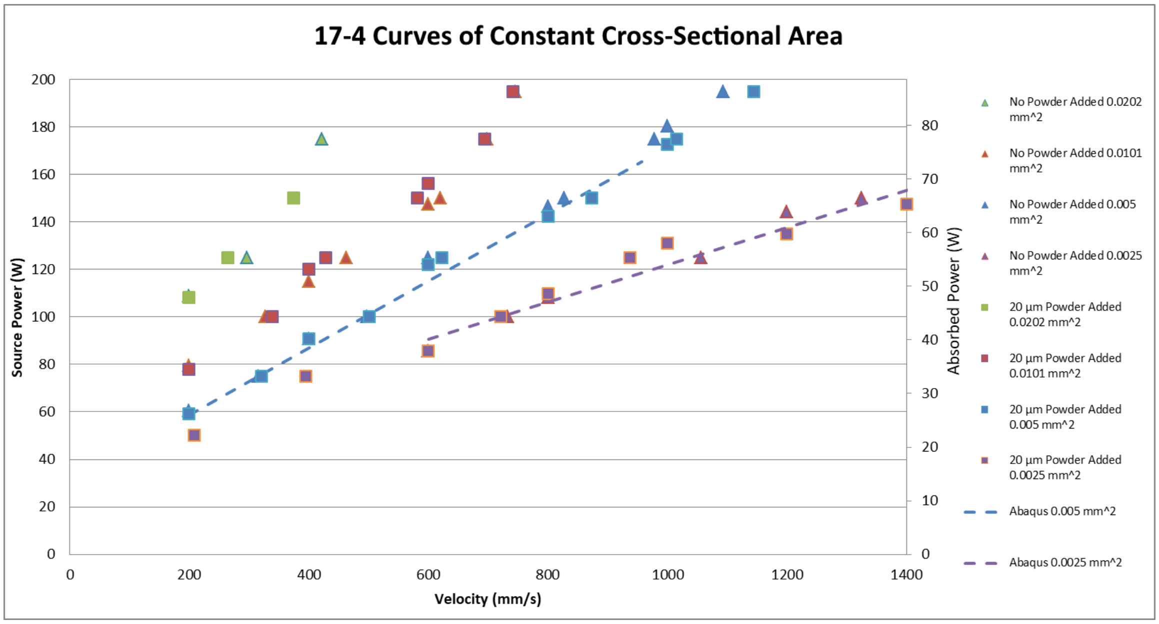

Figure 39: 17-4 Curves of constant cross-sectional area with varied effective absorptivity α = 0.52 (A = 0.0050 mm²) and α = 0.44 (A = 0.0025 mm²)

Correlating the curves of constant cross-sectional area between 17-4 and IN625 can allow inference as to the effects of the various materials. Both alloys have similar thermal properties, powder size distribution, and densities, however are extremely different alloys. Comparing the experimental results between the two (Figure 40) illustrates that the two alloys have similar process maps in P-V space. This is verification of the assumption that the thermal properties dominate the deposition process in terms of melted area. Residual stresses will behave differently (because of microstructural differences), as will keyholing behavior because of vaporization of material.

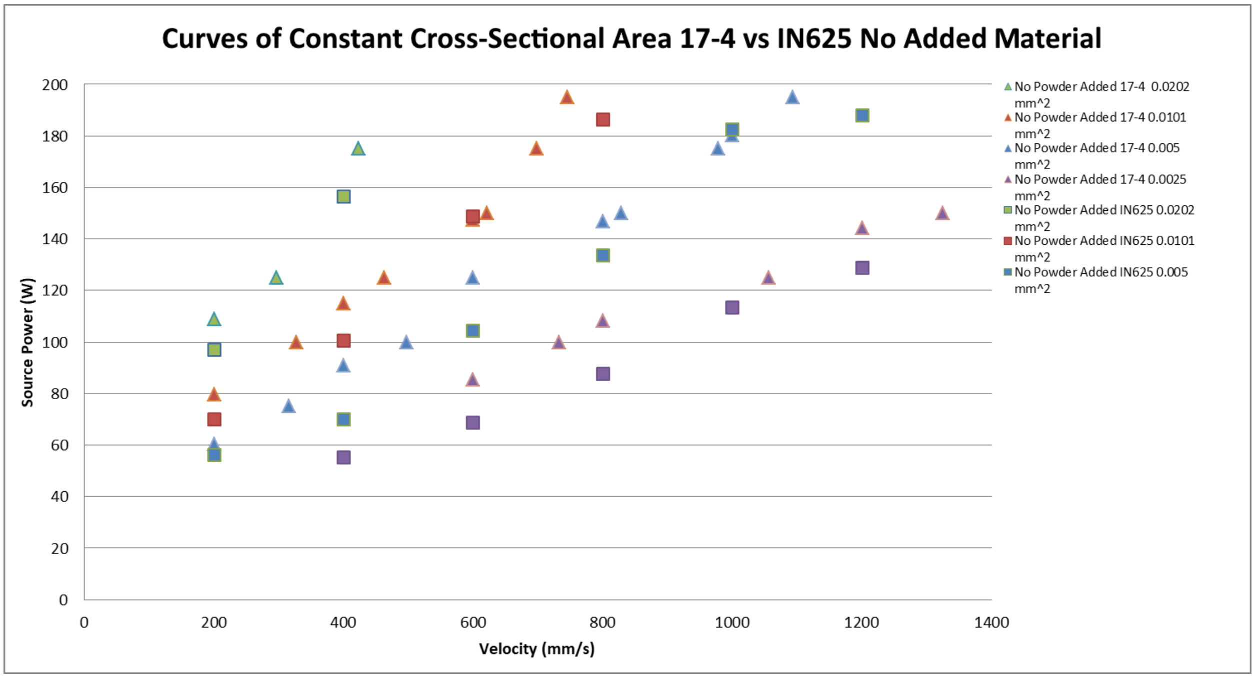

Figure 40: Curves of constant cross-sectional area comparing 17-4 and IN625 for no added material

3.3.3 Multi-Layer Pads

By inspection some of the pads readily appeared to have surface finish issues (Figure 41). These pads all had parameters that were severely keyholing and were low velocity combinations that would result in a longer time in the molten state. The resulting surface finish is likely due to surface tension causing balling of the molten material. An interesting feature was discovered when a magnet by chance was passed over the plate. The samples with the terrible surface were highly magnetic compared to the other samples. This indicates a high percentage of the delta ferrite phase of material in the microstructure of the samples produced in this region [117]. While the ability to design magnetism into certain regions of a part could be beneficial it should also be noted that any significant percentage of this delta-ferrite phase will decrease the toughness of the material which could result in cracking during any post processing machining operations, and more importantly for this alloy, decrease corrosion resistance [117]. Precipitates within 17-4 at the high cooling rates associated with AM are incredibly small and thus require the use of Transmission Electron Microscopy (TEM) to be able to be seen.

Figure 41: 17-4 Pads with various surface finishes

The pad geometries were analyzed for cross-sectional features. Since full melt-pool measurements of multi-layer pads are extremely difficult due to the 67° rotation between layers results are mostly qualitative. Figure 42 is a plot of the regions of processing space from the multilayer pad geometry. Similar to the single bead geometries the yellow points denote lack of fusion porosity, the red points denote keyholing induced porosity, and green denotes no readily evident porosity.

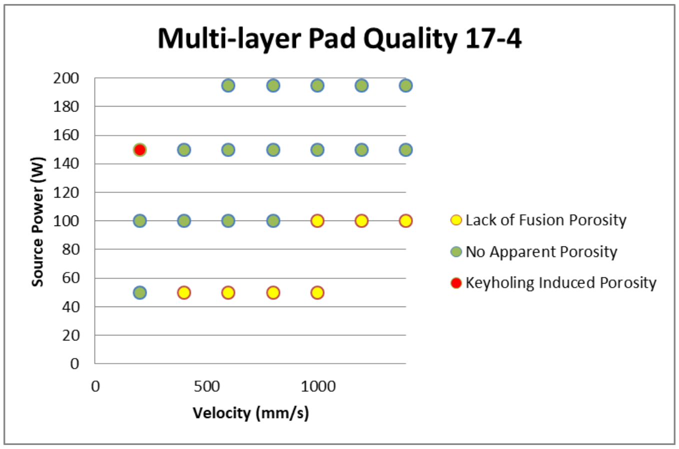

Figure 42: Quality of multi-layer 17-4 pads

The samples appear to have the defects that were expected from the single bead experiments. Points where undermelting was predicted to be an issue appear to have severe porosity and only partial interlayer adhesion. The porosity can be clearly identified as due to lack of fusion because of the shape and size scale on the order of at least one layer thickness or more as well as occurring on melt-pool boundaries while keyholing porosity is usually very spherical in nature since it is formed by trapping gas during solidification. [118]. Keyholing is occurring where predicted; however, as was seen before, no porosity appears to be evident at the magnification used for some of the points. The lack of porosity would make this type of weld highly desirable for fully dense parts. Examples of each of the phenomena can be seen in Figure 43.

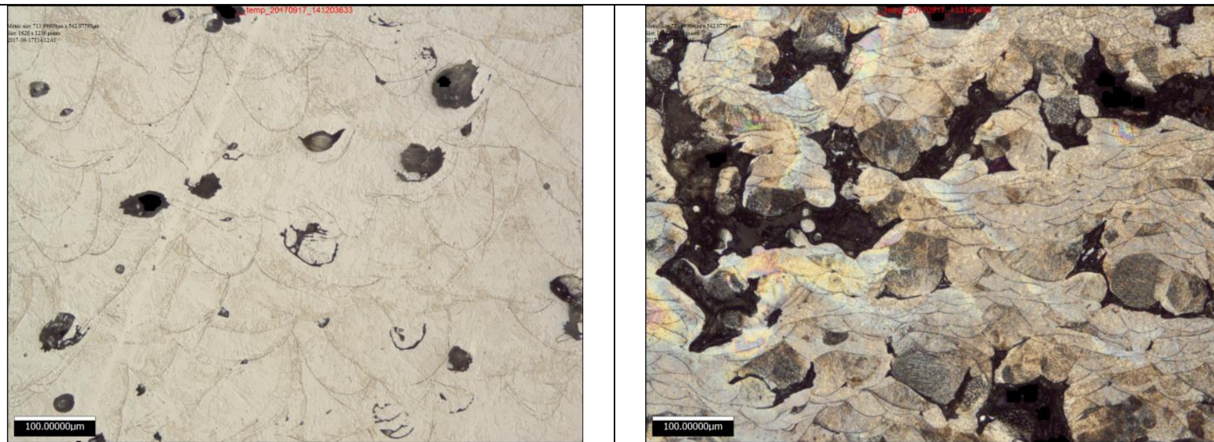

(a) (b)

Figure 43: (a) Keyholing and (b) lack of fusion induced porosity in 17-4 multi-layer pads

As this is a multi-layer build spreading can become an issue, although it can be somewhat predicted, there are ways to help minimize spreading issues within the EOS DMLS system. These parts were built with a tool steel recoater which will “hop” when it bumps into raised material, this “hopping” action can cause inadequate spreading. Using a carbon fiber “brush” style recoater or a soft recoater would mitigate this somewhat as the blade would deform rather than bounce. Other ways to help with spreading issues are to up the powder dosing factor to spread much more powder than is nominally required for the part to be produced. Upping the dosing is critical for high aspect ratio structures in particular because they tend to elastically deform and “throw” powder when the blade passes, spreading extra powder allows the bed to back-fill and reduces the powder deficit.

3.3.4 Conclusions

17-4 Stainless Steel was process mapped for melt-pool geometry in the L-PBF process. Simulations were done and fitted to experiments using an effective absorptivity. It was found that varying the effective absorptivity from 0.44 to 0.52 depending on the curves of constant area resulted in the best fit. This is thought to be because of melt-pool surface area and how much is at an elevated temperature with a higher absorptivity.

Experimental results from both the M270 and M290 at CMU were used and the results agree well between machines, which show that transfer between (properly calibrated) equipment can be accomplished. Parameter development can be performed on one piece of equipment and transferred successfully, with minor tweaks, to other equipment.

Single layer pads were skipped for this alloy system and it was shown that by doing so one can immediately go from single bead geometries to bulk components. The issues seen in single beads directly translate to bulk. It should be noted, however, that when skipping single layer pad geometry there is a potential to miss features that might have otherwise been detected (i.e.: keyholing due to localized preheating, or hatch spacing related defects).

A novel discovery was found within the multilayer deposits of 17-4 which show that in certain regions of P-V space the cooling rate is such that the microstructure becomes strongly magnetic. This is potential implications in designed or “programmed” magnetism within a single part and is beyond the scope of this work.

With 17-4 it is again seen that a single layer of powder does not appear to influence melt-pool geometry. This agrees with the results seen previously with IN625. It is believed that this is likely due to the thin layer thickness of the powder material in relation to the bulk material substrate.

When comparing the experimentally produced process map for 17-4 and IN625 the results are extremely similar for the two alloys, this is promising because it shows that if you have a process map for an alloy that is similar thermally it can be a good starting point for producing a new process map for a new alloy. Key differences are noticed between the quality melt-pool regions, and the balling regions, for the two alloys.

Chapter 4 Effects of Powder

4.1 Overview

Powder has drastically different thermal properties than bulk material which results in an insulating effect and thus a larger melted area than originally predicted [71]. From the previously presented work it was shown that powder has little influence on melt-pool geometry at 20 μm layer thickness for both IN625 and 17-4 stainless steel. This chapter examines the effects of increasing powder layer thickness on key melt-pool dimensions for IN625. Simulations are developed to determine how layer thickness affects the melted dimensions. Experiments are performed to validate simulations and to observe what non-thermal issues arise in practice. Conclusions are drawn as to when powder needs to be considered to properly predict melted dimensions and desired processing conditions.

4.2 Methods

Computationally the powder model was used in an attempt to predict melt-pool properties for varying layer thicknesses of powder. The model was run with a number of different layer thicknesses for the same, nominal, parameters that EOS uses by default for IN625. Layer thicknesses were chosen to span a wide range in an attempt to capture the steady state geometry where the melt-pool is purely surrounded by powder and has little to no thermal effect of any fully dense bulk material.

In order to experimentally examine the effect of powder layer thickness on melt-pool geometry, a custom build plate was created. This plate was designed to test multiple layer thicknesses of powder at once and preserve a known delta between thicknesses, even if the gapped distance is incorrect. A schematic of the test plan can be seen in Figure 44a. A wire EDM was used to face and cut 10 µm incremented steps into a 6” by 6” by ¼” IN625 plate, resulting in plate depths of 10, 20, 30, 40, and 50 µm. The wire EDM gave a ±2 µm surface finish with the cutting parameters used. The stepped features were positioned such that the recoater would spread through them rather than across, this was done to help avoid any potential spreading issues with the hard edge of the steps. An angled fiduciary was added to the bottom of the plate as well to serve as a locater. This plate was leveled and gapped to be 20 µm (resulting in a height range of 30-70 µm), similar to when starting a normal build and powder was spread across this. A single set of 40 single bead experiments were performed at each height. The repeated parameters in the same locations along the experimental plate allowed for direct comparisons between varying layer thicknesses and a redundancy if the plate was not exactly level the delta between the experiments at each height in the same location should be the same. Completed experimental plate can be seen in Figure 44b and the parameters chosen are shown in Figure 44c. It should be noted that the laser and experimental jig were not completely aligned in software so 5 melt tracks of each set were lost due to them lasing a high point rather than the trough at the correct height, resulting in a total of 35 single bead tests that are viable for analysis. The unusable parameters are highlighted in red in Figure 44c.

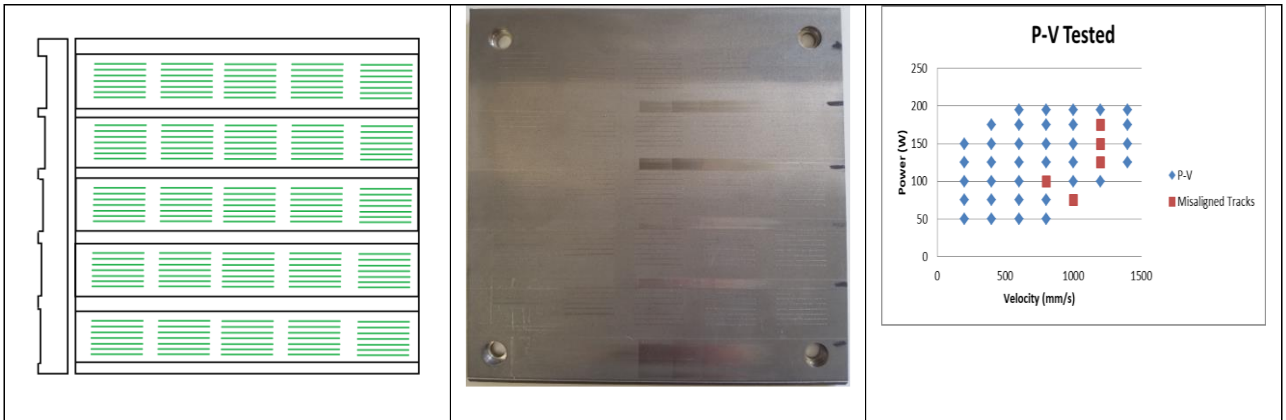

(a) (b) (c)

Figure 44: (a) Layer thickness experiment layout (b) experimental plate (c) parameters tested with failed parameters highlighted in red

The single bead tracks were first imaged using the Alicona InfiniteFocus for a length of 4 mm and then the image analysis program was run to calculate melt-pool widths from above. The plate was then sectioned using the wire EDM and the resulting samples mounted, ground, and polished (Again, according to Buehler procedures in Appendix A) and then finally etched using the electrolytic etchant found in literature [119], for cross-sectional analysis. The cross-sections were then examined under the Alicona InfiniteFocus to determine the cross-sectional measurements of the single bead geometries. The images were then measured using the image analysis tool, ImageJ.

4.3 Results

4.3.1 Modeling

The effect of powder can be seen mathematically by comparing the thermal diffusion length which is approximated by Equation 7 but this does not give the complete picture since this back of the envelope calculation is based on constant thermal properties throughout and only gives the penetration depth (L_{diff}) as a function of time (t) and thermal diffusivity (α), and not as a final value that may be reached given enough time since this assumes a constant flux. When the penetration depth is plotted for both the powder and the solid conductivities (Figure 45), it becomes readily apparent, that the powder will take a longer period of time to establish a melt-pool of the same size as with bulk material.

Equation 7: Thermal diffusion length

$$L_{diff} = 2\sqrt{\alpha t}$$

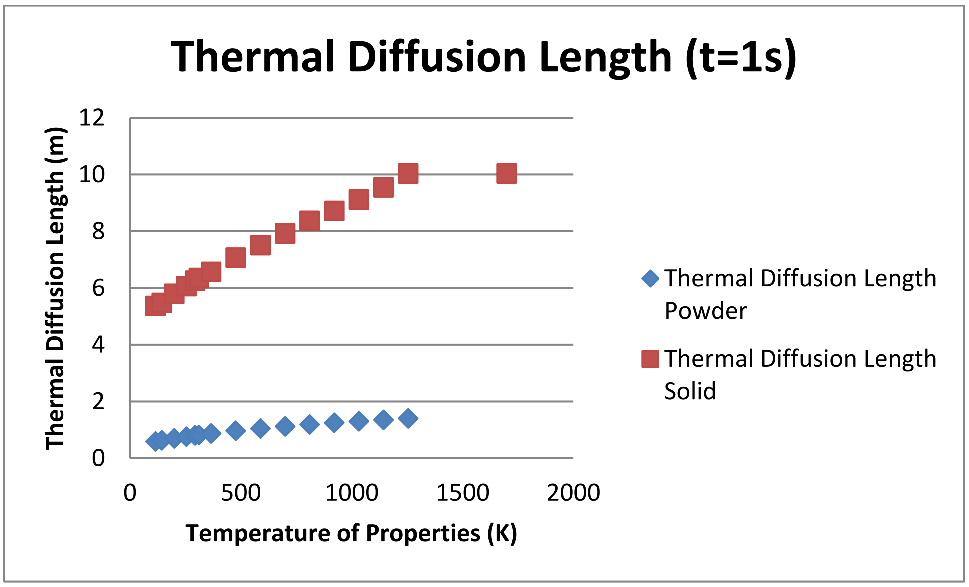

Figure 45: Thermal diffusion length for powdered IN625 compared to bulk IN625 (τ = 1 s)

From these results it appears there is quite a large influence that powder has on the problem, but this is counterintuitive to what has been seen through experimentation in the previous chapters. A more advanced model, such as the Rosenthal solution, can help explain the seemingly small effect of powder, by taking into account a moving heat source and other thermal properties. When we compare the Rosenthal solutions for a powder and for a bulk material the difference becomes more subtle and similar to what has been seen previously. The Rosenthal solution does not allow variation in material properties throughout the depth of the solution so some approximations must be made and the results are only an estimation of the final melt-pool geometry.

Applying the Rosenthal solution to the problem and setting the entire melted area to properties correlating to only powder the melt-pool depth dimension would increase by a factor of 1.44. This solution neglects the solidification of the powder into fully dense material and the difference in thermal properties that this imposes, but is a reasonable estimate to the behavior of the system as a whole when comparing powder to no powder. A better approximation would be to apply an effective medium model to the system. To do this the material properties were modeled as being a combination of the solid and powder values. If we assume that the powder comprises the top 20 µm of the semi-circular cross-sectional area of the material melted with fully solid material properties a rough ratio of powder to solid material can be calculated and applied as an effective conductivity. Applying this effective conductivity to the lased material gives results that start to become closer to what is being seen in experiments. The actual ratio will be dependent on the parameters chosen and the resultant melt-pool depth, but this gives a reasonable estimate. For example, if we choose a modest melt-pool depth of 70 µm with a 20 µm depth of powder, assuming a semi-circular melt-pool, this results in a cross-sectional powder to total area ratio of 0.36, which results in an 11% increase in width/depth calculations based on the Rosenthal model.

The trend in percent difference in area with the addition of powder from the solid material is of a quadratic nature when examining the analytical solution (Figure 46). This is in agreement to what is hypothesized since the percentage of the melt-pool that is comprised of powder increases nonlinearly. This is only half of the solution since using this model does not allow for the thermal boundary effect beyond the depth of the melt-pool, from intuition the solution will have to reach a steady state size eventually when the powder layer becomes thick enough that the solid material below is no longer contributing significantly to the thermal problem.

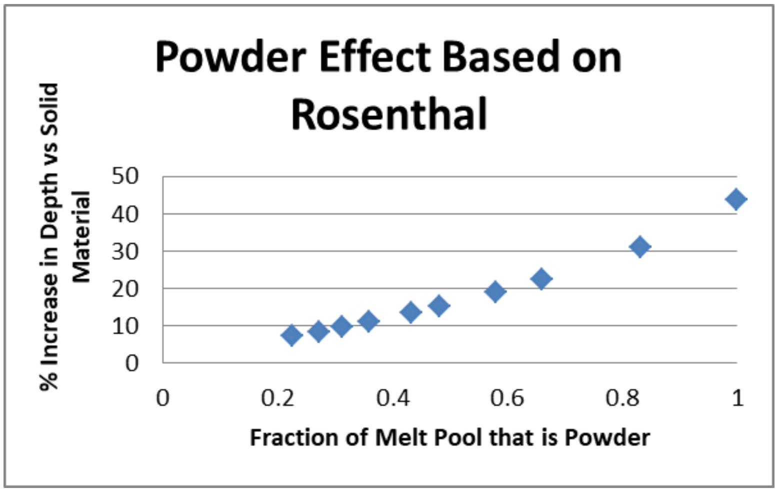

Figure 46: Effect of powder on melted depth based on Rosenthal Solution

The results from this model are in agreement with what was seen in the author's prior work showing that with smaller melt-pools there is a larger deviation in geometry, as the powder comprises more of the melted area. This difference is still not extreme because even when examining the melt-pools deposited on a pure powder bed, there is a significant portion of the melt-pool that is previously melted. Figure 47 illustrates the small fraction of a melt-pool (red outline) that is actively being seen by the heat source as powder (blue area), compared to the large fraction that is previously melted (magenta area) due to earlier melt-pools (black outline). The size of the blue area will be dependent on the thermal lead for the heat source, so will depend on laser velocity and thermal conductivity of the powder.

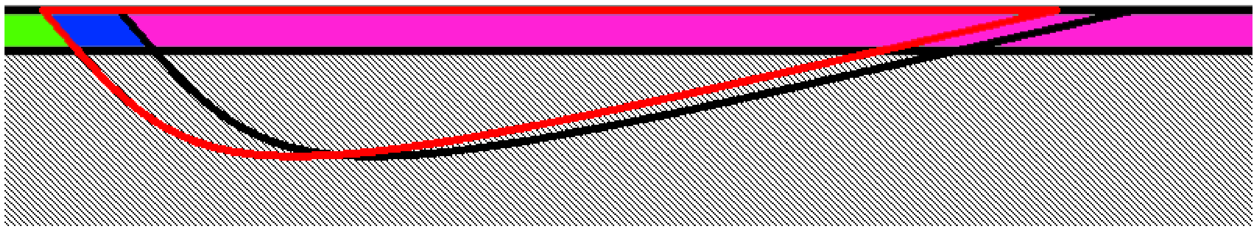

Figure 47: (Blue) Melt-pool fraction that is powder during deposition, (Red) New melt-pool, (Black) previous melt-pool, (Pink and Gray) solid material, (Green) powder

Simulations were run where the powder layer thickness was varied from 20 µm to 300 µm (Figure 48). These results give a curve similar to what is expected from the analytical solutions in a cubic type function. With small increases in powder layer thickness there is only a slight increase in the melted depth and area. With an increase in powder depth of 50% of the melted depth gives around a 10% increase in melted cross-sectional area. Depth changes are negligible until extreme layer thicknesses are utilized. There is an inflection point where the system starts to equalize and result in a steady state geometry regardless of the thickness of the powder layer. This makes intuitive sense because the melt-pool cannot infinitely increase in size for a given heat flux input.

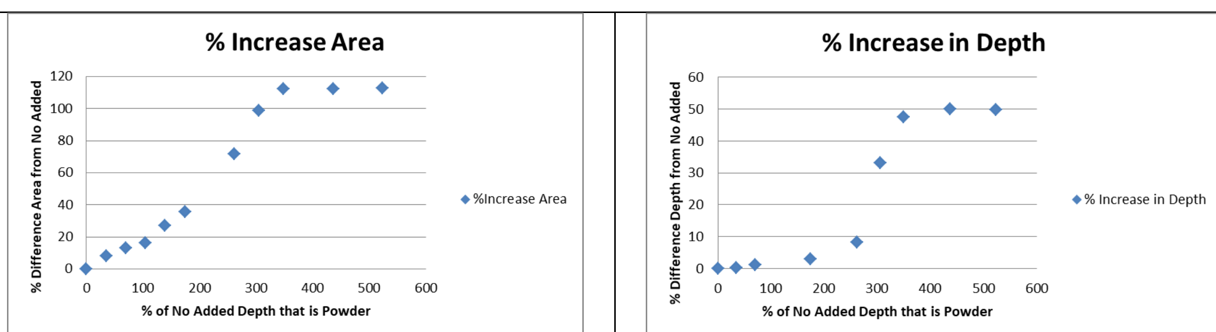

(a) (b)

Figure 48: Percent increase in (a) Area and (b) Depth with the addition of powder compared to no powder added from simulations

It can be seen readily from the plot in Figure 48 that as powder depth increases the melted area also increases, this is intuitive since the powder has an extremely low thermal conductivity compared to the bulk material. The melt-pool shape changes slightly because of the varied thermal constraints and this makes the portion of the melt-pool that is created on the powder slightly wider. Figure 49 shows an example comparison of two identical processing parameters but varied powder layer thicknesses.

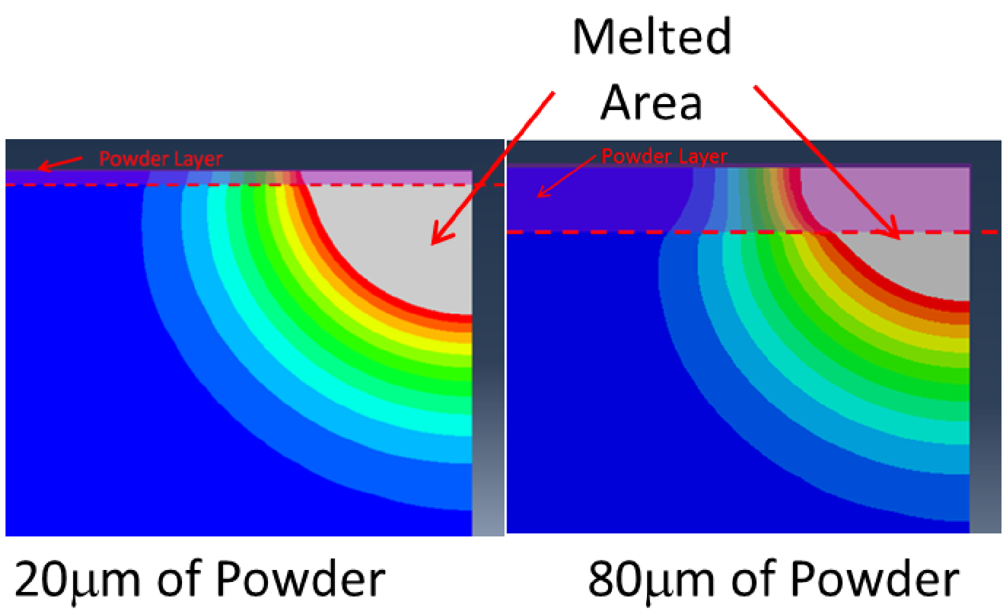

Figure 49: Simulation comparing the effects of powder on melt-pool cross-sectional geometry

If we vary the process conditions below (200 mm/s slower) the nominal parameters, the curve shifts slightly down (Figure 50). This new parameter combination results in a 37% larger melted area for no powder added than nominal. Since the curve is normalized and the heat transfer should be similar regardless of melt-pool size this curve should be comprehensive of the trend throughout processing space. This changes, in reality, with the effects of radiation and convection, with a larger melt-pool (lower velocity or higher power) there is more area at temperature that is acted upon by these heat transfer mechanisms and thus the plot will be scaled and shifted. The overall shape of the curve should remain the same.

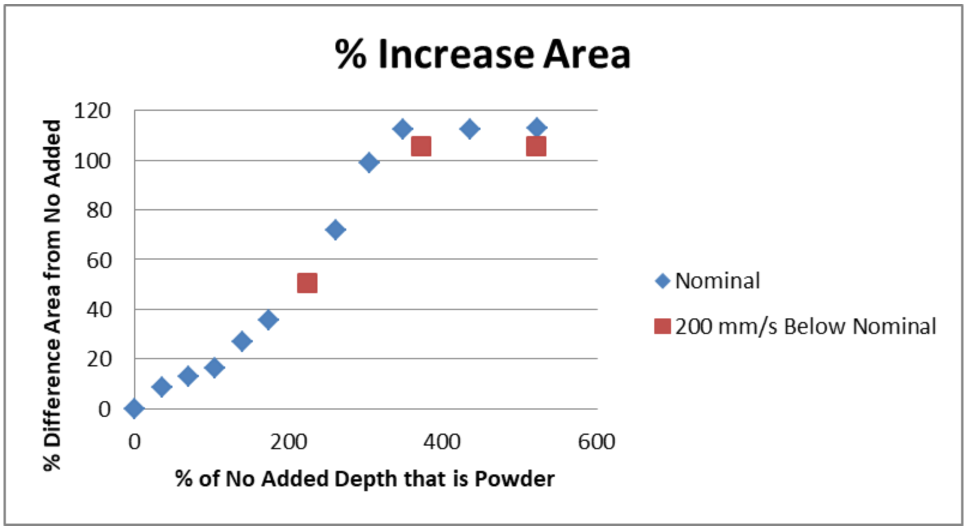

Figure 50: Effect of varying velocity on the cross-sectional area with increasing powder layer thickness

From the simulations and Rosenthal it became apparent that when powder is a significant portion of the melt-pool depth the length of the melt-pool increases significantly. This increase results in a lower “bead-up” threshold and thus overhanging structures will potentially have failure modes in the “bead-up” area much sooner than predicted from the nominal single beads with small amounts of powder. The bead-up will also increase due to the different wetting conditions provided by a purely powder substrate, although this is not modeled here. The process maps produced from a Rosenthal solution (fitted to simulation results) for a completely powder case vs a no powder case can be seen in Figure 51. These plots increase by a factor of four in the same regions of processing space. The increase in length will also increase the solidification time for a given velocity, these are also shown in Figure 51. This increase in solidification time will change the microstructure of the resultant bead, however, with layer thicknesses less than 100% the nominal melt-pool depth simulations predict that the increase in solidification time is less than 10%, and thus can be considered negligible for thin layers. For layer thicknesses beyond this, the solidification time will increase rapidly due to the insulating nature of the powder.

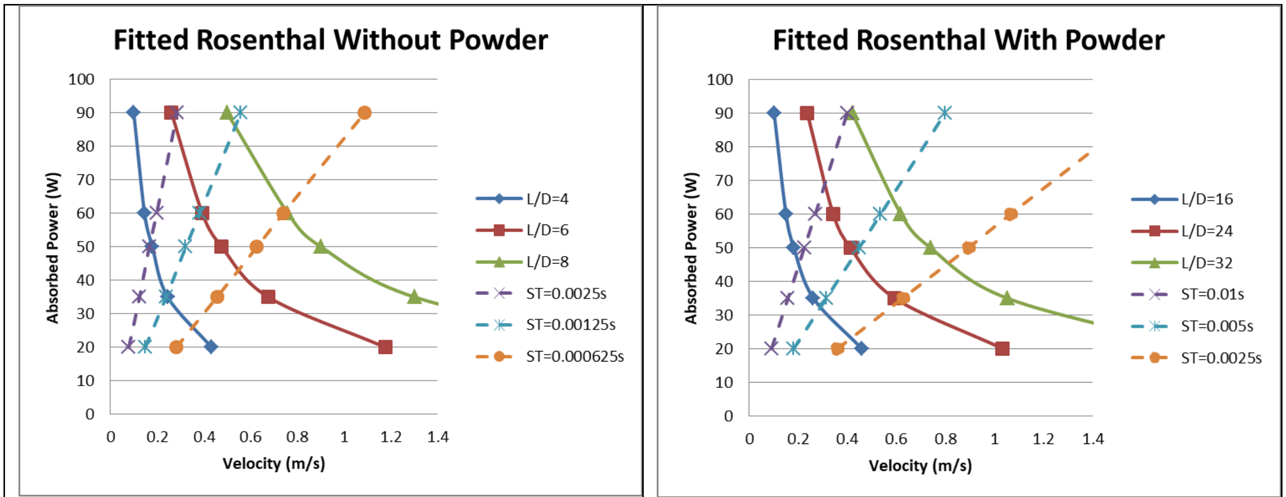

(a) (b)

Figure 51: Process map produced by fitting Rosenthal to simulations showing lines of constant solidification time and curves of constant L/D ratio for (a) no powder and (b) completely powder cases

4.3.2 Single Bead Widths

From experiments no noticeable trend in width with increasing powder layer thickness was observed. The data was roughly horizontal as the layer thickness of the powder increased from 30-70 µm. A representative measurement can be seen in Figure 52 and Figure 53 with data points being inconsistent but generally appearing to have little trend in either direction with increase in powder layer thickness. With smaller melt-pools produced at smaller powers seem to have a higher variation. This is likely just due to the small weld bead size and less to do with the powder itself since the variations are throughout the range of layer thicknesses tested. The remaining plots can be found in Appendix B. All error bars are 2 standard deviations above and below the average that is reported.

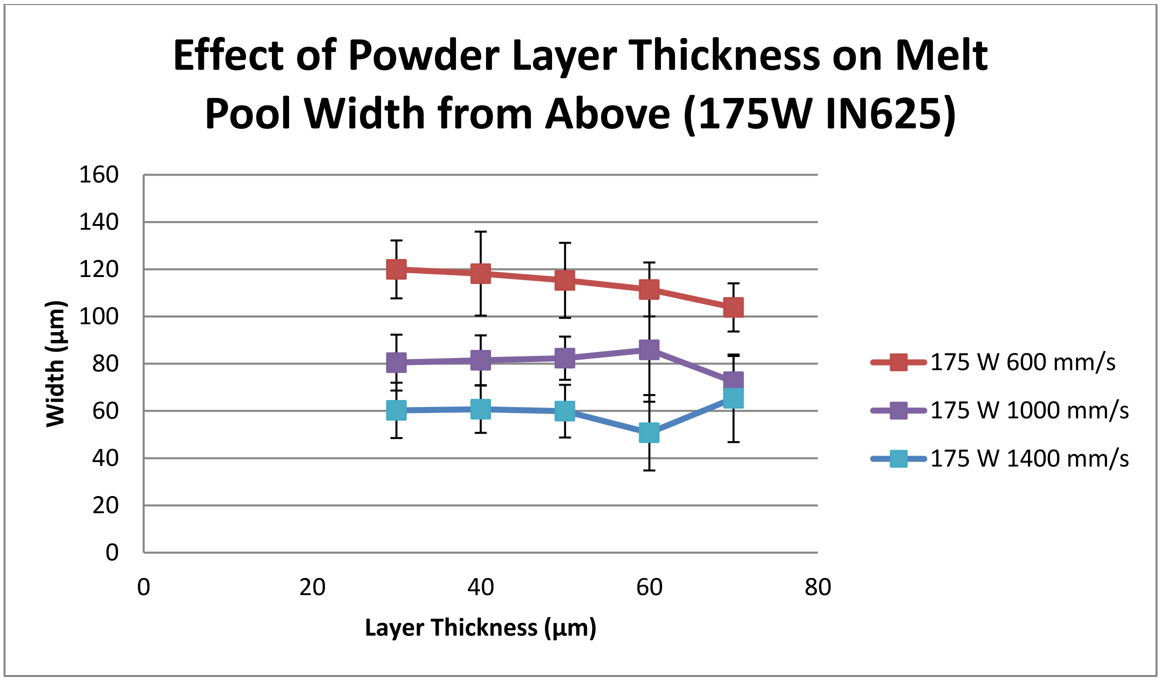

Figure 52: Effect of powder layer thickness on IN625 melt-pool width from above (175 W)

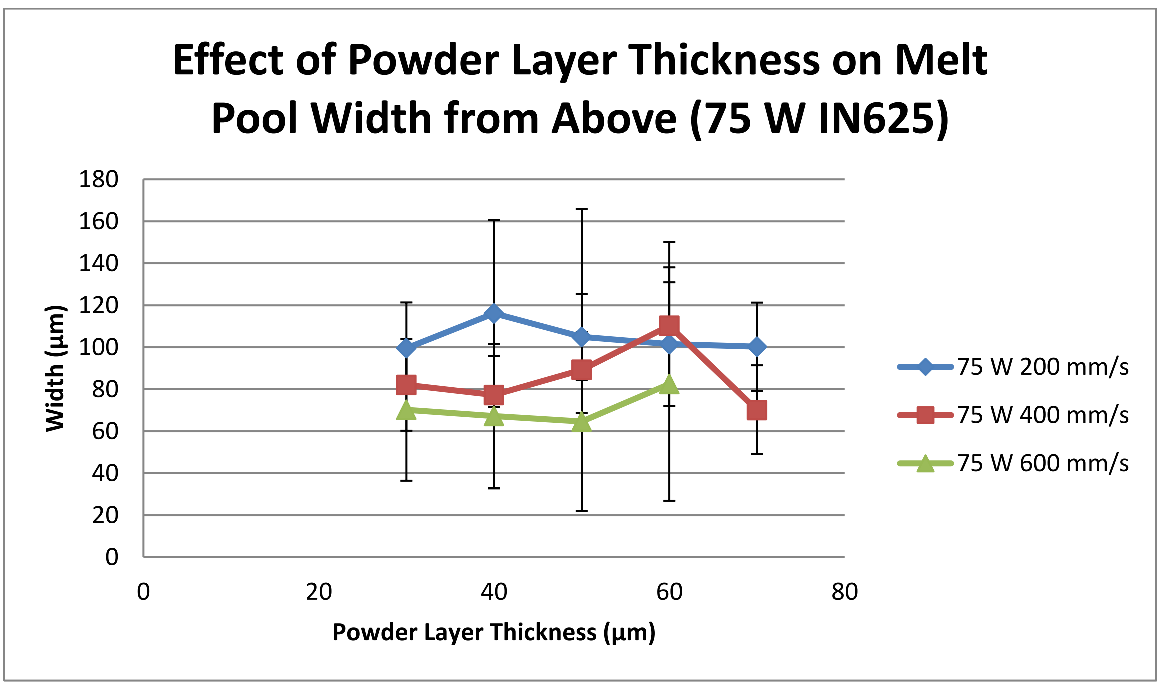

Figure 53: Effect of powder layer thickness on IN625 melt-pool width from above (75 W)

It is difficult to quantify the "bead up" phenomenon in these experiments due to the ability for many melt tracks to delaminate. The lack of a substrate to provide a surface to wick onto and affix the weld bead results in a more spherical weld bead when the layer thickness is increased (Figure 54). This is not ideal for building most parts since it will likely result in lack of fusion porosity within the part that may serve as crack initiation sites and lead to premature part failure.

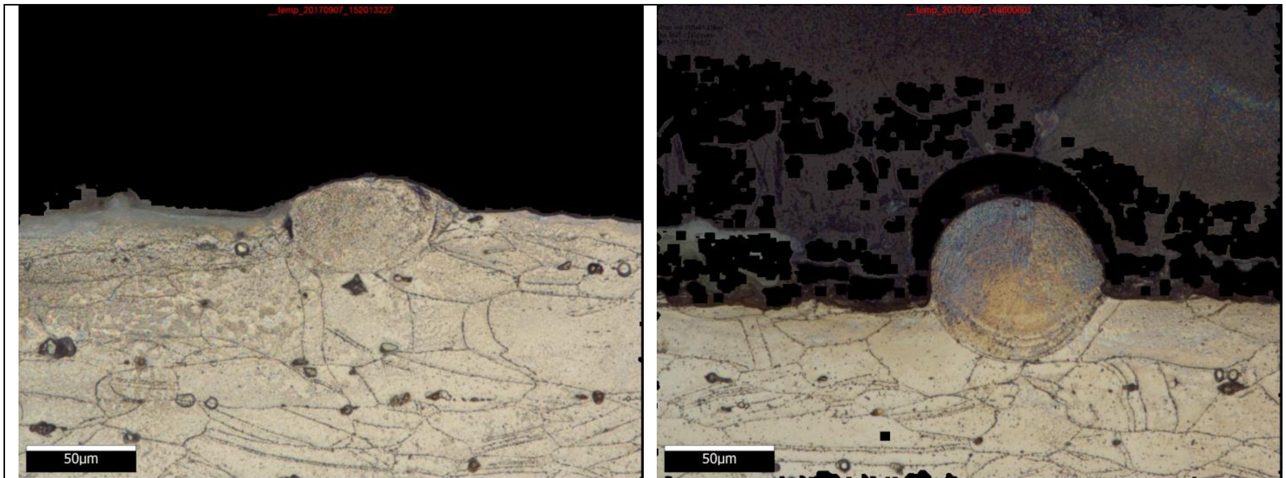

(a) (b)

Figure 54: Balling phenomenon for increasing layer thickness (a) 30 µm and (b) 70 µm of powder

A byproduct of the "bead up" occurring can result in discontinuities in the melt track. Of interest is the increase in the presence of discontinuous melt-pools with increase in powder layer thickness. This is from surface tension effects and the wettability of the powder layer compared to the baseplate [18]. This makes sense given that the powder layer, being composed of particles, is not physically uniform and thus the melt-pool cannot be exactly the same, so smaller melt-pools than the nominal powder layer thickness show discontinuities rather than no melt track at all. Other causes for this are slight fluctuations in the laser power or velocity resulting in inhomogeneous melt tracks.

4.3.3 Single Bead Depths and Areas

Melt-pool quality was examined for each layer thickness. As layer thickness increases the region of space that exhibits keyholing appears to increase since the melt-pool depth seems to increase slightly. This is not necessarily detrimental to using larger layer thicknesses but it is something that must be considered as it is a potential source of porosity [118]. If the solidification rate is slow enough to allow any pores formed to escape the molten bead the porosity issues can be mitigated. Since the processing window is already extremely narrow, the addition of powder seems to close that window so that operating without keyholing is much more difficult, while undermelting still remains an issue. An example of the same processing parameters for three different layer thicknesses can be seen in Figure 55, with little noticeable difference in melt-pool geometry.

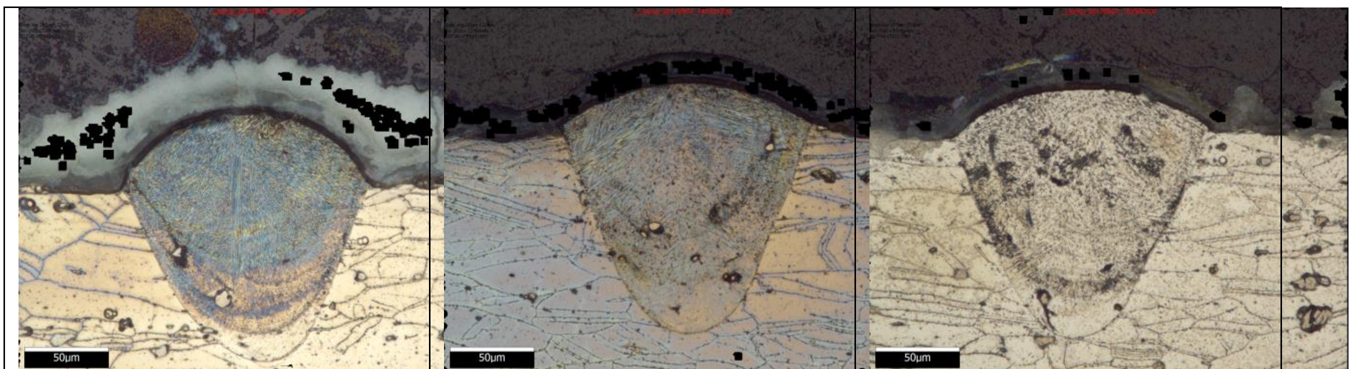

(a)	(b)	(c)

Figure 55: The same processing parameters for three different layer thicknesses: (a) 30 μm, (b) 50 μm, and (c) 70 μm

The melted depths vary only slightly as powder layer thickness increases, similarly to the above view widths. The smaller melt-pools again have a high variation but appear to be roughly consistent with increasing layer thickness. Two representative plots can be seen in Figure 56, additional plots can be seen in Appendix C.

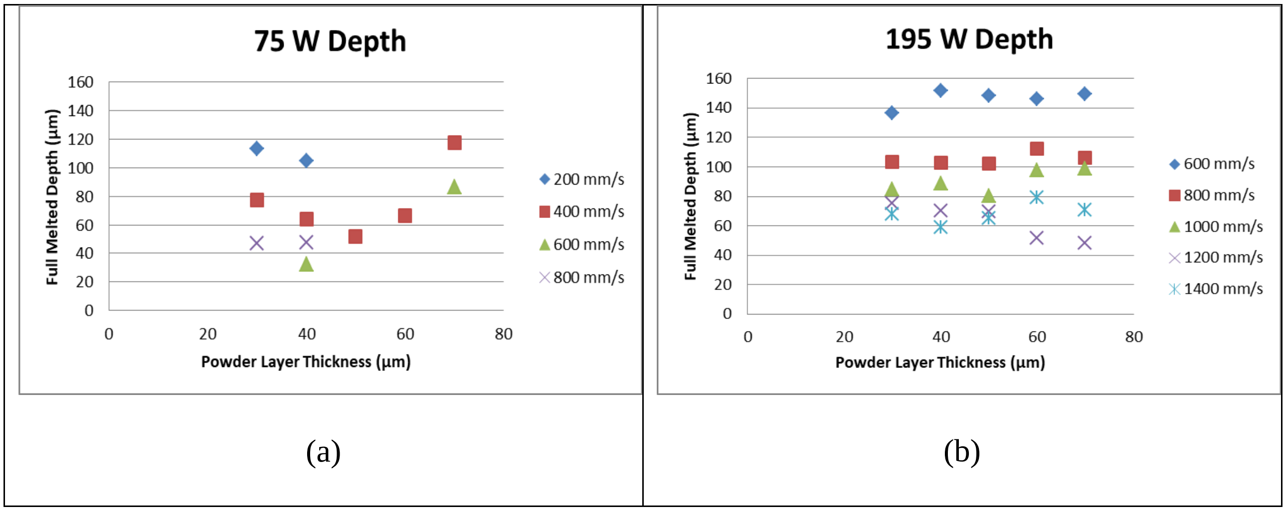

Figure 56: Effect of melt-pool depth with increasing layer thickness for (a) 75 W and (b) 195 W

Single bead areas were measured for the various layer thicknesses and P-V maps were produced for each of the layer thicknesses. The area data becomes more scattered with increasing layer thickness, due to higher variability and a decrease in the available data points. Figure 57 illustrates that the trends are in similar regions of processing space for curves of constant cross-sectional area. As area decreases, the variability between layer thicknesses seems to increase but this is also intuitive since a smaller melt-pool has a larger portion that is powder, during melting, than a larger melt-pool.

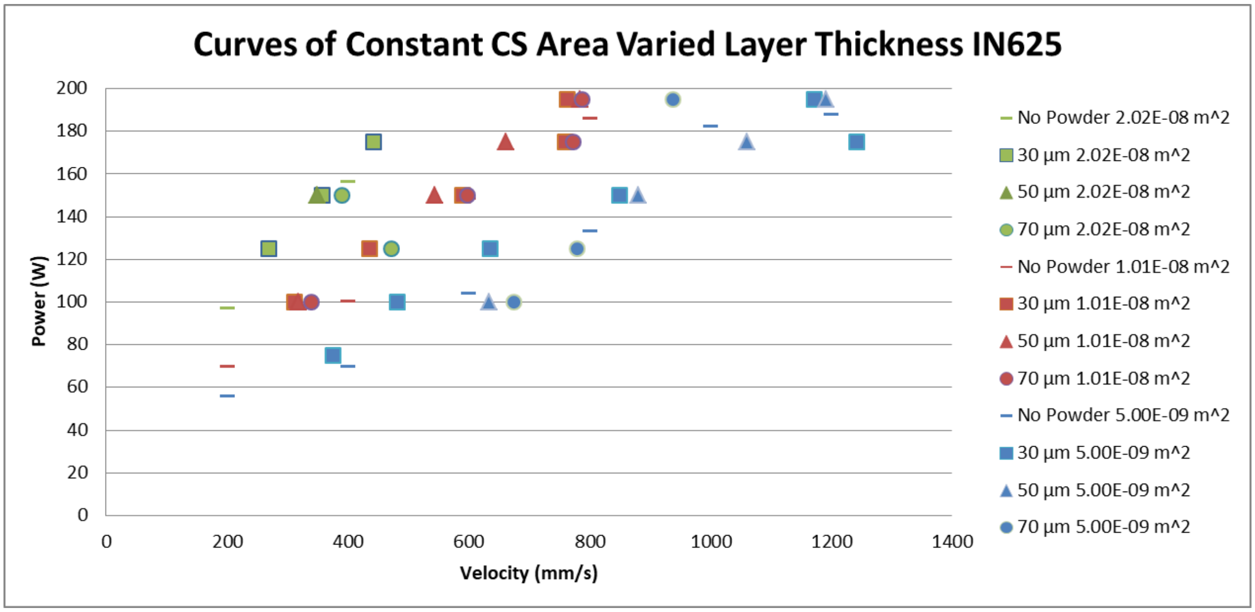

Figure 57: Curves of constant cross-sectional area with varied layer thickness

As powder layer thickness increases the area only slightly increases. This aligns with what was predicted from previous experiments with single layer of powder and the simulations run. There appears to be a lot of variability with melt-pool dimensions with the low power cases (where melt-pools are smaller).

Many of the low power cases result in melt-pool discontinuities with increasing powder layer thickness. Figure 58 compares the same power and velocity but with different powder layer thicknesses (30 µm and 70 µm, respectively), the melt-pool starts to become discontinuous with increased powder layer thickness.

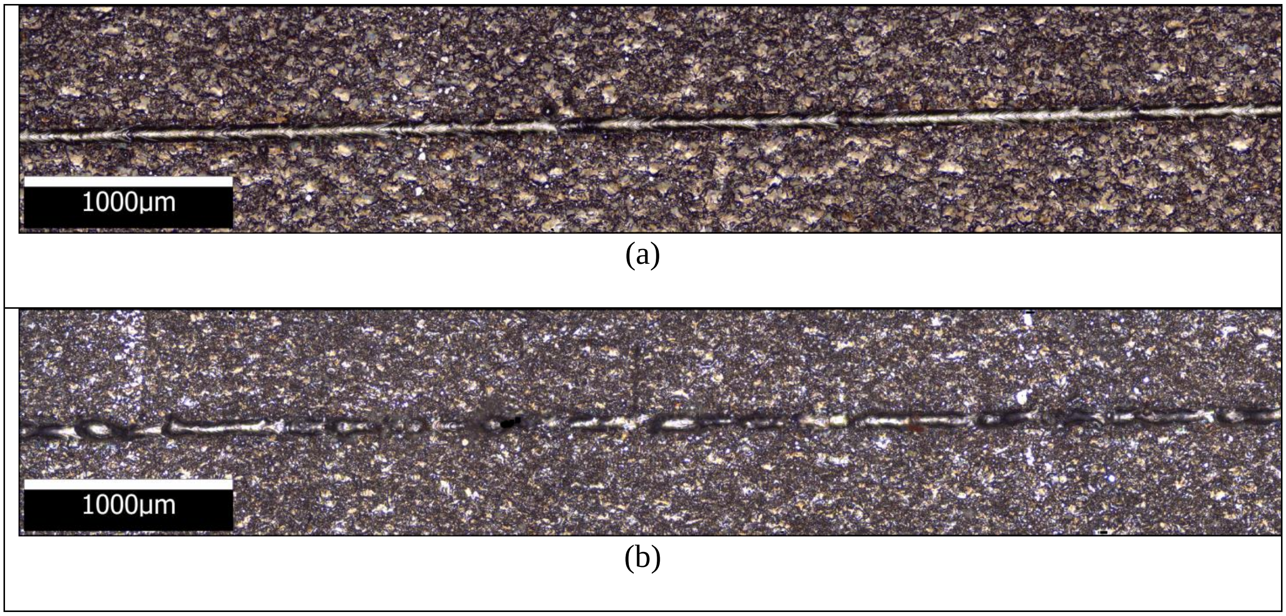

Figure 58: Increased melt-pool discontinuities for the same parameters (50 W, 400 mm/s) with increase in layer thickness (a) 30 µm and (b) 70 µm added powder

The reason there is only a small difference in the area is because as mentioned previously the amount of powder actually being seen by the laser in this process is minimal. When the powder layer is thick enough to cause significant differences, according to simulations, the beads won't weld to the substrate at all, and this was not under investigation with this set of experiments. The laser absorption isn't affected a great deal because except at extremely high velocities the laser only hits molten material, based on simulation results. The powder acts as insulation to the melted material and thus concentrates the heat longer, resulting in a larger melt-pool.

Analysis of the microstructures produced with various layer thicknesses is beyond the scope of this work and the time available (since extensive SEM analysis is required) but could prove interesting. From the geometry not changing greatly for small layer thickness increases, it can be inferred that the microstructure will not differ greatly. When the powder depth is approaching or exceeding the penetration depth of the weld the microstructure may start to be affected a greater deal due to the highly insulated boundary conditions and thus slower cooling rates.

4.3.4 Conclusions

Mathematical modeling, both analytical and computational, of the addition of powder shows that for small amounts of powder relative to the melt-pool depth results in relatively small changes in melted area. The modeling also revealed that the melt-pool length increases by a factor of four when depositing on a powder bed (where layer thickness no longer has an effect) compared to depositing on a bulk material. The experiments compared to simulations seem to agree, although the experiments show that the surface tension and wetting physics play a large role in the final melt-pool geometry when the powder depth increases and becomes a significant portion of the expected melted depth predicted from no powder added experiments. The physical reasoning behind these effects is that although conductivity changes drastically, the specific heat does not, and since only small portions of material are being melted at a given time the density is only much lower for a small portion of the material. The conductivity being so low insulates the back of the melted track and thus results in a longer melt-pool when depositing on a pure powder bed.

From experiments, there was no noticeable trend in melt-pool widths or depths with respect to powder layer thickness as the points were roughly horizontal with minor fluctuations. The areas vary only slightly with increased powder layer thickness. The smaller areas show more deviation than the larger areas, however, for the majority of process space, the regions of processing space for a given melt-pool dimension are not shifting any great amount. This means that if an operator runs single bead experiments to determine regions of processing space that these results will directly scale to a wide range of layer thicknesses. Since the keyholing and bead-up regions shift slightly with increasing layer thickness it should be noted that the resulting melt-pool shape may not be quite the same as predicted from single bead no powder experiments, however should be close for mild increases in layer thickness.

Another benefit shown from these results is that if an operator does not correctly level their build plate, as long as the overall level does not change a great deal, the build should progress fine for the first layer until a true level is achieved with the next recoat.

Chapter 5 Effect of Overhanging and Cellular Structures

5.1 Overview

Previous chapters have discussed the effect of powder layer thickness on melt-pool geometry. This chapter presents work on applying that knowledge and simulation tools to overhanging geometries and cellular lattices. Horizontal structures are often thought to be unable to be produced by L-PBF without support structure; however there are many cases where support is undesirable or impossible to be implemented and maintain design intent. This work aims to produce unsupported horizontal structures by varying process parameters. Three overhanging geometries are investigated to simulate internal structures where support would not be feasible. An attempt is made at determining a universal processing parameter to use when producing overhangs and what conditions will optimize the surface finish. Finally the work is applied to cellular lattice structures in an attempt to allow both larger and smaller size scales to be produced.

5.2 Methods

5.2.1 Finite Element Model

A simulation was created that accounts for the first overhang geometry. This simulation took considerable time, on the order of a month, to run due to the size of the model needed to get the required resolution able to model the melted geometry accurately throughout the process. The model mimics multiple raster passes between two already built up surfaces, such as is occurring when depositing a lattice structure (the first raster pass) or overhang geometry 1 (subsequent raster passes). An illustration of the simulation geometry can be seen in Figure 59 with the important features labeled. The flux steps through the model in a similar fashion to what was done in previous models and will delay at the end of a raster pass to allow for the cooling that happens during the “skywriting” portion of the deposition process. Skywriting is a programmed time delay where the laser is turned off that is implemented within the EOS process in order to allow the beam time to slow, reverse direction, and achieve the desired velocity without affecting the melt track. This type of model is able to show both thermal trends and melt-pool geometry as the overhang is built.

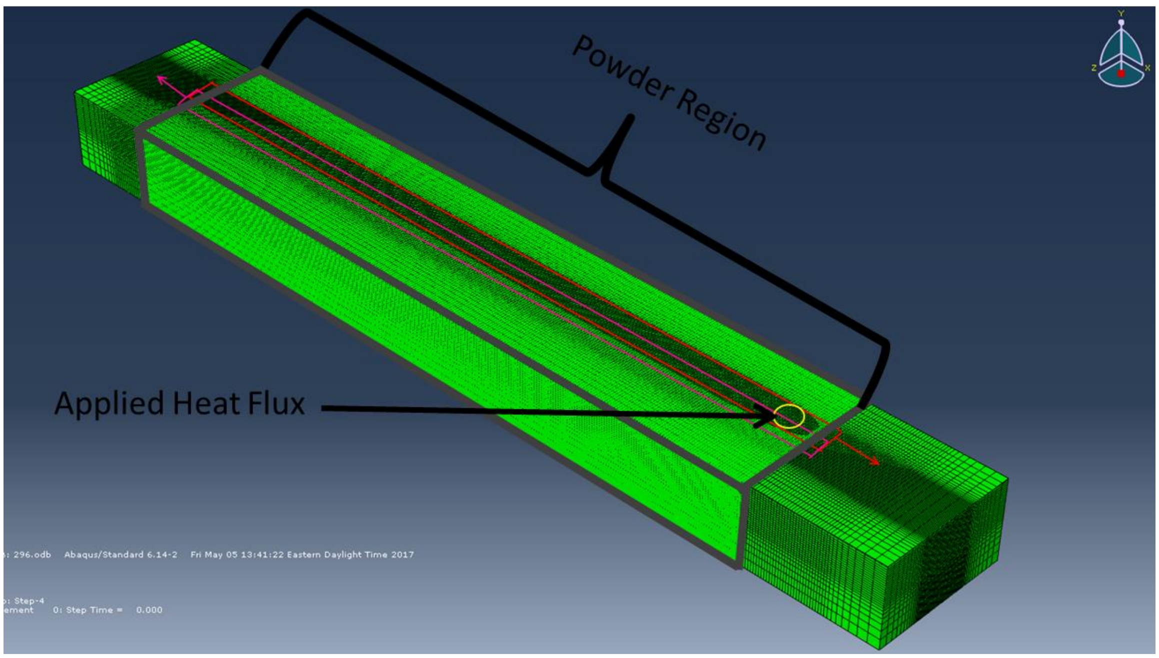

Figure 59: Simulation for overhanging structures at melt-pool level

Another type of simulation was created to better understand the heat conduction path and residual heating of the overhanging powder because of the input heat. This model is not refined enough to show a reasonable melt-pool geometry, however it does roughly approximate the heat buildup during the rastering process with powder. To accomplish this, the flux input is modified to be an equivalent line of heat flux that covers the entire length of a single bead scan track, then stepping this line of flux along the raster direction. After each flux application there is a 300 μs delay (measured using the high speed camera equipment at CMU) to simulate the “skywriting” step that is present in the EOS process. An illustration of this is shown in Figure 60. To analyze this type of simulation, the temperatures along the centerline on the top surface of the material were analyzed for each raster pass and the peak temperature recorded after skywriting. Simulations of this type did not account for radiation and convection for the results presented here due to computational time constraints. Inclusion of the radiation and convection terms would lower peak temperature values however the trends should still remain the same.

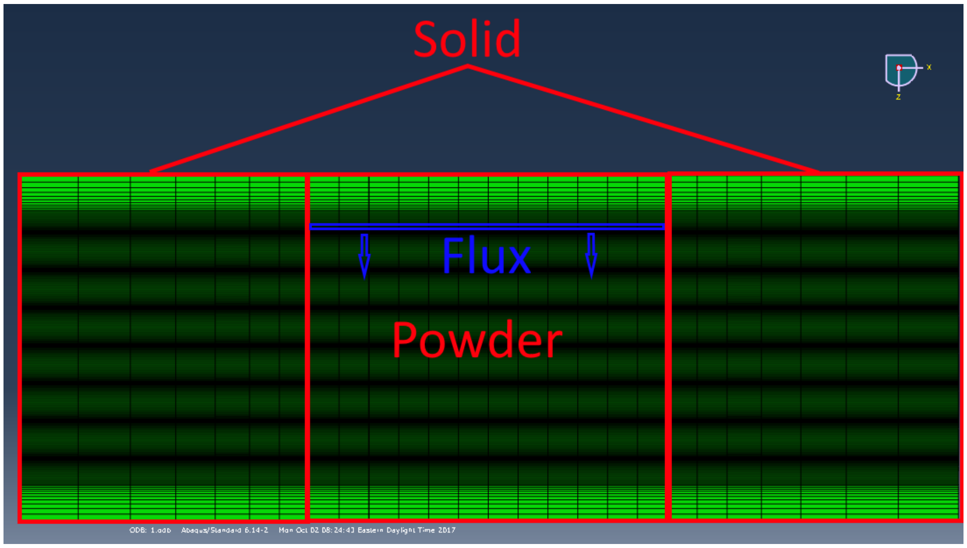

Figure 60: Simulation for overhanging geometries at raster pass level

5.2.2 Experiments

All of the experiments in this chapter were performed on IN625 to build upon the work in the previous chapter. These resulting behaviors should translate to other alloy systems as well, although the cutoffs will be different.

Overhang Geometry 1

This geometry was chosen as it simulates the roof of an internal channel (i.e. constrained on two sides). An application example for this type of overhang would be a wave guide. Overhang geometries 1 and 2 are both tested throughout P-V space in order to see what, if any, affect that parameters have on the buildability of an unsupported geometry.

The samples were created to have a 10 mm by 12 mm overhanging area that was supported by a strut on either side. The geometry can be seen in detail in Figure 61. This size was decided upon based on literature that showed difficulty in producing unsupported overhangs with spans longer than 5 mm [84].

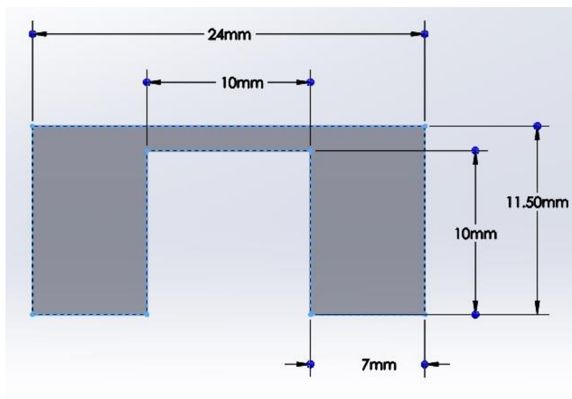

Figure 61: Overhang geometry type 1

This geometry was actually run twice, but due to catastrophic failure (Figure 62) the first build was not analyzed beyond what parts built and what did not. These experiments were re-run with the parameters that were not catastrophically failing and these results are presented in the following sections. It was found that the “Y” raster direction, or the direction perpendicular to the overhanging direction, nearly always broke during deposition due to residual stresses resulting in warping of the part before a layer was complete. The exception to this condition was when the power was low (50 W), this is thought to be because of lower residual stresses coupled with lower melt-pool lengths. The parameters for both tests can be seen in Table 4 with the second iteration parameters highlighted in green.

Figure 62: Failed first iteration of overhang geometry type 1 experiments

Table 4: Overhang geometry type 1 experimental parameters (Green highlight denotes run for second attempt)

Power (W)	Velocity (mm/s)	Hatch Spacing based on overlap of 30%	Orientation	Comments
50	200	70	x	
50	200	70	y	
50	400	50	x	
50	400	50	y	
50	600	40	x	
50	600	40	y	
50	800	40	x	
50	800	40	y	
100	200	130	x	
100	200	130	y	
100	400	100	x	
100	400	100	y	
100	600	70	x	
100	600	70	y	
100	800	60	x	
100	800	60	y	
100	1000	50	x	
100	1000	50	y	
100	1200	50	x	
100	1200	50	y	
150	600	90	x	
150	600	90	y	
150	800	70	x	
150	800	70	y	
150	1000	60	x	
150	1000	60	y	
150	1200	50	x	
150	1200	50	y	
195	600	110	x	
195	600	110	y	
195	800	100	x	Default Raster
195	800	100	y	Default Raster
195	1000	80	x	
195	1000	80	y	
195	1200	60	x	
195	1200	60	y	

Since the specimens were built directly onto the build plate it was required to remove them with a saw. Doing so without a stress relieving heat treatment, however, could damage the specimens and void the experimental results. To combat this, a stress relief heat treatment was performed in an inert gas furnace at 1065 °C for 1.5 hours before removing the samples from the plate [120].

To analyze the samples the specimens were placed inverted under the Alicona InfineFocus microscope and imaged along the middle, front, and back edge of the sample. These images were used to produce a 3D contour of the surface within the Alicona software based on focal points of the optics. In addition to these three profiles, a profile from front to back was also created. These profiles were input into MATLAB and analyzed for max difference between heights and other features to quantify the flatness and produced surface finish.

Overhang Geometry 2

This geometry was chosen as it simulates an internal rectangular pocket, as well as constrains the geometry better than the channel geometry (i.e. constrained on 4 sides). This type of geometry is indicative of what would be seen in wave-guides and internal cavities.

The geometry design for the second type of overhang experiments was a series of 10 mm by 25.4 mm pockets wire EDM cut into a surface ground ¼” thick plate of IN625. The further distance was chosen to try and mitigate edge effects from samples and give a larger overall unsupported area for analysis of the dross formation. The designed plate can be seen in Figure 63 with relevant dimensions. Note that the pockets were required to be connected due to the lack of EDM experience and difficulty in drilling a large number of start holes in the Inconel material. Connecting the slots resulted in a weakening of the plate that could have influenced results to a small degree. The connected slots potentially allowed parameters that would fail to have succeeded by warping the plate to accommodate the stress rather than breaking away from the base plate entirely.

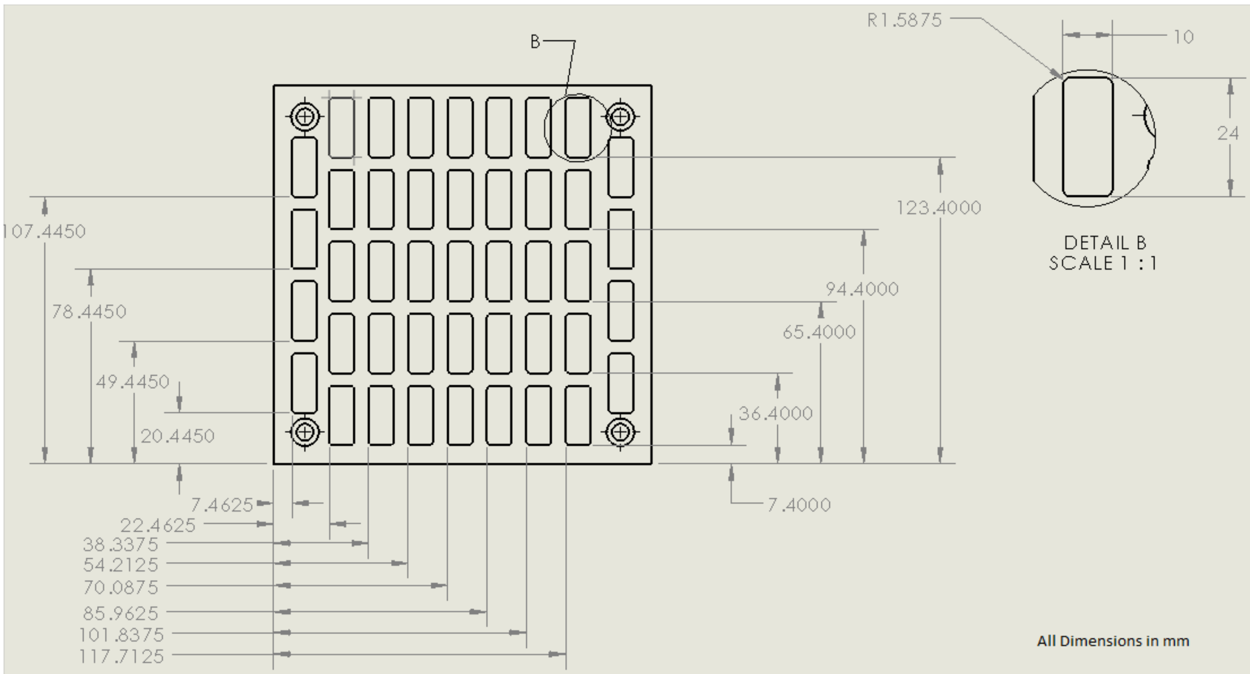

Figure 63: Overhang geometry type 2

The experimental plate was affixed to a modified base plate in the EOS M290 at CMU (Figure 64). All of the pockets were then filled with powder via spreading multiple passes. This was in an attempt to replicate packing of powders under an overhang for a real part. The plate was then gapped to be 20 µm and a final layer of powder was spread. The system then lased 36 different P-V combinations onto the plate (

Table 5). From the previous overhanging geometry experiments it was decided that only the 'X' raster direction would be tested. The logic behind this was that 'X' and 'Y' in this configuration would be nearly identical thermally (other than span length) and that the 'X' direction was most successful in previous tests. The pads were oversized by 1 mm in every direction in an attempt to facilitate welding to the experimental base plate. The samples were only built to 10 layers tall because the recoater blade seized upon one of the specimens and thus didn't allow the build to continue. It was decided, that 10 layers was adequate for what was being investigated in these experiments since after this number of layers most likely a user would transition to a bulk parameter set instead of downskin, since nominally downskin is only the first 2-4 layers of a downward facing surface on a part.

Figure 64: Overhang geometry type 2 experimental plate

Table 5: Overhang geometry type 2 parameters

Power (W)	Velocity (mm/s)	Hatch Spacing (μm)	Comments
50	200	70	
50	400	50	
50	600	40	
50	800	40	
50	1000	30	
50	1200	30	
100	200	130	
100	400	100	
100	600	70	
100	800	60	
100	1000	50	
100	1200	50	
100	1400	40	
100	1600	40	
150	600	90	
150	800	70	
150	1000	60	
150	1200	50	
150	1400	50	
150	1600	50	
150	1800	50	
150	2000	50	
150	2200	50	
150	2400	50	Nominal Downskin
150	2600	50	
195	600	110	
195	800	100	Nominal Raster
195	1000	80	
195	1200	60	
195	1400	50	
195	1600	50	
195	1800	50	
195	2000	50	
195	2200	50	
195	2400	50	
195	2600	50	
150	2400	50	Nominal Downskin

No heat treatment was required as all of the samples were welded to a single removable plate. This was able to speed up the analysis of the experiments, although there is some residual stress that is evident in the X-Y direction. The resulting plate was imaged using the Alicona InfiniteFocus microscope. The profile along the x direction in the center of the pads was extracted from this data and surface information was gathered. Imaging of the entire pad area for the number of pads created would have been time prohibitive. For this geometry the flatness was again measured using the delta between the max and min points in the profile measured.

Overhang Geometry 3

This geometry was chosen as it simulates a circular cavity (such as would be seen on the end of a blind fastening hole), but also has applications in wave-guides, and constrains the geometry similarly to the rectangular pocket geometry however has a different thermal conduction path. The geometry chosen is a circular hole of diameter 12.7 mm EDM cut into a ¼" IN625 plate. The reason this diameter was chosen was to maintain consistency with the previous experiments by maintaining an average chord length of 10 mm similar to what was done with geometry 2. The test layout can be seen in Figure 65 with the parameters in Table 6. These parameters were decided on based on the previous experimental results. Duplicates of each parameter were created in order to observe any outlier parameters.

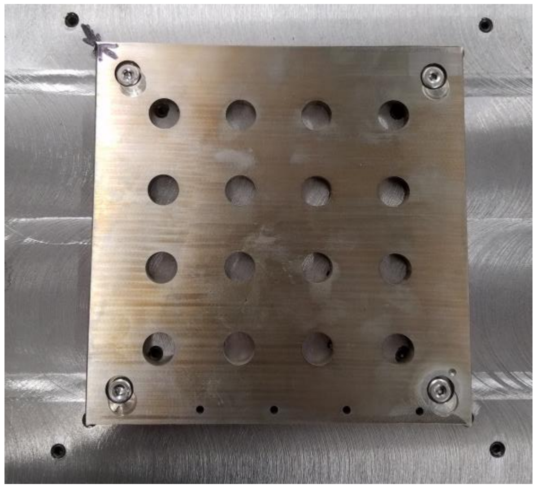

Figure 65: Overhang geometry type 3 experimental plate

Table 6: Overhang geometry type 3 experimental parameters

Power (W)	Velocity (mm/s)	Hatch Spacing (µm)
50	200	70
50	400	50
50	600	40
50	800	40
50	1000	30
50	1200	30
150	2400	50
195	800	100

The smaller overall area and lower quantity of pads allowed for full imaging of the samples using the Alicona InfiniteFocus to get data from the entire produced surface rather than only selected paths.

A low pass filter 800 µm wide in the X and Y (planar) directions was applied to the measurements to filter out the surface roughness and topological images were taken. 800 µm was chosen as the filter threshold since this was well beyond the size scale of hatch spacing effects and would allow the resulting profile to be seen clearly. The resulting topological features are indicative of what the surface looks like in terms of dross. A high pass filter with a threshold of 800 µm was applied to the data to determine surface roughness values for the samples as well. Surface finish was measured using the ASME B46,1-2002 standard provided within the Alicona InfiniteFocus software.

The bottom surface of the experimental plate was measured in addition to the deposited structure to be able to quantify the dross formed based on the known thickness of the experimental plate (7.31 mm). The raw data were averaged and then compared to the bottom surface and this gave a value of the dross that could be compared between the deposited overhangs.

Cellular Lattice Application

Cellular lattices with approximately 10 mm of strut length (Simple Cubic Lattice, 1.1 mm strut thickness) were designed using the Structures module in Magics by Materialise. A few of these lattices were produced in order to examine the application of the overhanging geometry parameters to these lattice structures. The experimental layout along with an example lattice can be seen in Figure 66 and the parameters used in Table 7. In order to correctly run these experiments, contour parameters are disabled.

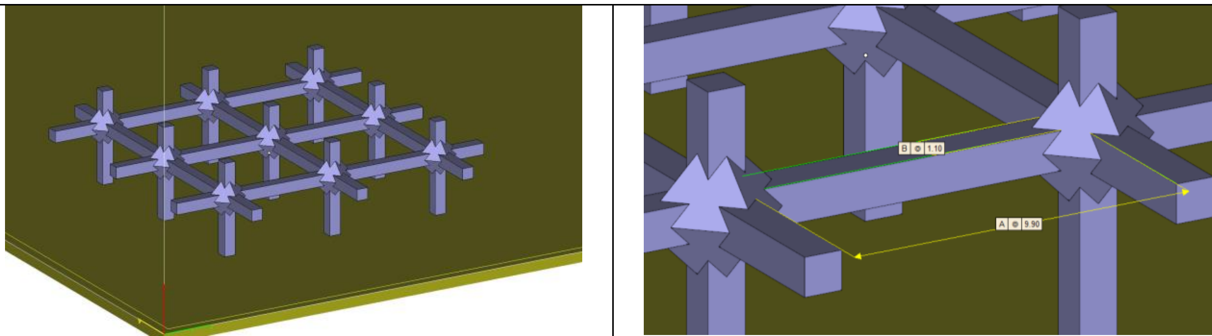

(a) (b)

Figure 66: Large cellular lattice design (a) full lattice (b) dimensions of struts

Table 7: Large cellular lattice test parameters

Power (W)	**Velocity (mm/s)**	**Hatch Spacing (μm)**
50	200	70
50	400	50
50	600	40
50	800	40
195	800	100

A second lattice structure was designed and built to test the lower unit cell size and application of the derived parameters. This lattice has an 80 μm wide strut spanning 320 μm. The parameter chosen to attempt this was 50 W at 1000 mm/s based on previous results this was thought to potentially give the best surface finish if it did not fail due to delamination and residual stress. An image of the designed lattice structure can be seen in Figure 67. The lattice is thin enough to require only a single laser pass, so no hatch spacing was specified for these experiments.

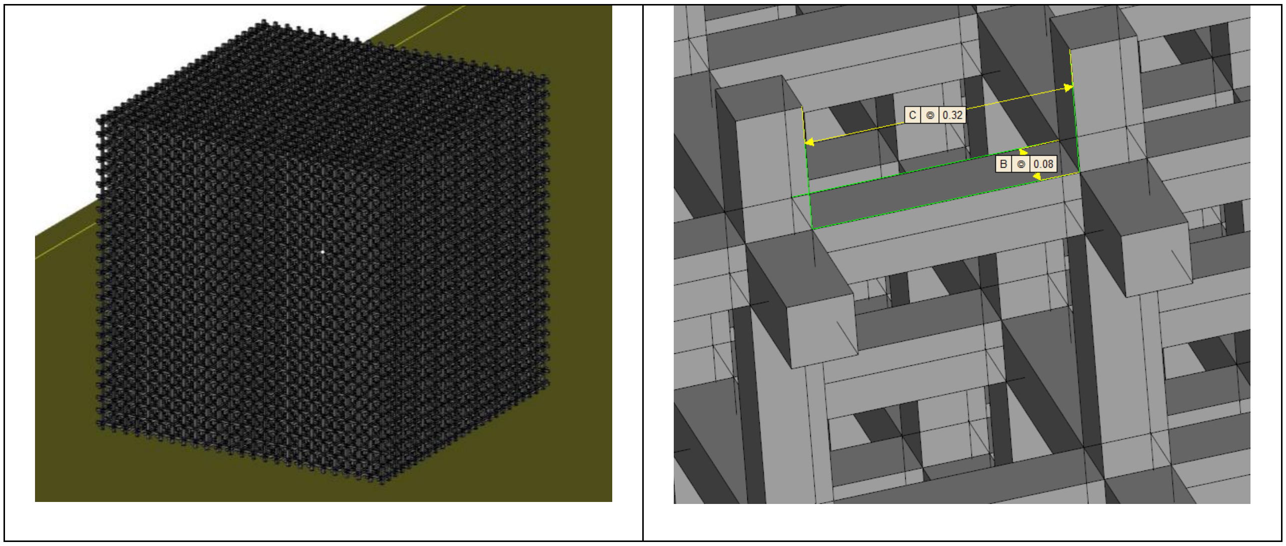

Figure 67: Small cellular lattice design (a) full lattice and (b) dimensioned cell

These samples were only visually inspected to determine produced quality. An image was taken and the outside face was examined for flaws using the Alicona InfiniteFocus microscope. Further examination can be done by utilizing a computed tomography (CT) system for macroscopic flaws within the lattice on more than the outer surfaces.

It should be noted that the powder used was reclaimed and sieved with the internal 80 µm sieve. This is important because it is assumed that powder quality and morphology affects the surface finish, although should not affect buildability [88].

5.3 Results

5.3.1 Simulations

Images of the first pass and the second pass can be seen in Figure 68 and Figure 69 respectively. The first pass simulates a lattice structure where all sides except for the edges are powder. The subsequent passes simulate the rastering found on the first set of experiments where there is an overhanging structure that is "bridging" a gap. This is fundamentally similar but still different than a strut for a thin lattice where only one laser pass defines the strut.

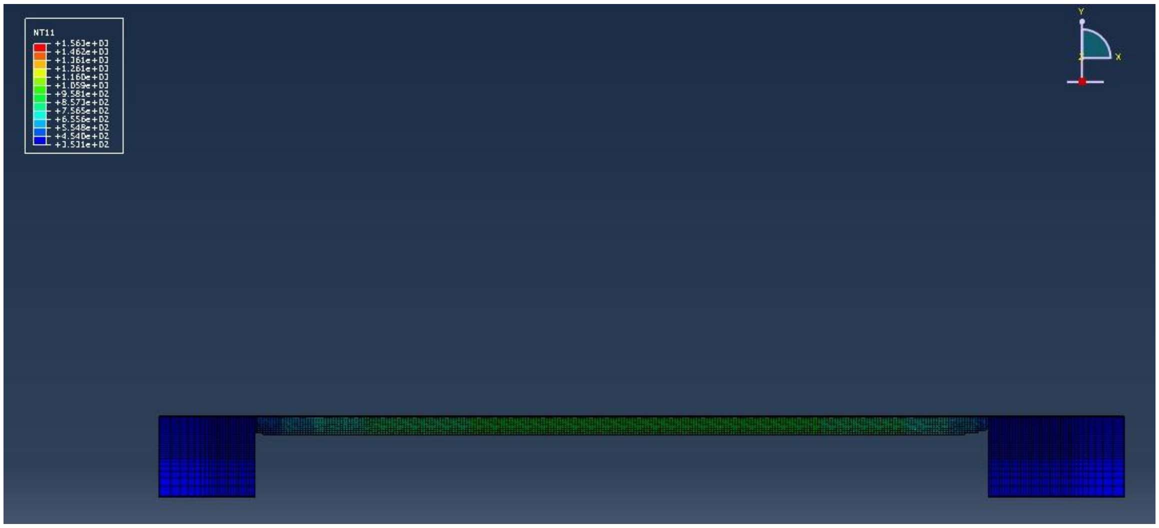

Figure 68: Melt-pool level simulation of first raster pass of overhang geometry type 1

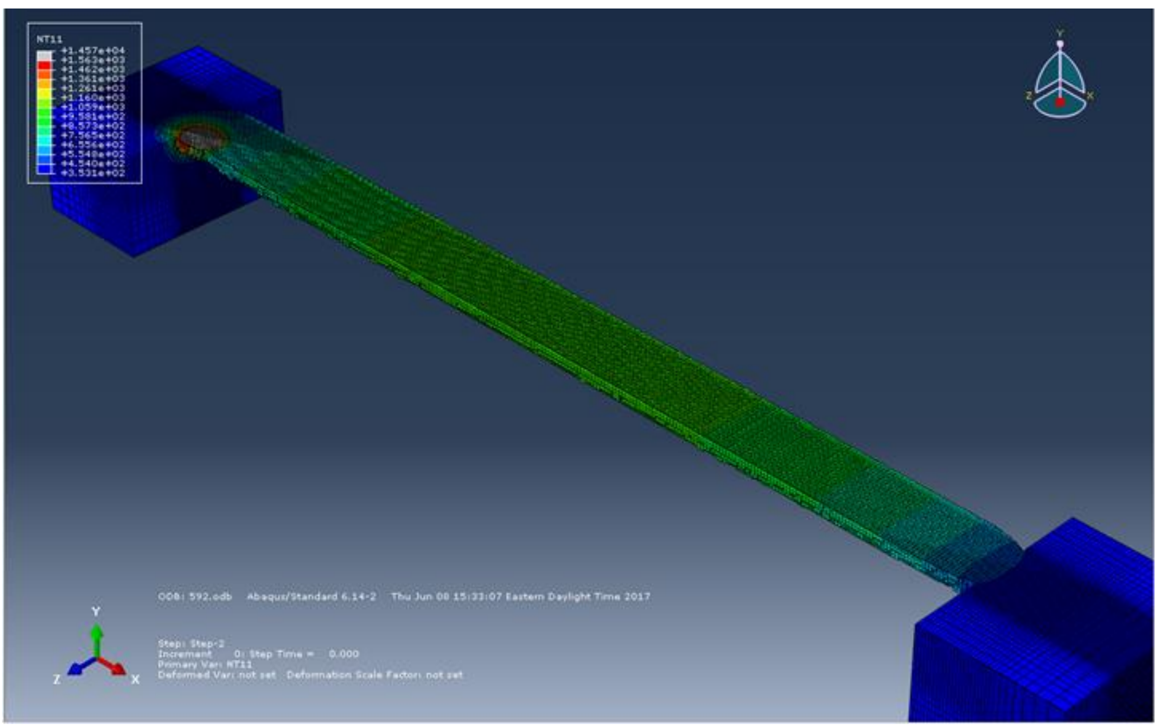

Figure 69: Melt-pool level simulation of second raster pass of overhang geometry type 1

The melt-pool area increases slightly as more raster passes are added, this is due to a combination of residual preheating of the material and the insulation/limited conduction path provided by the powder. Due to rastering, after 2 passes, the middle of the deposited overhang material is at a temperature of 728 °C which is significantly above the nominal preheat of 80 °C. During the building process this increase in temperature is visible as the part starts to radiate in the visible spectrum. These simulations show that there is a very short region where the melt-pool has to transition from melting one amount of material that was solid to an all powder case, resulting in a transitional region where thermal dross, or dross that results solely from a difference in thermal conditions, can be observed. An illustration of this effect is shown in Figure 70. The length of this region is on the order of 150 μm for this power and velocity combination.

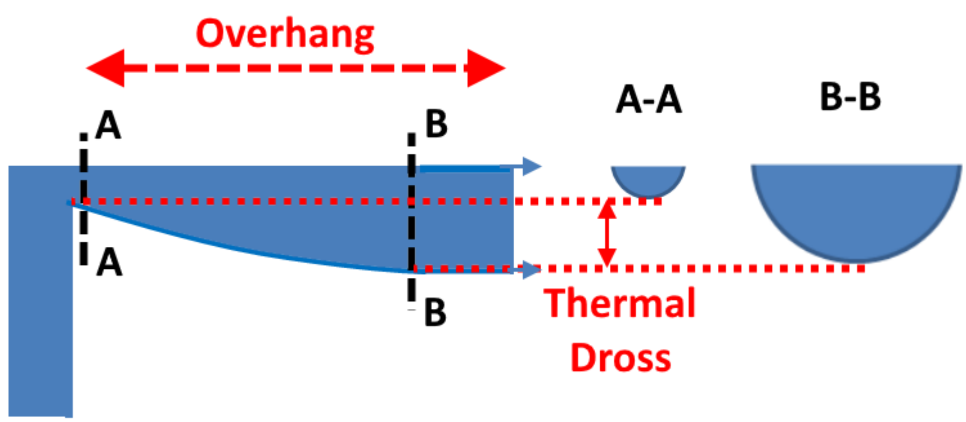

Figure 70: Illustration of thermal dross

The melt-pool increases in size when leaving the solid section and moving to the powder region, this is the thermal dross due to the drastic differences in thermal conductivity (Figure 71). The initial area is approximately 6.15E-8 m² but over a short distance of 150 μm the area increases to 6.6E-8 m² (7% increase in area is shown in the dross in this case). The small increase is due to the start position of the scan path being right next to the powder portion, which will increase initial area further due to insulation. The no powder added weld pool will actually be significantly smaller. The distance that the dross transition should take place over should be dependent on initial and final areas of the melt-pool (the melted area produced within the bulk, to the melted area produced on the powder), so implementing a controller could potentially account for this deviation and result in a sharper corner than is currently produced.

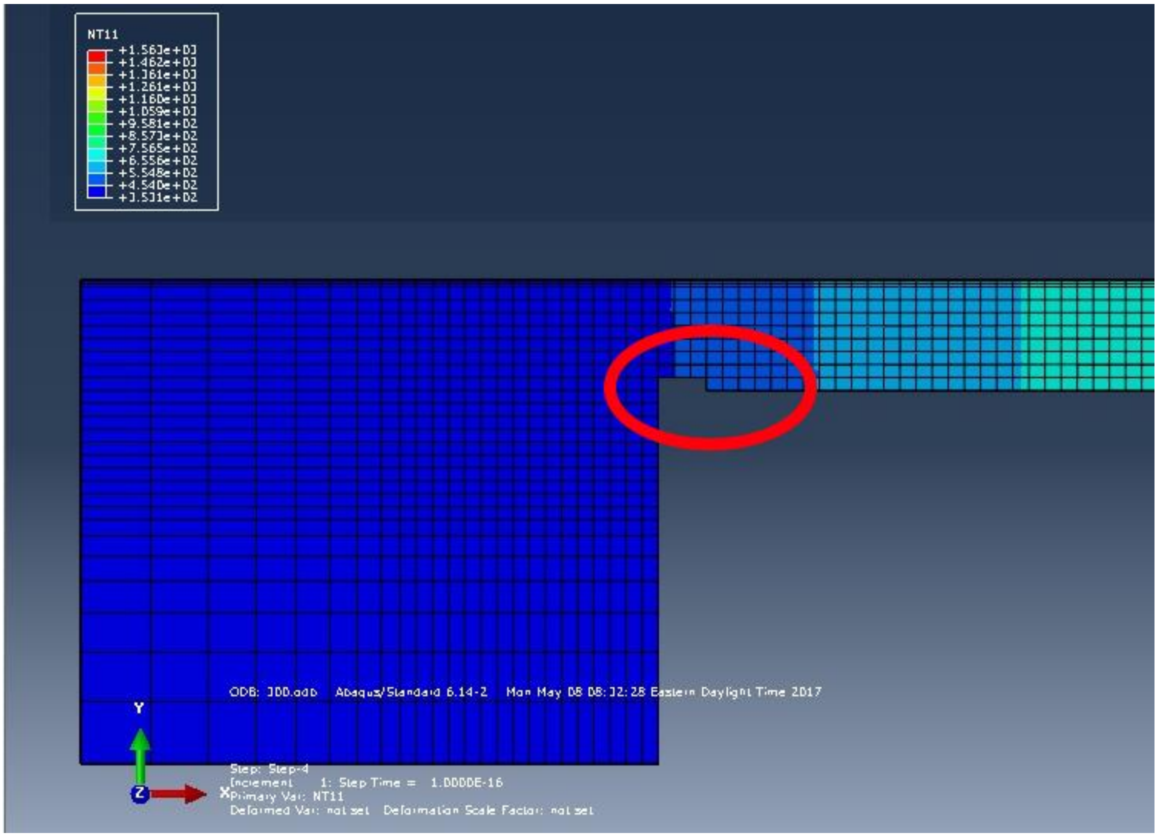

Figure 71: Simulation of thermal dross

The second simulation type gave more insights into how the temperature increases throughout the building of the part and what post solidification peak temperatures can be expected. As the raster passes progress the temperature increases. The residual preheating from previous raster passes elevates the temperature for the first few raster passes. After the first few raster passes the temperature stops increasing due to the more favorable conduction conditions and the overall maximum temperature asymptotically approaches an elevated temperature as the overhang is produced. This is much hotter than nominal conditions would permit, so further research should be done to investigate the use of process control to reduce this preheating effect if melt-pool geometry is of concern.

This finding is evident during production by the presence of optically radiating samples. Physically this phenomena makes sense because as the overhanging structure is produced the heat paths made available to the part increase and therefore thermally the material can dissipate the heat better (so preheat will not continue to increase with increasing width of overhang in the raster direction. Initially the overhang has only the two sides of the overhang to be able to dissipate heat to, since it is surrounded completely with powder. As the fully solid material amount increases this insulation effect will reduce. This phenomena will be greatly affected by the hatch spacing, lasing power, and velocities used. The effects for 20 W of absorbed power and 200 mm/s scan velocity can be seen compared to 20 W, 400 mm/s and 80 W, 1400 mm/s for a 300 μs skywriting delay in Figure 72. With a short skywriting delay there is still a molten portion remaining after skywriting, for the 200 mm/s case, so the preheat is actually greater than melting temperature, and where the heat source is being applied is extremely elevated in temperature. The temperature decays to 1645 K but maintains this temperature. Examining the cases of 20 W 400 mm/s and 80 W 1200 mm/s (Figure 72b and Figure 72c) the system approaches approximately 650 K for both cases, since they are of similar solidification times. These elevated preheats are still significant and can work to reduce the residual stress in the part (by reducing thermal gradients) but also will influence dross formation due to producing more molten material than expected.

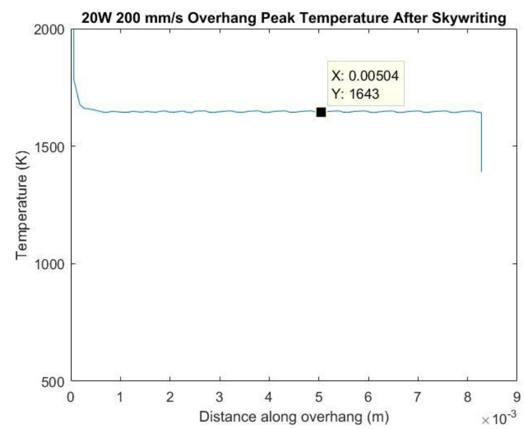

(a)

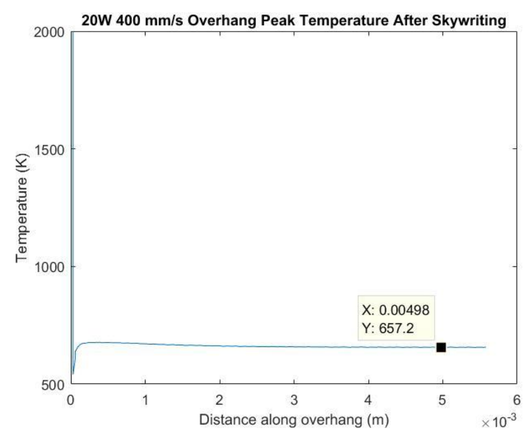

(b)

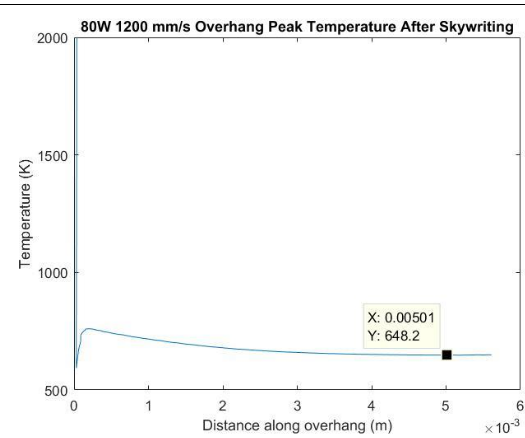

(c)

Figure 72: Peak temperature after skywriting for (a) 20 W, 200 mm/s, (b) 20 W, 400 mm/s, and (c) 80 W, 1200 mm/s

5.3.2 First Overhanging Experiments

As mentioned previously the first iteration of the first overhanging geometry experiments failed, however the knowledge that the Y direction of the raster consistently failed in all but the lowest of power cases was gathered. The X direction rastered parts built consistently for all P-V combinations, with some failing after a number of layers but not immediately. This failure in the Y raster direction agreed well with the assumption that there was an increase in residual stress warping with this raster direction compared to the X direction because a fixed-free beam is being created rather than a fixed-fixed beam.

The second iteration of this experiment gave many more insights into dross formation and buildability of overhanging structures due to the reduction in test parameters that failed catastrophically previously.

Residual stresses during the building process resulted in a number of deformed geometries. Often it was seen with a curvature towards the edge of the overhanging feature where it was not constrained. There were other points where the structure failed because of warping and the sample was then re-lased on the next layer and this bridged the gap, an example of this can be seen in Figure 73. This still allowed the feature to be built, but drastically affected the surface finish. In general for a given parameter combination the down-skin surface was consistently worse than the up-skin surface. The drastic difference in thermal boundary conditions, agglomeration of powder particles to the molten surface, and the inherent directional melt-pool geometry drives the downward facing surface to be significantly rougher than the upward or side facing surface and this can be readily seen with the naked eye.

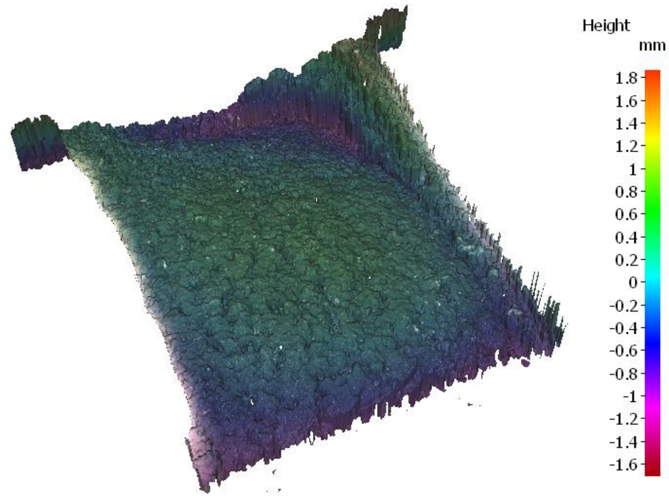

Figure 73: Failed overhang surface

Low power low velocity parameters built consistently regardless of raster orientation. This is potentially because of a reduction in residual stresses (IN625 relaxes residual stress with increased dwell time at temperature) or because of the lower melt-pool length, resulting in less molten material at a given time and thus less ability to form dross. It is assumed that the results that are being seen are actually a combination of both of these factors, however, the length and thus solidification time is assumed to be dominant in the reduction of dross.

Since this was a first iteration of the experiment many of the samples cracked, and thus the data are more qualitative in general for most of the samples. The surface profiles were created to help quantify the dross produced, along the center profile, and the profile from front to back of the sample. These should give insight into the curvature of the samples as well as the dross. There is, in general, a lot of curvature seen throughout all the samples. Flatness was taken as a measurement of the maximum difference between the heights along the profile of the centerline. Ideally the difference would be zero since a flat plane is attempting to be deposited. To quantify the flatness further, since the shape is extremely distorted, flatness is plotted vs the percentage away from the edge the measurement is taken. An example of the profile and flatness measurements can be seen in Figure 74. The overall flatness in the middle and the flatness 20% from the edges are noted in Table 8 along with the overall flatness standard deviation. The profile from front to back of the sample along the center is also noted in Table 8. Due to the extreme amounts of curvature and the variability in this measurement (due to rounding of the edge) this is only taken as the peak flatness value.

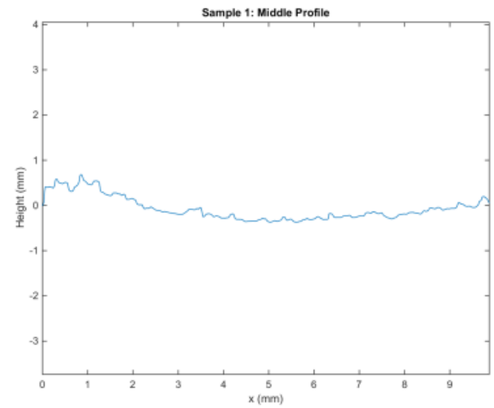

(a)

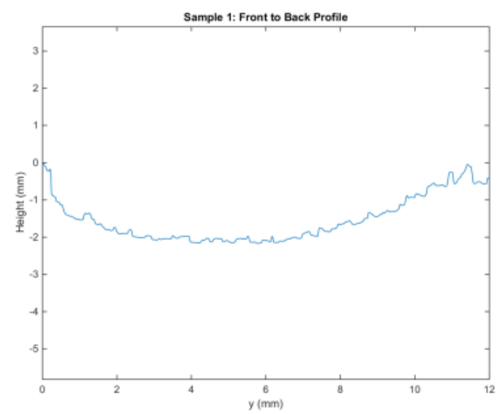

(b)

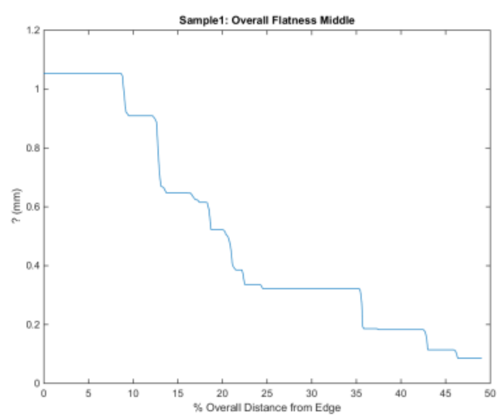

(c)

Figure 74: Example of measurements taken from overhang geometry type 1: (a) Profile along the middle, (b) front to back profile, and (c) flatness of the middle profile

Table 8: Overhang geometry type 1 parameters and measurement values

Sample	Power (W)	Velocity (mm/s)	Flatness (Middle) (mm)	Middle Flatness σ (mm)	20% from Edge Flatness (Middle) (mm)	Flatness (Front to Back) (mm)	Raster Direction	Defects
1	50	200	1.053	0.259	0.523	2.169	x	Curl
2	50	200	1.101	0.277	0.415	2.598	y	Curl
13	50	400	0.686	0.178	0.312	2.504	x	Curl
14	50	400	0.736	0.184	0.314	2.211	y	Curl
15	50	600	1.266	0.316	0.482	2.446	x	Curl/spreading issue
16	50	600	1.181	0.314	0.615	2.626	y	Curl
25	50	800	0.911	0.258	0.776	2.309	x	Curl
26	50	800	0.490	0.102	0.272	2.337	y	Curl
27	100	200	0.868	0.204	0.297	2.169	x	Cracking
28	100	200	NaN	NaN	NaN	NaN	y	Failed
3	100	400	0.860	0.202	0.244	2.561	x	Curl
4	100	400	NaN	NaN	NaN	NaN	y	Failed
17	100	600	1.770	0.288	0.475	2.633	x	Curl/spreading issue
18	100	600	NaN	NaN	NaN	NaN	y	Failed
29	100	800	1.144	0.320	0.367	2.543	x	Cracking
30	100	800	1.286	0.277	0.489		y	Cracking/spreading issue
31	100	1000	NaN	NaN	NaN	NaN	x	Failed
32	100	1000	NaN	NaN	NaN	NaN	y	Failed
33	100	1200	1.009	0.231	0.331	2.492	x	Cracking
34	100	1200	NaN	NaN	NaN	NaN	y	Failed
5	150	600	1.058	0.290	0.651	2.028	x	Cracking
6	150	600	NaN	NaN	NaN	NaN	y	Failed
11	150	800	0.743	0.175	0.255	1.200	x	Cracking
12	150	800	NaN	NaN	NaN	NaN	y	Failed
19	150	1000	1.457	0.392	0.711	1.775	x	Cracking
20	150	1000	NaN	NaN	NaN	NaN	y	Failed
23	150	1200	0.847	0.218	0.336	2.145	x	Curl
24	150	1200	NaN	NaN	NaN	NaN	y	Failed
7	195	800	0.727	0.170	0.478	2.507	x	Cracking/spreading Issue
8	195	800	NaN	NaN	NaN	NaN	y	Failed
9	195	1000	0.537	0.109	0.229	1.908	x	Curl
10	195	1000	NaN	NaN	NaN	NaN	y	Failed
21	195	1200	0.910	0.232	0.375	2.560	x	Cracking
22	195	1200	NaN	NaN	NaN	NaN	y	Failed

The higher power cases produce a flatter surface, however appear to be more prone to cracking and other failures. The lower power parameters appear to produce a large amount of dross and are not flat but consistently can be built without other issues. The lower powers could potentially produce a nicer surface if further constrained by supports on the edges. The least amount of dross in the “X” direction is formed at high power high velocity (195 W 1000 mm/s), but the low power results are similar when looking at the low velocity low power results (50 W 400 mm/s). All samples exhibit curl to some degree and this results in an extremely poor front to back profile. The best parameters that did not crack in terms of the front to back profile are at 195 W 1000 mm/s.

A process map of the parameters and the flaws seen when creating the overhanging geometry presented was created and can be seen in Figure 75. Production of overhang geometry 1 is possible, however for any large geometry of this type there is an unavoidable amount of dross formation and curling of the unsupported edges, regardless of process parameters. If buildability is the major concern the user should aim to use the low power and low velocity processing parameters in the bottom left corner of processing space.

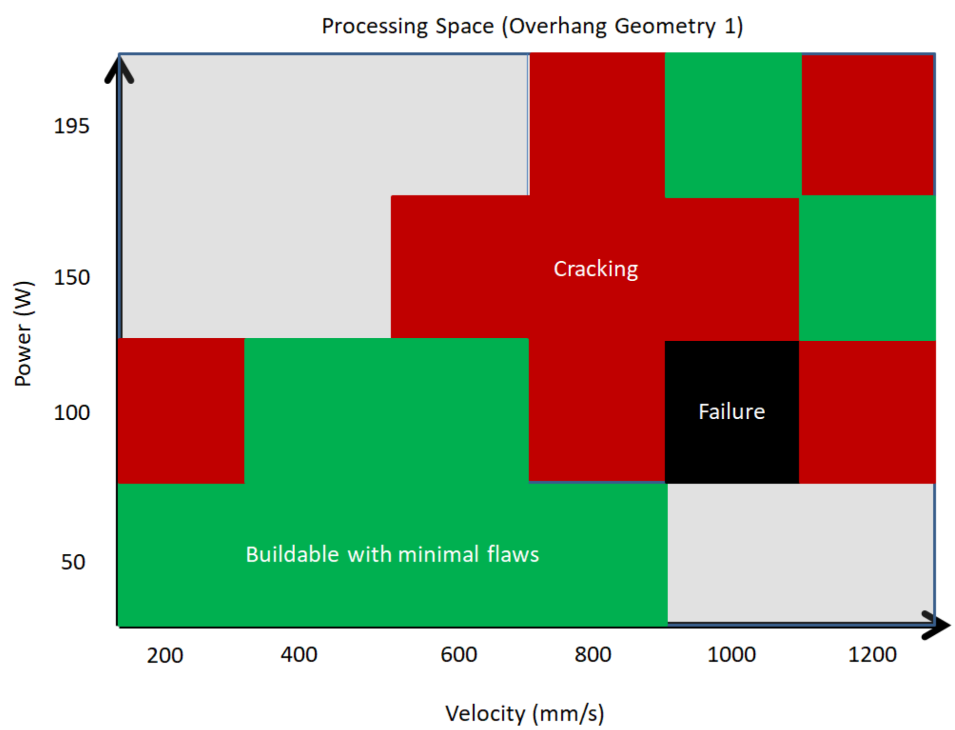

Figure 75: Processing space for overhang geometry type 1 experiments

A basic experiment utilizing a high speed camera (Photron FASTCAM Mini AX200 type 900K-M-16GB) for one of the optimal parameter combinations (50 W 600 mm/s) was done to provide data for future research. An exposure time of 50 μs at 6400 frames per second was used for this imaging experiment and the gamma was decreased in order to better show the contrast between the region of interest and the powder bed. The results can be used in future work to determine the temperature gradient of the overhang during production. An example image from the high speed footage, which actually shows the optically radiating surface, can be seen in Figure 76.

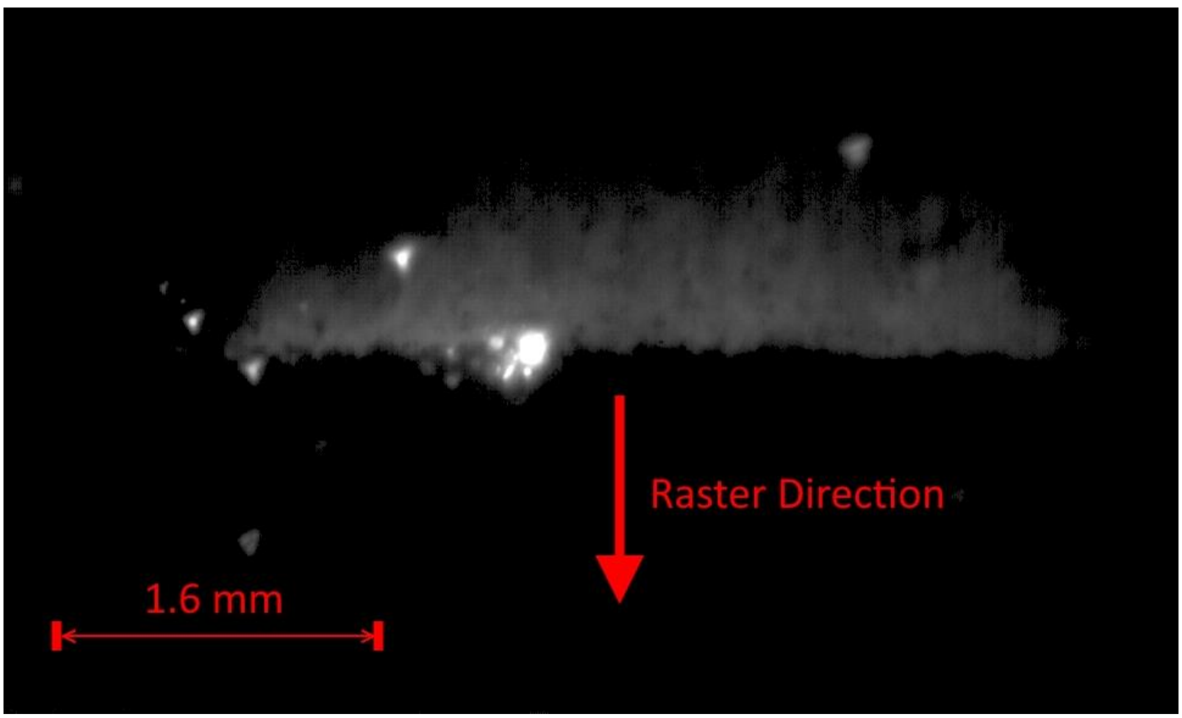

Figure 76: High speed camera image of overhang geometry type 1 production

5.3.3 Second Overhanging Experiments

The results of the second overhanging experiments varying power and velocity yield results similar to what was seen in the first set of experiments. These results are less deformed when successfully constructed when compared to the first set of experiments, which is understandable given the more constrained geometry. Low power and low velocity parameters, as predicted, built without issue again.

Many overhangs built but had a delamination of the weld or cracks that formed. When these defects occurred, the overhanging geometry oftentimes curled, and successfully built the next layer. This, however, resulted in extremely poor downskin, or downward facing, surfaces as well as not truly successful builds. A dross failure is a failure type that was seen where the melt-pools sagged to a point where they were well below the plane of the building surface and thus a failure mode occurs around the perimeter of the sample. Figure 77 illustrates some examples of the samples that illustrated defects that were visible by the naked eye.

			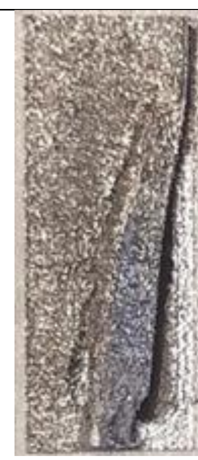
Cracking	Dross Failure	Curling	Delamination

Figure 77: Types of overhang failures seen in overhang geometry type 2

The dross was analyzed across processing space and was again characterized by the max difference between the surface profile. The surface profiles along the centerline of the "X" direction can be seen in Figure 78 for the correctly built samples. The values for the flatness for the correctly built samples, along with the surface finish (Sa) values can be seen in Table 9. Upon inspection the profiles appear to be relatively consistent in shape for the parameters that built correctly. The values, however, for overall flatness, and thus dross, are substantially different, ranging from 0.686 mm to 1.163 mm, with no apparent trend. Potentially the edges of the profile have measurement issues with the microscope being unable to determine focus correctly on the edges because of lighting. The flatness at 20% of from each edge is similar in scale for all the samples with the values being within the surface finish values of one another.

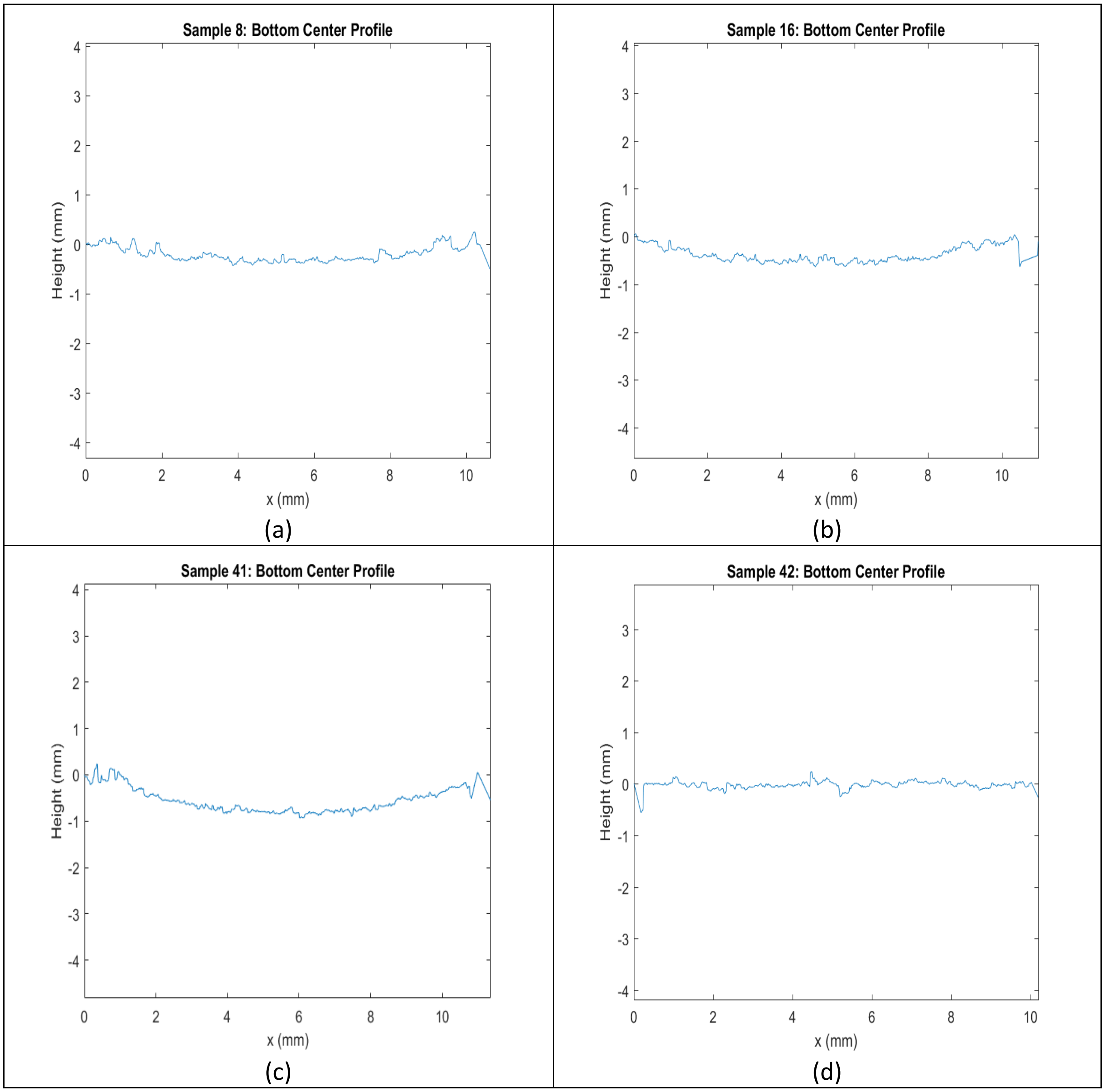

Figure 78: Center profiles of overhang geometry type 2 for (a) 50 W, 200 mm/s, (b) 50 W, 400 mm/s, (c) 50 W, 600 mm/s, and (d) 195 W, 800 mm/s

Table 9: Measured properties of overhang geometry type 2 samples

Power (W)	Velocity (mm/s)	Sa (µm)	Flatness (mm) (Full)	Flatness 20% from the edges (mm)
50	200	41.542	0.7473	0.3395
50	400	34.474	0.686	0.4164
50	600	32.622	1.1636	0.4625
195	800	25.913	0.7922	0.4869

The EDM cutting path structurally weakened the pockets such that some parameters appear to have warped the walls of the pocket horizontally via residual stress. This appears most evident with the high power, medium velocity cases. An outlier to the successful experiments, 195 W, 800 mm/s, caused significant warping (Figure 79) on the order of 1 mm on either side of the experimental jig. The pocket deformed greatly since ideally the pocket would follow the red outlines in Figure 79 however it is evident that it does not. This outlier had the best surface finish of the samples produced in this set of experiments with a ±26 µm surface finish (Sa). It is believed that this surface finish is a result of the extreme residual stresses and that without the deformation of the base material there would be a considerably worse surface finish. Surface finish is not drastically changing for downskin for any of the parameters that successfully built. The range of produced surface finishes is between ±26 µm and ±42 µm. The higher velocity parameters produce a better surface finish, which makes sense since the melt-pools are smaller.

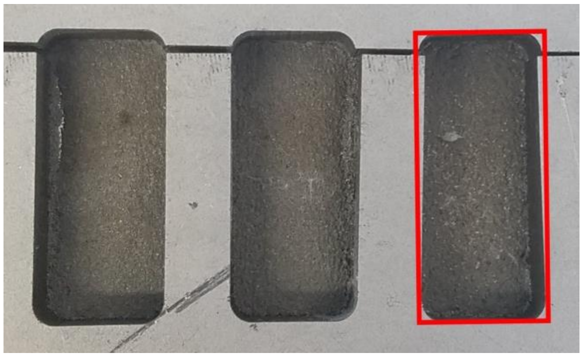

Figure 79: Residual stress warping in overhang geometry type 2 samples

A compilation of the images of the top of the surface can be seen in process space in Figure 80 and the bottom surface in Figure 81. The viable processing parameters are highlighted in green in these two images, resulting in a process window to be used when depositing overhangs of this type. The three types of failure are highlighted in yellow, red, and blue, for lack of fusion, cracking, and dross induced failure, respectively.

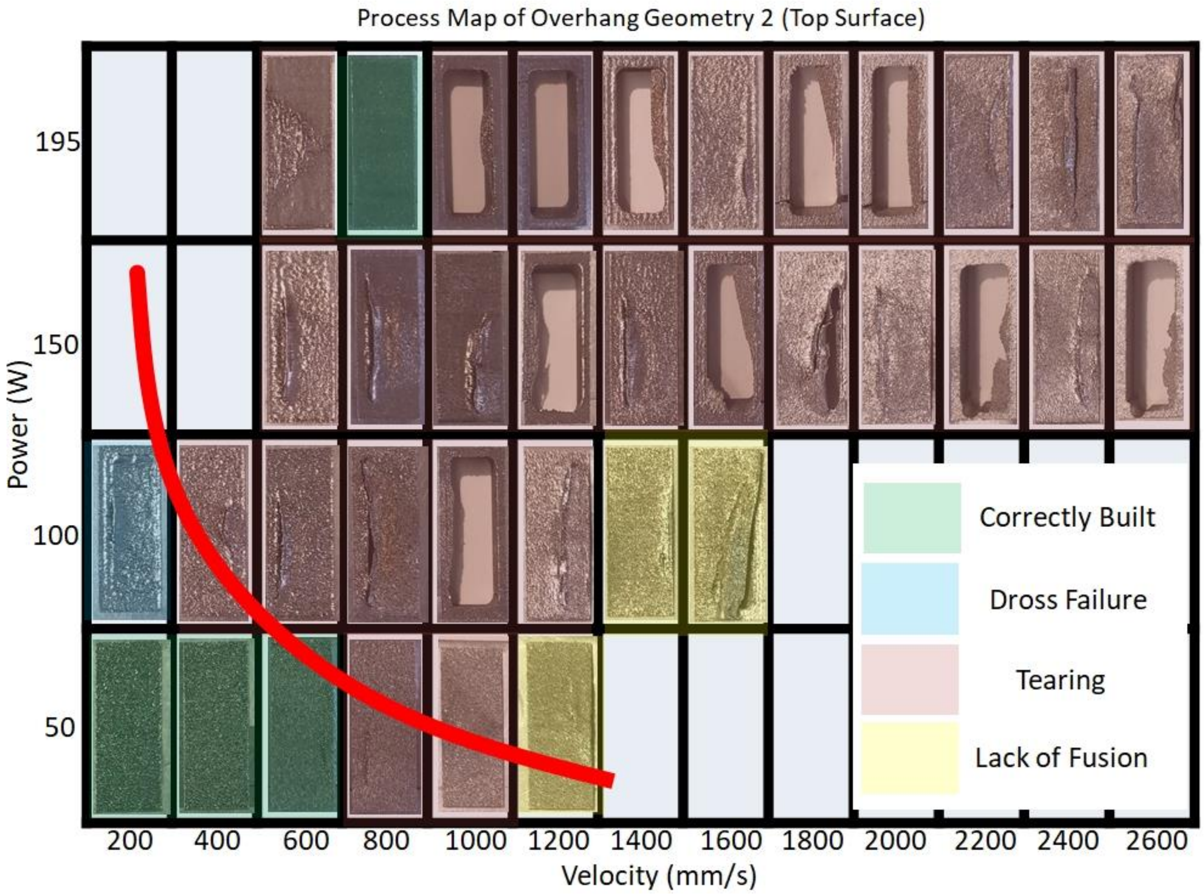

Figure 80: Process map of overhang geometry type 2 for top surface with L/D curve overlaid

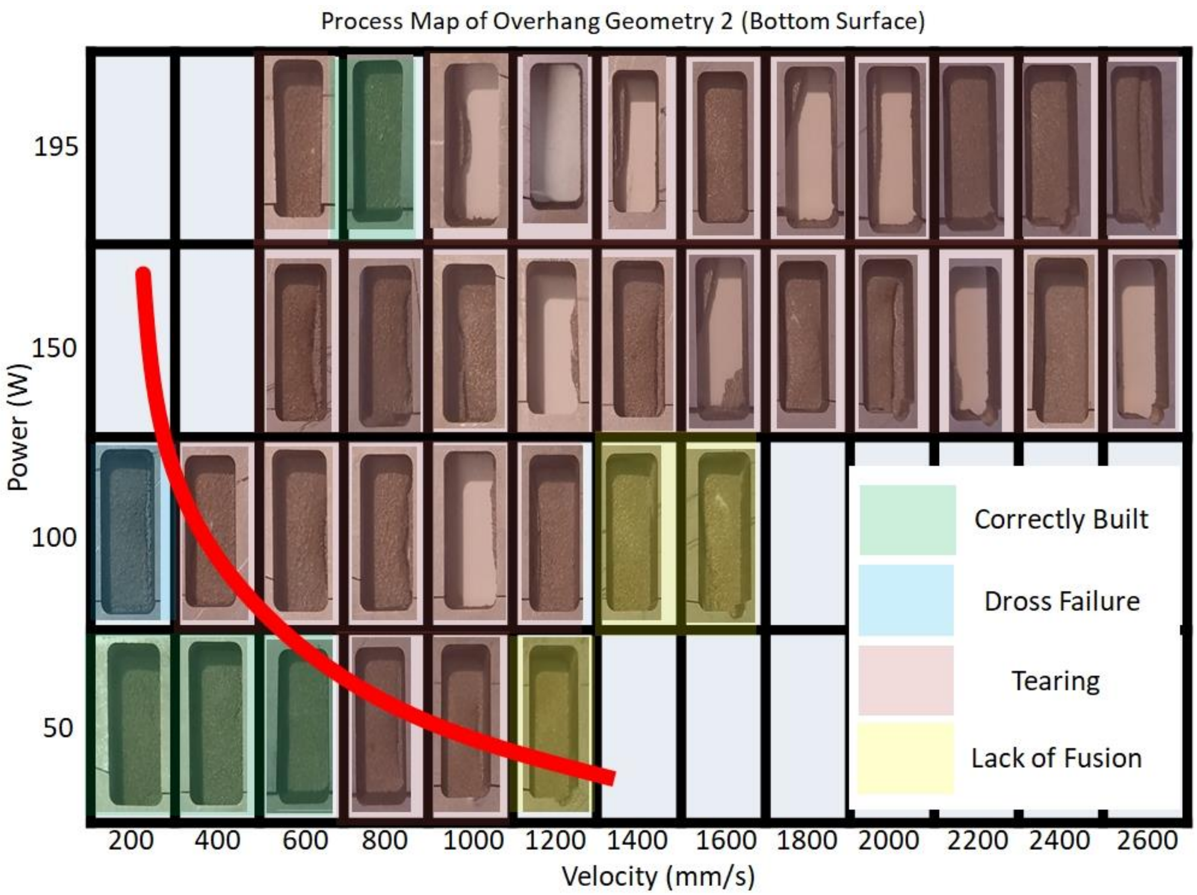

Figure 81: Process map of overhang geometry type 2 for bottom surface with L/D curve overlaid

These experiments and results reinforce the idea that there is an L/D dependence to the failures, as well as a dross induced failure cutoff. An L/D curve would be parabolic in shape, as seen in Chapter 4 (Figure 51), and cut off higher power/low velocity and low power/high velocity cases. A curve of constant L/D has been overlaid in red on the plots in Figure 80 and Figure 81 and fits what is being seen well. From these results it is evident that to successfully deposit a large overhanging pocket a low velocity and low power are required.

5.3.4 Third Overhanging Experiments

The nominal EOS downskin parameters fail almost immediately by delaminating from the surface on layer two. Figure 82 shows the delaminated nominal downskin parameters (outlined in red) after failure. The remaining parameter combinations all successfully built to some degree. The discoloration seen in some of the combinations is indicative of excessive heat buildup within the sample. Upon inspection, the high velocity and low power parameters appear to have had slight delamination problems, so this confirms the previous work that low power and low velocities are where overhanging structures should be deposited.

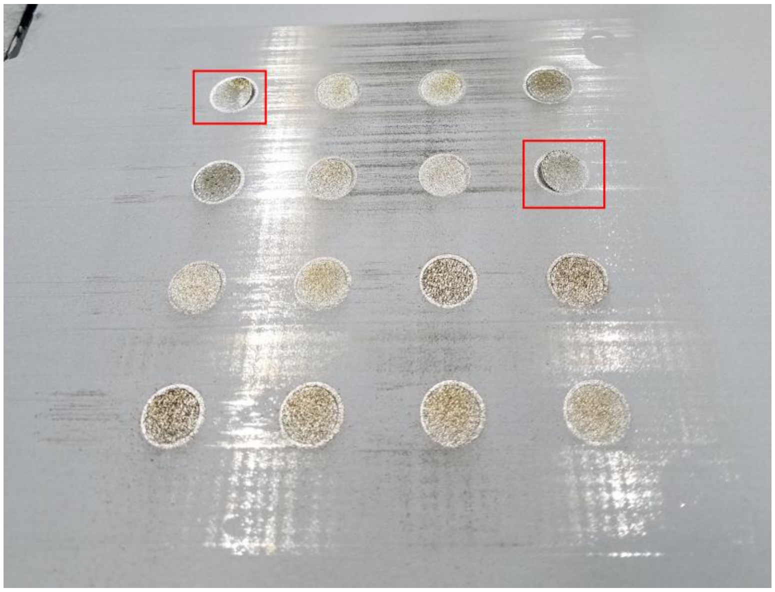

Figure 82: Failure of the nominal downskin parameters

The downward facing surface finish of the samples produced is documented in Table 10. From the Sa measurements it can be seen that higher velocities produced the best surface finish, with a value of 30.925 µm being the best downward facing surface that could be achieved using the parameters tested. This makes sense knowing that the melt-pool size is smallest at higher velocities. That being said, all of the samples appeared to have similar surface roughness values approximately equal to the mean powder diameter, which could be an indication that the powder is agglomerating on the downward facing surface of the overhang and dominating surface roughness. If powder size is dominating the surface roughness this implies that that the processing conditions don’t appear to have any great effect in the regions that were examined.

Table 10: Surface roughness measurements (Sa) of overhang geometry type 3 experiments

Power (W)	Velocity (mm/s)	Sa (µm)
50	200	49.937
50	400	41.169
50	600	38.203
50	800	33.696
50	1000	32.056
50	1200	30.925
195	800	30.925
150	2400	NaN

The profiles of the produced structures were analyzed to determine the dross formation. The dross topology can be seen in Figure 83, where zero is arbitrarily chosen and is the average height value of the surface computed by the Alicona software. From inspection it can be seen that the dross formation is considerably better in this experiment than the previous experiments, due to the fully constrained boundaries. The dross was again measured in terms of the flatness for the deposited surface, this time using four profiles taken across the diameter at 45 degree intervals with the maximum values and the average values of flatness recorded, not just a singular profile. The flatness is documented in Table 11. The nominal parameter profiles had the greatest flatness at 328 µm, although since this has other issues during production, the best profile that did not have production issues was the 50W 600 mm/s profiles, with a flatness of 422 µm. The high velocity profiles started to curl and this caused a large deviation for the flatness term. The flatness in general will increase with an increase in velocity until there is a building issue.

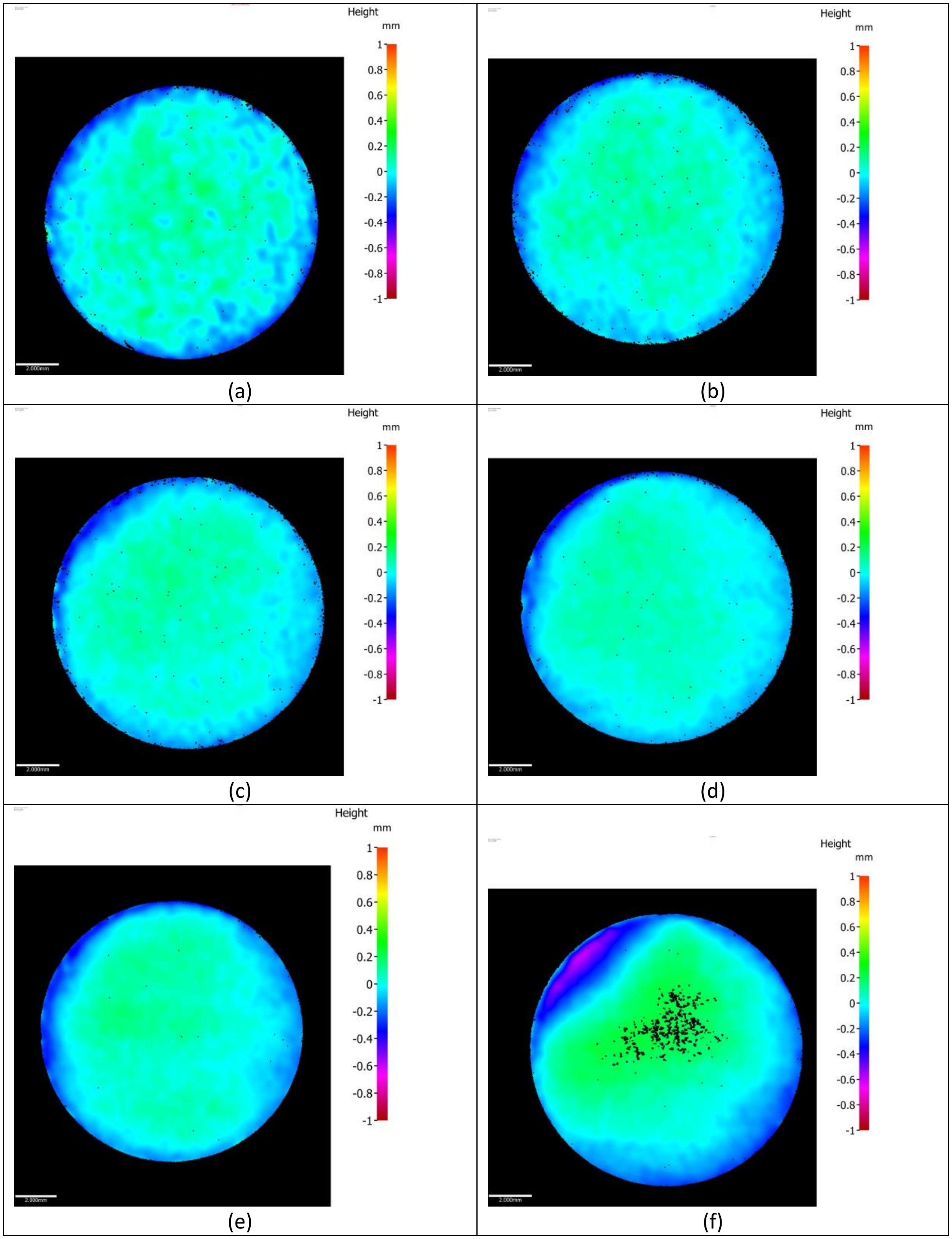
Height
mm
1
0.8
0.6
0.4
0.2
0
-0.2
-0.4
-0.6
-0.8
-1
(a)
(b)
(c)
(d)
(e)
(f)

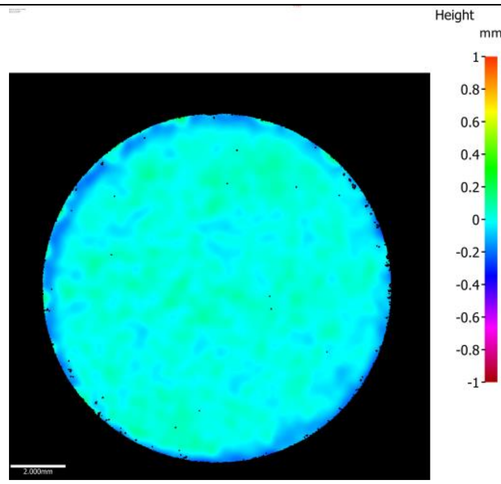

(g)

Figure 83: Bottom profiles of overhang geometry type 3 (a) 50 W, 200 mm/s, (b) 50 W, 400 mm/s, (c) 50 W, 600 mm/s, (d) 50 W, 800 mm/s, (e) 50 W, 1000 mm/s, (f) 50 W, 1200 mm/s, (g) 195 W, 800 mm/s

Table 11: Flatness values of overhang geometry type 3

Power (W)	Velocity (mm/s)	Average Flatness (µm)	Max Flatness (µm)
50	200	399.76	496.52
50	400	358.15	423.33
50	600	350.81	422.37
50	800	387.28	522.27
50	1000	412.14	449.18
50	1200	616.99	874.4
195	800	251.55	328.79
150	2400	NaN	NaN

These images illustrate the surface texture of the dross but are not directly indicative of the overall protrusion from the plane that would be the ideal top of the baseplate. This value would ideally be minimized to produce the closest to net shape geometry as possible, which means that ideally the melt-pool would be very small. To find the overall protrusion from the base of the plate the dross profile is subtracted from the thickness of the plate. From this calculation it becomes evident that 50 W 1200 mm/s produces the least amount of protrusion at 110 µm of overmelting, which aligns with previous work that higher velocity will result in a smaller melt-pool, although this protrusion is much greater than the amount one would expect from such low power parameters. This parameter combination does not successfully build, however, so the least amount of overmelting protrusion can be achieved while successfully depositing by using the 50 W 600 mm/s parameters to produce a 210 µm of overmelting. The nominal bulk part parameter, 195 W 800 mm/s appears to have a very sporadic surface texture, although is fairly flat. This is likely due to intermittent keyholing as well as the bead-up effects that are occurring within this combination. These parameters produce what appears to be a low amount of overall dross, however when the thickness of the plate is considered there is a substantial amount of penetration, measured at 410 µm. These parameters also substantially superelevate from the surface, which during production can cause failures or flaws.

After all of the previous experiments were concluded and the 50 W cases consistently appeared to build better with less dross, it was further investigated as to why. The initial thought, before experimentation, was that the solidification time would want to be minimized to reduce the amount of dross formation because a faster solidification would allow less time for movement of the melt-pool. This assumption appears to apply for these low power cases since the solidification time (Equation 8),

Equation 8: Solidification Time

$$S_t = \frac{L}{V}$$

Where S_t is the solidification time, L is melt-pool length, and V is the scan velocity, thus, from simple kinematics, the distance the melt-pool can travel downwards before fully solidifying, assuming the powder offers no resistance, and neglecting capillary effects (Equation 9):

Equation 9: Kinematic dross equation

$$x_{kinematic} = \frac{1}{2} g \left(\frac{L}{V}\right)^2.$$

Wicking into porous media can be represented by Equation 10 [121].

Equation 10: Wicking into porous media

$$x_{wicking} = \frac{S}{\varepsilon}\sqrt{t}$$

Where ε is void fraction, S is sorptivity, $x_{wicking}$ is distance travelled, and t is time.

Wicking into a porous media is more of a surface finish problem than a dross effect, since most powder that the molten pool will wick into will just melt that powder particle. That being said, wicking should still be noted as a possible source of errors as it will allow powder particles to agglomerate onto the surface of the melt-pool. The wicking will also become a dominant factor in surface finish since a partially melted or adhered powder particle would increase surface roughness over a continuous melt-pool.

From the kinematics it becomes apparent that at the same velocity for an increase in power from 50 W to 195 W the dross formation is almost two orders of magnitude larger purely from the gravitational kinematics. Including the wicking phenomena will only exacerbate the dross formation, as it is also a time dependent function.

From these equations one would conclude that it would be possible to increase the build speed and power and result in a similar solidification time. This may be possible with a drastic increase in speed, which may make the melt-pool too small to be useable in some cases. However, the increase in melt-pool length results in a much higher length to depth ratio. This higher L/D ratio will trip into a bead-up regime where the bead is no longer being deposited as a single continuous weld due to surface tension effects. An example of a part deposited on pure powder with parameters that would normally be well outside the bead-up regime (100W at 400 mm/s) can be seen in Figure 84. The severe porosity in this deposition strategy results in extremely fragile surfaces during deposition. Creative lasing strategies could mitigate some of the porosity, however if the part fails during deposition these parameters are not suitable. This results in an extremely narrow usable processing window where the melt-pools are deep enough to be useful, solidify fast enough to not dross from kinematics, have a low enough residual stress, and are continuous welds. An experimentally derived process map for the usable regions for producing large overhangs can be seen in Figure 85.

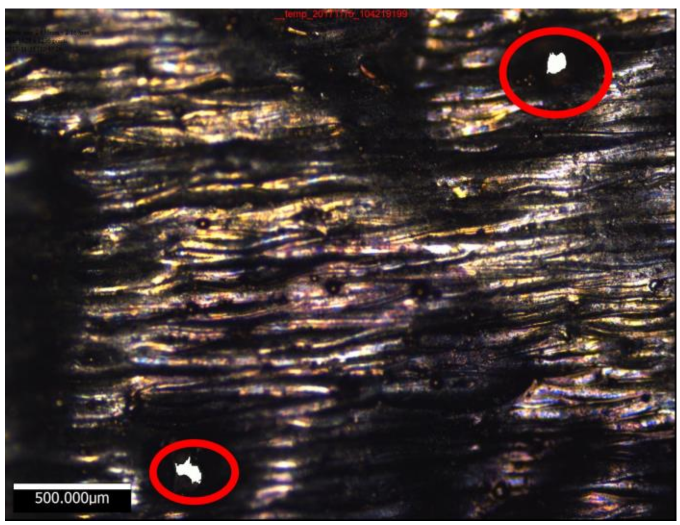

Figure 84: Bead-up induced porosity in overhang geometry

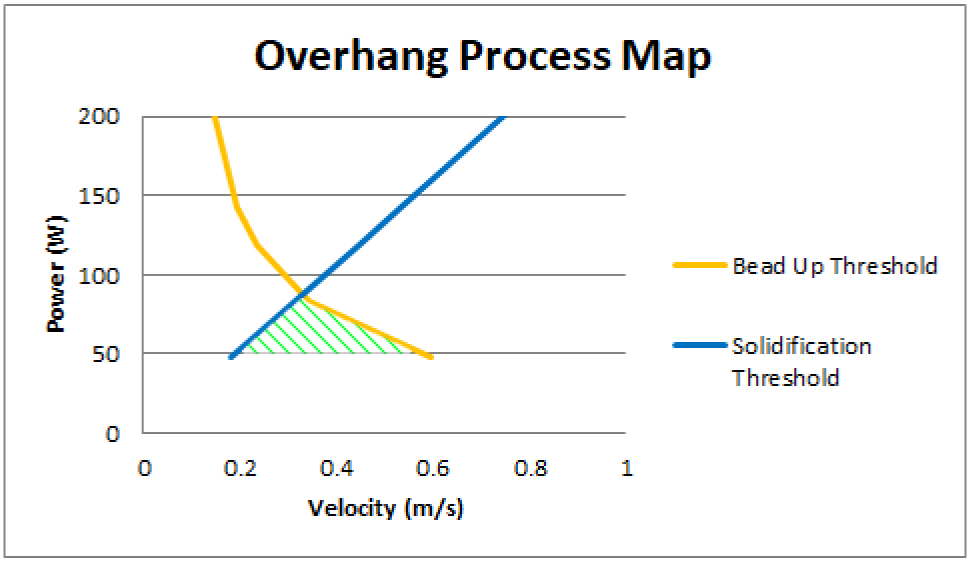

Figure 85: Overhang process map

5.3.5 Application to Cellular Lattices

The results of all of the previous work, when applied to large span cellular lattices, result in a well formed lattice compared to what is currently produced. The nominal hatch parameters produce a well formed lattice, but with a significant amount of dross formation and curvature to the struts. The residual stresses cause the nominal parameters to be virtually unbuildable without a flexible recoater blade, since the rigid recoater will either tear the entire lattice free or destroy the offending struts. The lower power custom parameters did not appear to protrude from the powder bed to as great an extent as the nominal parameters. An image taken in-situ after recoating can be seen in Figure 86 where it is evident that there is a significant amount of protrusion for the nominal parameters (outlined in red) but not for the custom parameters (outlined in green). This will allow these parameters to be potentially used with a rigid recoater blade and thus within large bulk geometries where the flexible recoater is not a feasible option, or surface finish and repeatability is of a high priority.

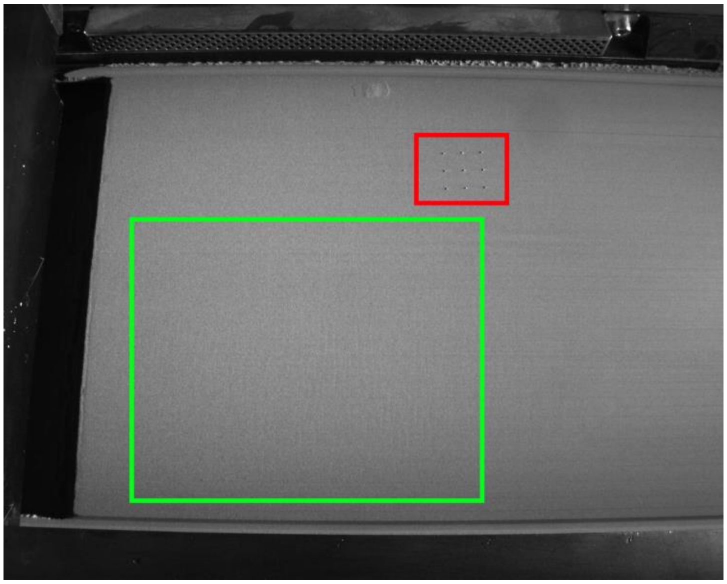

Figure 86: Cellular lattices being produced with custom parameters (green outline) and nominal parameters (red outline)

The large cellular lattices can be seen in Figure 87 and the deviation from a flat profile is readily noticeable. The nominal parameters have failures in the center of the struts, while the newly proposed parameters successfully produce the desired shape. The amount of dross is significantly less and on the order of 300 μm when comparing these two produced structures.

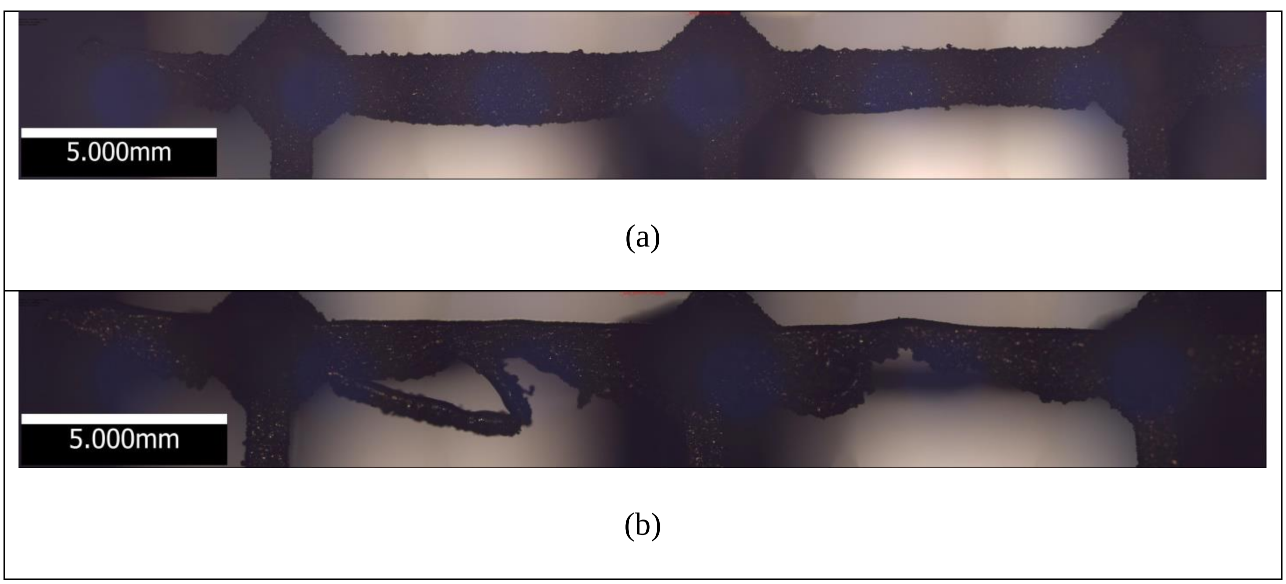

Figure 87: Large lattice structures (a) 50 W 600 mm/s and (b) 195 W 800 mm/s (nominal)

When applied to a small scale lattice, just to test feasibility of the same parameters for both small and large lattice structures, the results are promising. From basic optical imaging it appears that the majority of the lattice structure built without flaws (Figure 88). The trusses are larger than designed but this is unavoidable without adjusting the beam focus since 80 µm is near the limits of what is able to be produced.

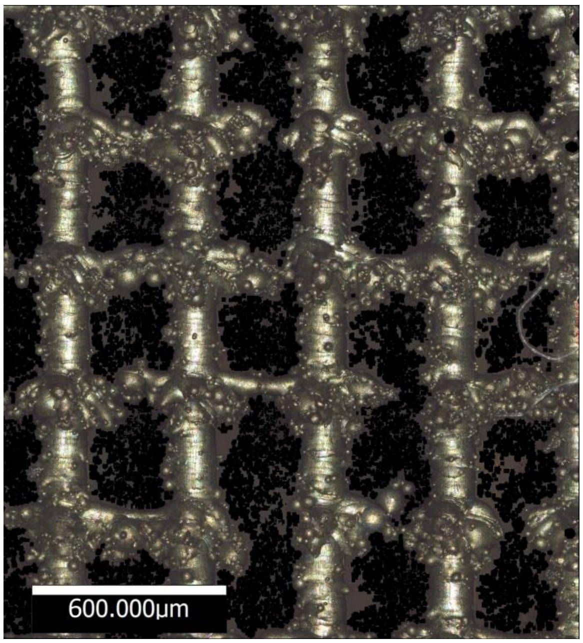

Figure 88: Small scale lattice produced at 50 W 1000 mm/s

The smaller lattice, due to the small single bead struts, can use smaller weld beads than would be used when producing an overhanging structure. So the process map for small lattices would ideally expand slightly in velocities, however, not extremely far since delamination and bead-up are still of concern and this is likely why many of the struts failed in the produced sample, using a lower velocity would likely get rid of these deposition errors. The lattices should use a similar process map to that of the overhangs, concentrating on the low power low velocity regions.

5.3.6 Conclusions

A series of overhanging geometries were constructed using no support structures in order to determine buildability and resulting surface finish using various processing parameters. This methodology illustrated the differences between various geometries and their effects on dross, buildability, and surface finish.

Low power low velocity points appear to be consistently buildable for a variety of unsupported overhanging geometries. The points don't have excellent surface finish, however, and would need post processing in most applications, such as wave guides in order to reach the required surface finish. The points are thought to reduce dross because of the lower length and faster solidification time. A higher power results in a longer length, which, given a higher velocity, allows for the same solidification time. The issue with longer lengths, however, is that bead up phenomena will begin to occur, as well as the melt-pool sizes become smaller when you hit the requisite velocities. Production of overhanging structures of the types 2 and 3 are more reliable than the production of an overhang of type 1 without supports. Adding supports at the edges of such a geometry would increase build quality substantially. Types 2 and 3 can be produced with a low amount of dross if parameters are kept in the low power and low velocity regime.

For the bulk of the overhanging structure it appears that many of the defects are caused by residual stresses interacting with high porosity in the part and not by thermal dross. The dross has a more dominant and visible effect for single bead and thin walled struts deposited on powder such as what is utilized within cellular lattice structures. The dross still does occur, and could be accounted for using a feedforward control system knowing the conductivity differences in the powder and bulk material similar to the work done by Fox [31] since it was shown in that work that the response distance is a function of the initial and final cross-sectional area.

Large cellular lattices were constructed and proven to be buildable at the parameters that were derived from experimentation. When compared to the nominal production method used by the EOS the custom parameters appear to result in a better horizontal surface with less dross formation and strut breakage. With small lattice structures there appears to be uniform overmelting occurring, although a number of the lattice struts appear to have been destroyed by the recoating process and bead-up during deposition, this is a result of too high of velocity for these conditions.

Chapter 6 Conclusions and Future Work

6.1 Conclusions

As additive manufacturing, particularly laser powder bed AM, becomes more desirable in modern manufacturing, new alloys will need to be characterized quickly to use the equipment to its full potential. Work in this thesis focused on the rapid development of process parameters for new alloy systems in terms of melt-pool geometry by manipulation of three processing parameters: (1) laser power, (2) scan velocity, and (3) powder layer thickness. In order to quickly develop parameters for a new alloy system, a process mapping approach and methodology is proposed and utilized to quickly quantify desired melt-pool geometries for Inconel 625. This methodology can be applied to any alloy system and provide low cost experimentation and simulation tools to develop new parameters for new alloy systems in the DMLS process.

The proposed process mapping methodology is further streamlined to develop process parameters for 17-4 stainless steel. This further reduces experimentation cost and time by successfully removing steps in the process. Comparisons were drawn between the two alloys under investigation to draw insights into how different alloys behave throughout process space. During investigation of these alloy systems absorptivity with cross-sectional area dependence was investigated and determined to fit the data much better than a constant absorptivity throughout processing space. This work also translates work from the EOS M270 at NIST to the M290 at CMU, showing that work can be translated between equipment.

Powder in the processes has long been of concern in the laser powder bed process. The thermal effect of powder for two different alloy systems was investigated and it was found that powder can be neglected for much of processing space when dealing with relatively thin layers compared to the predicted melt-pool geometry. Production of metal powders for new alloy systems can be costly and time consuming; the ability to predict melt-pool geometry with only bulk material is highly beneficial to determine the build rates and melt-pool geometries that can be produced with a given alloy. The results of this research form the basis of a powderless approach to development of new alloy compositions for additive manufacturing.

The difficulty in producing overhanging geometries without support or with minimal support is a major issue with the L-PBF process. Manipulation of process parameters was done to determine the optimal regions of processing space to produce unsupported overhanging structures with minimal defects. The low power and low velocity parameters consistently build with the higher velocity of these parameters giving the best overall properties in terms of dross and surface finish. Finally, these results were applied, with great success, to two different sizes of cellular lattices to determine their applications to other overhanging geometries. All of the information presented in this thesis can lead to faster development of process parameters for new alloy systems in the powder bed fusion process and to build more intricate geometries that are otherwise impossible or difficult to produce.

6.2 Implications

While previous work has been done to process map various alloys, little work has been done to expand and develop this technique in relation to the laser powder bed fusion process by establishing a consistent methodology for process parameter development of new alloys, even without access to powder. Little work has also been done on identifying processing parameters to produce large overhangs beyond the build angle limits with standard parameters. This work has provided major insights into the following aspects of manufacturing using L-PBF:

- Process maps, experimentally and computationally, for both IN625 and 17-4 geometry are thoroughly documented for the L-PBF process. This work enables engineers and machine users to optimize parameters for the desired properties for their part. This can allow for faster build rates or better surface finish and feature resolution.
- A process development technique for new alloys is proposed, implemented, and streamlined. Machine users can utilize this streamlined approach to rapidly develop process parameters for new alloys for use in the laser powder bed process at reduced cost. Small quantities of powder and experiments can be used to fully determine the viable process regions for a given alloy system. This technique is now a commonly used tool within the Beuth lab group at CMU.
- The effect of powder layer thickness is analyzed. It was found that for thin layers of powder there is little effect on melt-pool geometry. Implications of this are widespread as procurement of powder of a given alloy of interest can be difficult and costly, while often plate or bar stock of this material can be readily acquired or produced. No-added powder experiments can be done and the process space can be mapped for many flaws before powder is even considered. This can rapidly develop a new alloy and determine its viability as a material for the process. These results are a driving force behind new powderless alloy development projects at CMU.
- Absorptivity was found to vary with cross-sectional area. This will allow process engineers to better correlate simulations to experimental results and equipment. Since machine time is more expensive than computational time there are numerous benefits to better correlating simulations to a minimal number of experiments.

- A series of process parameters have been evaluated and suggested to be able to produce unsupported overhanging structures with minimal flaws. End users can apply this knowledge to make more complex and intricate geometries, such as the cellular lattices shown previously. The ability to make these geometries internally without support can help redesign how things such as waveguides and filters are produced.
- Work was translated directly from one piece of equipment to another. With machine costs being high and time valuable, engineers need not develop all parameters on a single machine. Developing on a similar piece of equipment (EOS M270 and M290 in this case) can reduce downtime and directly translate to a scaled up manufacturing facility with larger equipment.

6.3 Future Work

The work presented in this dissertation focuses on process development for new alloys in the DMLS process in terms of melt-pool geometry. Investigations are also done into the application of knowledge of powder effects in relationship to overhanging geometries and lattice structures. While this work represents substantial progress into understanding the effects of beam power, scan velocity, and powder in the DMLS process there are still room for significant development of the process. Some potential future research areas include:

- Effects of the inert gas on the production of overhanging structures. While the default gases used in the systems are argon and nitrogen, utilizing a gas such as helium or a welding gas mix could potentially increase conductivity of the powder greatly and improve surface finish.

- Effects of other processing parameters, such as scan strategy or hatch spacing. All of the strategies presented in this work have been nominal to the EOS L-PBF equipment, however other manufacturers use different parameter combinations, which may be more beneficial to surface finish, geometry, and microstructural control.
- Experimental verification of heating effects during production of overhanging geometries using high speed imaging and data acquisition. This, coupled with simulations, can help to determine optimal hatch spacing for overhanging structures to result in desired melt-pool geometry control.
- Investigation of the ability to control magnetism in the 17-4 alloy via manipulation of process parameters. This could have numerous industrial benefits such as logistics and robotics applications.
- Taking the results from the cellular lattice and overhang work and applying them to a real part geometry with a variety of geometric features.

References

[1] C. E. a. J. W. A. Sanders, "Industry 4.0 implies lean manufacturing: research activities in industry 4.0 function as enablers for lean manufacturing," *Journal of Industrial Engineering Management*, vol. 9, pp. 811-833, 2016.

[2] S. Ford and M. Despeisse, "Additive manufacturing and sustainability: an exploratory study of the advantages and challenges," *Journal of Cleaner Production*, vol. 137, pp. 1573-1587, 2016.

[3] I. Gibson, D. Rosen and B. Stucker, Additive Manufacturing Technologies 3D Printing, Rapid Prototyping, and Direct Digital Manufacturing, New York: Springer, 2010.

[4] N. Guo and M. C. Leu, "Additive manufacturing: technology, applications and research needs," *Frontiers of Mechanical Engineering*, vol. 8, no. 3, pp. 215-243, 3013.

[5] Electro Optical Systems, "EOS StainlessSteel GP1 for EOSINT M 270," 2015. [Online].

[6] Arcam AB, "EBM-Built Materials," [Online]. Available: http://www.arcam.com/technology/electron-beam-melting/materials/. [Accessed 6 June 2017].

[7] Optomec, "Component Repair," Optomec, [Online]. Available: https://www.optomec.com/3d-printed-metals/lens-core-applications/component-repair/. [Accessed 25 11 2017].

[8] Sciaky Inc., "Make Metal Parts Faster & Cheaper Than Ever with Electron Beam

Additive Manufacturing (EBAM) Systems and Services," Sciaky Inc., [Online]. Available: http://www.sciaky.com/additive-manufacturing/electron-beam-additive-manufacturing-technology. [Accessed 25 11 2017].

[9] M. J. Matthews, G. Guss, D. R. Drachenberg, J. A. Demuth, J. E. Heebner, E. B. Duoss, J. D. Kuntz and C. M. Spadaccini, "Diode-based additive manufacturing of metals using an optically-addressable light valve," *Optics Express,* vol. 25, no. 10, 15 May 2017.

[10] Special Metals Corporation, "Inconel Alloy 625 Datasheet," 2013. [Online].

[11] A. M. Anam, D. Pal and B. Stucker, "Modeling and experimental validation of nickel-based super alloy (Inconel 625) made using selective laser melting," in *Solid Freeform Fabrication Symposium,* Austin, TX, 2013.

[12] Kennametal, "High Temperature Machining Guide," [Online]. Available: http://www.kennametal.com/content/dam/kennametal/kennametal/common/Resources/Catalogs-Literature/Industry%20Solutions/SuperAlloys_material_machining_guide_Aerospace.pdf. [Accessed 2013].

[13] AK Steel, "17-4 PH Stainless Steel," [Online].

[14] J. Beuth, J. Fox, J. Gockel, C. Montgomery, R. Yang, H. Qiao, E. Soylemez, P. Reeseewatt, A. Anvari, S. Narra and N. Klingbeil, "Process Mapping for Qualification Across Multiple Direct Metal Additive Manufacturing Processes," in *SFF Proceedings*, Austin, TX, 2013.

[15] E. R. Denlinger, J. C. Heigel, P. Michaleris and T. A. Palmer, "Effect of inter-layer dwell time on distortion and residual stress in additive manufacturing of titanium and nickel alloys," *Journal of Materials Processing Technology,* vol. 215, pp. 123-131, 2015.

[16] A. S. Wu, D. W. Brown, M. Kumar, G. F. Gallegos and W. E. King, "An Experimental Investigation into Additive Manufacturing-Induced Residual Stresses in 316L Stainless Steel," *Metallurgical and Materials Transactions A,* vol. 45, no. 13, pp. 6260-6270, 2014.

[17] M. F. Zaeh and G. Branner, "Investigations on residual stresses and deformations in selective laser melting selective laser melting," *Production Engineering*, vol. 4, no. 1, pp. 35-45, 2010.

[18] N. T. Aboulkhair, N. M. Everitt, I. Ashcroft and C. Tuck, "Reducing porosity in AlSi10Mg parts processed by selective laser melting," *Additive Manufacturing,* Vols. 1-4, pp. 77-86, October 2014.

[19] J. Beuth and N. Klingbeil, "The Role of Process Variables in Laser-Based Direct Metal Solid Freeform Fabrication," *JOM,* pp. 36-39, 2001.

[20] A. Vasinota, J. L. Beuth and M. L. Griffith, "Process maps for laser deposition of thin-walled structures," in *Proceedings of 1999 Solid Freeform Fabrication Symposium*, Austin, TX, 1999.

[21] A. Vasinota, J. L. Beuth and M. L. Griffith, "Process maps for controlling residual stress and melt pool size in laser-based SFF processes," in *Proceedings of the 2000 Solid Freeform Fabrication Symposium*, Austin, TX, 2000.

[22] A. Vasinota, J. L. Beuth and R. Ong, "Melt pool size control in thin-walled and bulky parts via process maps," in *Proceedings of the 2001 Solid Freeform Fabrication Symposium*, Austin, TX, 2001.

[23] A. Vasinota, "Process Maps for Melt Pool Size and Residual Stress in Laser-based Solid Freeform Fabrication," Ph.D. Thesis, Carnegie Mellon University, 2002.

[24] S. Bontha, "The Effect of Process Variables on Microstructure in Laser-Deposited Materials," 2006.

[25] J. Gockel and J. L. Beuth, "Understanding Ti-6Al-4V Microstructure Control in Additive Manufacturing via Process Maps," in *Proceedings of the 2013 Solid Freeform Fabrication Symposium,* Austin, TX, 2013.

[26] S. M. Kelly and S. L. Kampe, "Microstructural evolution in laser-deposited multilayer Ti-6Al-4V builds: Part I. Microstructural characterization," *Metallurgical and Materials Transactions A,* vol. 35, no. 6, pp. 1861-1867, 2004.

[27] N. Hrabe and T. Quinn, "Effects of processing on microstructure and mechanical properties of a titanium alloy (Ti-6Al-4V) fabricated using electron beam melting (EBM), Part 2: Energy input, orientation, and location," *Materials Science and Engineering: A,* pp. 271-277, 2013.

[28] S. Bontha and N. Klingbeil, "Thermal Process Maps for Controlling Microstructure in Laser-Based Solid Freeform Fabrication," in *Proceedings of the 2003 Solid Freeform Fabrication Symposium,* Austin, TX, 2003.

[29] A. Birnbaum, P. Aggarangsi and J. L. Beuth, "Process Scaling and Transient Melt Pool Size Control in Laser-Based Additive Manufacturing Processes," in *Proceedings of the 2003 Solid Freeform Fabrication Symposium,* Austin, TX, 2003.

[30] P. Aggarangsi, "Transient Melt Pool Size and Stress Control in Additive Manufacturing Processes," PhD Thesis, Carnegie Mellon University, 2006.

[31] J. C. Fox, "Transient Melt Pool Response in Additive Manufacturing Processes," PhD Thesis, Carnegie Mellon University, 2015.

[32] D. Clymer, J. Beuth and J. Cagan, "Additive Manufacturing Process Design," in *Solid Freeform Fabrication Symposium*, Austin, TX, 2016.

[33] P. A. Kobryn and S. L. Semiatin, "The Laser Additive Manufacture of Ti-6Al-4V," *Journal of Materials,* pp. 40-42, 2001.

[34] P. Kobryn and S. Semiatin, "Microstructure and Texture Evolution During Solidification Processing of Ti-6Al-4V," *Journal of Materials Processing Technology,,* vol. 13, pp. 330-339, 2003.

[35] S. Bontha, C. Brown, D. Gaddam, N. W. Klingbeil, P. A. Kobryn, H. L. Fraser and J. W. Sears, "Effects of Process Variables and Size Scale on Solidification Microstructure in Laser-Based Solid Freeform Fabrication of Ti-6Al-4V," in *Solid Freeform Fabrication Symposium*, Austin, TX, 2004.

[36] S. Bontha, N. Klingbeil, P. Kobryn and H. L. Fraser, "Effects of Process Variables and Size Scale on Solidification Microstructure in Beam-Based Fabrication of Bulky 3D

Structures," *Material Science and Engineering*, vol. 513, pp. 311-318, 2009.

[37] J. Gockel, "Integrated Control of Solidification Microstructure and Melt Pool Dimensions in Additive Manufacturing of Ti-6Al-4V," Carnegie Mellon University, PhD Thesis, 2014.

[38] S. P. Narra, R. Cunningham, J. Beuth and A. D. Rollett, "Location Specific Solidification Microstructure Control in Electron Beam Melting of Ti-6Al-4V," *Additive Manufacturing*, p. In Press, 2017.

[39] S. P. Narra, R. Cunningham, D. Christiansen, J. Beuth and A. D. Rollett, "Toward Enabling Spatial Control of Ti-6Al-4V Solidification Microstructure in the Electron Beam Melting Process," in *Solid Freeform Fabrication Symposium*, Austin, TX, 2015.

[40] L. N. Carter, C. Martin, P. J. Withers and M. M. Attallah, "The influence of the laser scan strategy on grain structure and cracking behaviour in SLM powder-bed fabricated nickel superalloy," *Journal of Alloys and Compounds*, vol. 615, pp. 338-347, 2014.

[41] D. Rosenthal, "The Theory of Moving Sources of Heat and Its Applications to Metal Treatments," *Transactions of ASME*, vol. 68, pp. 849-866, 1946.

[42] R. D. a. D. Dobranich, "Analytical Thermal Models for the LENS Process," Sandia National Laboratories Internal Report, 1998.

[43] R. Dykhuizen and D. Dobranich, "Cooling Rates in the LENS Process," Sandia National Laboratories Internal Report, 1998.

[44] T. W. Eagar and N. S. Tsai, "Temperature Fields Produced by Traveling Distributed Heat Sources," *Welding Research Supplement,* pp. 346-355, 1983.

[45] P. Michaleris, "Modeling metal deposition in heat transfer analyses of additive manufacturing processes," *Finite Elements in Analysis and Design,* vol. 86, pp. 51-60, 2014.

[46] J. K. Peter Mercelis, "Residual stresses in selective laser sintering and selective laser melting," *Rapid Prototyping Journal,* vol. 12, no. 5, pp. 254-265, 2006.

[47] P. Aggarangsi and J. L. Beuth, "Localized Preheating Approaches for Reducing Residual Stress in Additive Manufacturing," in *Solid Freeform Fabrication Symposium Conference Proceedings,* Austin, TX, 2006.

[48] I. A. Roberts, C. J. Wang, R. Esterlein, M. Stanford and D. J. Mynors, "A three-dimensional finite element analysis of the temperature field during laser melting of metal powders in additive layer manufacturing," *International Journal of Machine Tools and Manufacture*, vol. 49, no. 12-13, pp. 916-923, 2009.

[49] P. Nie, O. A. Ojo and Z. Li, "Numerical modeling of microstructure evolution during laser additive manufacturing of a nickel-based superalloy," *Acta Materialia,* vol. 77, pp. 85-95, 2014.

[50] S. M. Kelly, "Thermal and Microstructure Modeling of Metal Deposition Processes with Application to Ti-6Al-4V," Virginia Polytechnic Institute and State University, 2004.

[51] C. K. Gong X, " Phase-field modeling of microstructure evolution in electron beam additive," *Journal of Materials,* vol. 67, pp. 1176-1182, 2015.

[52] B. A. R. A. K. C. Markl M, "Numerical investigations of selective electron beam melting on the powder scale," in *2016*, Proceedings Fraunhofer Direct Digital Manufacturing Conference.

[53] H. H. K. C. Rai A, "Simulation of grain structure evolution during powder bed based additive manufacturing," *Additive Manufacturing,* 2016.

[54] M. M. K. C. Rai A, "A coupled cellular automaton–lattice Boltzmann model for grain structure simulation during additive manufacturing," *Computational Material Science,* 2016.

[55] L. F. S. W. N. J. F. Z. e. a. Zhang J, "Probabilistic simulation of solidification microstructure evolution during laser-based metal deposition," in *Proceedings of the International Solid Freeform Fabrication Symposium,* Austin, TX, 2013.

[56] A. Zinoviev, O. Zinovieva, V. Ploshikhin, V. Romanova and R. Balokhonov, "Evolution of Grain Structure During Laser Additive Manufacturing. Simulation by a Cellular Automata Method," *Materials and Design,* vol. 106, pp. 321-329, 2016.

[57] T. Chen and Y. Zhang, "Thermal modeling of metal powder-based selective laser sintering," in *Solid Freeform Fabrication Symposium 2005 Conference Proceedings*, Austin, TX, 2005.

[58] X. C. Wang, T. Laoui, J. Bonse, J. P. Kruth, B. Lauwers and L. Froyen, "Direct selective laser sintering of hard metal powders: experimental study and simulation," *International Journal of Advanced Manufacturing Technology*, vol. 19, pp. 351-357, 2002.

[59] M. Matsumoto and M. Shiomi, "Finite element analysis of single layer forming on metallic powder bed in rapid prototyping by selective laser processing," *International Journal of Machine Tools and Manufacture*, vol. 42, no. 1, pp. 61-67, 2002.

[60] N. E. Hodge, R. M. Ferencz and J. M. Solberg, "Implementation of a thermomechanical model for the simulation of selective laser melting," *Computational Mechanics*, vol. 54, pp. 33-51, 2014.

[61] W. E. King, A. T. Anderson, R. M. Ferencz, N. E. Hodge, C. Kamath, S. A. Khairallah and A. M. Rubenchik, "Laser powder bed fusion additive manufacturing of metals; physics, computational, and materials challenges," *Applied Physics Reviews,* 2015.

[62] S. A. Khairallah, A. T. Anderson, A. Rubenchik and W. King, "Laser powder-bed fusion additive manufacturing: physics of complex melt flow and formation mechanisms of pores, spatter, and denudation zones," LLNL.

[63] I. Yadroitsev, A. Gusarov, I. Yadroitsava and I. Smurov, "Single track formation in selective laser melting of metal powders," *Journal of Materials Processing Technology,* vol. 210, pp. 1624-1631, 2010.

[64] D. Dobranich and R. C. Dykhuizen, "Scoping Thermal Calculations of the LENS Process," Sandia National Laboratories, Albuquerque, NM, 1998.

[65] N. Karapatis, "A sub-process approach of selective laser sintering," in *Thesis N2506*, EPFL, 2002.

[66] W. J. Sames, "Additive Manufacturing of Inconel 718 Using Electron Beam Melting: Processing, Post-Processing, & Mechanical Properties," 2015.

[67] A. J. Pinkerton and L. Li, "Rapid prototyping using direct laser deposition: The effect of powder atomisation type and flow rate," *Journal of Engineering Manufacture,* vol. 217, pp. 741-752, 2003.

[68] J. Gan, Z. Zhou and A. Yu, "Effect of particle shape and size on effective thermal conductivity of packed beds," *Powder Technology,* vol. 311, pp. 157-166, 2017.

[69] J. A. Slotwinski, E. J. Garboczi, P. E. Stutzman, C. F. Ferraris, S. S. Watson and M. A. Peltz, "Characterization of Metal Powders Used for Additive Manufacturing," *Journal of Research of the National Institute of Standards and Technology,* vol. 119, 2014.

[70] L. C. Wei, "New Studies on Thermal Transport in Metal Additive Manufacturing Processes and Products," Carnegie Mellon University, Pittsburgh, PA, 2017.

[71] S. Yagi and D. Kunii, "Studies on effective thermal conductivities in packed beds," *AIChE,* vol. 3, no. 3, pp. 373-381, 1957.

[72] D. L. Swift, "The thermal conductivity of spherical metal powders including the effect of an oxide coating," *International Journal of Heat and Mass Transfer,* vol. 9, no. 10, pp. 1061-1074, 1966.

[73] H. W. Godbee and W. T. Ziegler, "Thermal conductivities of mgo, al2o3, and zro2 powders to 850c. ii. theoretical," *Journal of Applied Physics,* vol. 37, no. 56, 1966.

[74] I. Nozad, R. G. Carbonell and S. Whitaker, "Heat conduction in multiphase systems—II: Experimental method and results for three-phase systems," *Chemical Engineering Science,* vol. 40, no. 5, pp. 857-863, 1985.

[75] G. R. Hadley, "Thermal conductivity of packed metal powders," *International Journal of Heat and Mass Transfer,* vol. 29, no. 6, pp. 909-920, 1986.

[76] S. S. Sih and J. W. Barlow, "Measurement and Prediction of the Thermal Conductivity of Powders at High Temperatures," in *Solid Freeform Fabrication Symposium*, Austin, TX, 1994.

[77] S. S. Sih and J. W. Barlow, "The prediction of the thermal conductivity of powders," in *Solid Freeform Fabrication Symposium*, Austin, TX, 1995.

[78] P. Zehner and E. U. Schlünder, "Thermal conductivity of beds at moderate temperatures," *Chemical Engineering Technology,* vol. 42, no. 14, pp. 933-941, 1970.

[79] K. Bala, P. R. Pradhan, N. S. Saxena and M. P. Saksena, "Effective thermal conductivity of copper powders," *Journal of Physics D: Applied Physics*, vol. 22, no. 8, pp. 1068-1072, 1989.

[80] A. V. Gusarov and E. P. Kovalev, "Model of thermal conductivity in powder beds," *Physical Review B,* pp. 80-95, 2009.

[81] A. V. Gusarov, I. Yadroitsev, P. Bertrand and I. Smurov, "Model of Radiation and Heat Transfer in Laser-Powder Interaction Zone at Selective Laser Melting," *Journal of Heat Transfer*, vol. 131, no. 7, 2009.

[82] P. Fischer, V. Romano, H. P. Weber, N. P. Karaptis, E. Boillat and R. Glardon, "Sintering of commercially pure titanium powder with a Nd:YAG laser source," *Acta Materialia*, vol. 51, no. 6, pp. 1651-1662, 2003.

[83] J. -P. Kruth, G. Levy, F. Klocke and T. H. C. Childs, "Consolidation phenomena in laser and powder-bed powder based layered manufacturing," *Annals of the CIRP*, vol. 56, no. 2, pp. 730-759, 2007.

[84] F. Calignano and D. Manfredi, "Production of overhanging structures by DMLS," in *High value manufacturing*, Torino, Italy, Taylor & Francis Group, 2014, pp. 61-64.

[85] D. Wang, Y. Yang, M. Zhang, J. Lu, R. Liu and D. Xiao, "Study on SLM fabrication of Precision Metal Parts with Overhanging Structures," in *Proceedings 2013 IEEE International Symposium on Assembly and Manufacturing (ISAM)*, Xi'an, 2013.

[86] G. Strano, L. Hao, R. M. Everson and K. E. Evans, "Surface roughness analysis, modelling and prediction in selective laser melting," *Journal of Materials Processing Technology*, vol. 213, no. 4, pp. 589-597, 2013.

[87] L. Thijs, F. Verhaeghe, T. Craeghs, J. V. Humbeeck and J. P. Kruth, "A study of the micro structural evolution during selective laser melting of Ti-6Al-4V," *Acta Mater*, vol. 58, no. 9, pp. 3303-3312, 2010.

[88] J. C. Fox, S. P. Moylan and B. M. Lane, "Effect of process parameters on the surface roughness of overhanging Effect of process parameters on the surface roughness of overhanging," in *3rd CIRP Conference on Surface Integrity*, 2016.

[89] J. Banhart, "Manufacturing Routes for Metallic Foams," *Journal of Materials,* vol. 52, no. 12, pp. 22-27, 2000.

[90] G. J. Davies and S. Zhen, "Metallic foams: their production, properties and applications," *Journal of Materials Science,* vol. 18, no. 7, pp. 1899-1911, 1983.

[91] A. Y. Hussein, "The Development of Lightweight Cellular Structures for Metal Additive Manufacturing," PhD. Thesis, University of Exeter, 2013.

[92] M. Salmi, J. Tuomi, K.-S. Paloheimo, R. Björkstrand, M. Paloheimo, J. Salo, R. Kontio, K. Mesimäki and A. A. Mäkitie, "Patient-specific reconstruction with 3D modeling and DMLS additive manufacturing," *Rapid Prototyping Journal,* vol. 18, no. 3, pp. 209-214, 2012.

[93] I. A. Aziz, "Direct Metal Laser Sintering of Titanium Implant with Tailored Structure and Mechanical Properties," PhD. Thesis, The University of Waikato, 2014.

[94] S. Zhang, S. Dilip, L. Yang, H. Miyanaji and B. Stucker, "Property evaluation of metal cellular strut structures via powder bed fusion AM," in *Solid Freeform Fabrication Symposium*, Austin, TX, 2015.

[95] C. Yan, L. Hao, A. Hussein and D. Raymont, "Evaluations of cellular lattice structures manufactured using selective laser melting," *International Journal of Machine Tools &*

Manufacture, vol. 62, pp. 32-38, 2012.

[96] C. Yan, L. Hao, A. Hussein, S. L. Bubb, P. Young and D. Raymont, "Evaluation of light-weight AlSi10Mg periodic cellular lattice structures fabricated via direct metal laser sintering," *Journal of Materials Processing Technology,* vol. 214, pp. 856-864, 2014.

[97] M. Santorinaios, W. Brooks, C. J. Sutcliffe and R. A. Mines, "Crush behavior of open celular lattice structures manufactured using selective laser melting," *High Performance Structures and Materials III,* vol. 85, pp. 481-490, 2006.

[98] E. Soylemez, J. L. Beuth and K. Taminger, "Controlling Melt Pool Dimensions Over a Wide Range of Material Deposition Rates in Electron Beam Additive Manufacturing," in *Solid Freeform Fabrication Proceedings,* Austin, TX, 2010.

[99] P. Y. Peretyagin, I. V. Zhirnov, Y. G. Vladimirov, T. V. Tarasova and A. A. Okun'kova, "Track Geometry in Selective Laser Melting," *Russian Engineering Research,* vol. 35, no. 6, pp. 473-476, 2015.

[100] Simulia, "2.11.1 Uncoupled heat transfer analysis," in *Abaqus Theory Manual*, 2016.

[101] G. Jacob, A. Donmez, J. Slotwinski and S. Moylan, "Measurement of powder bed density in powder bed fusion additive manufacturing processes," *Measurement Science and Technology,* vol. 27, no. 11, 2016.

[102] G. Bugeda, M. Cervera and G. Lombera, "Numerical prediction of temperature and density distributions in selective laser sintering processes," *Rapid Prototyping Journal,*

vol. 5, no. 1, pp. 21-26, 1999.

[103] C. Sainte-Catherine, M. Jeandin, D. Kechemair and J.-P. Ricaud, "Study of Dynamic Absorptivity at 10.6um (CO2) and 1.06um (Nd-YAG) Wavelengths as a Function of Temperature," *Journal De Physique IV,* vol. 1, no. C7, pp. 151-157, 1991.

[104] S. Ly, A. M. Rubenchik, S. A. Khairallah, G. Guss and M. J. Matthews, "Metal vapor micro-jet controls material redistribution in laser powder bed fusion additive manufacturing," Nature, 2017.

[105] J. F. Lancaster, "The Physics of Welding," *Physics Technology,* vol. 15, pp. 73-79, 1984.

[106] S. Pang, W. Chen and W. Wang, "A Quantitative Model of Keyhole Instability Induced Porosity in Laser Welding of Titanium Alloy," *Metallurgical and Materials Transactions A,* vol. 45, no. 6, pp. 2808-2818, 2014.

[107] R. Rai, J. W. Elmer, T. A. Palmer and T. DebRoy, "Heat transfer and fluid flow during keyhole mode laser welding of tantalum, Ti-6Al-4V, 304L stainless steel and vanadium," *Journal of Physics D: Applied Physics,* vol. 40, pp. 5753-5766, 2007.

[108] Z. Francis, "The Effects of Laser and Electron Beam Spot Size in Additive Manufacturing Processes," PhD Thesis, Carnegie Mellon University, Pittsburgh, PA, 2017.

[109] J. Trapp, A. M. Rubenchik, G. Guss and M. J. Matthews, "In situ absorptivity measurements of metallic powders during laser powder-bed fusion additive manufacturing," *Applied Materials Today,* vol. 9, pp. 341-349, 2017.

[110] S. P. Narra, "Melt Pool Geometry and Microstructure Control across Alloys in Metal Based Additive Manufacturing Processes," Carnegie Mellon University, Pittsburgh, 2017.

[111] W. M. Steen, Laser Material Processing, London: Springer, 2003, p. 72.

[112] N. R. Comins, "The optical properties of liquid metals," *The Philosophical Magazine: A Journal of Theoretical Experimental and Applied Physics,* vol. 25, no. 4, pp. 817-831, 1972.

[113] G. Shannon, "Laser welding modes: conduction, transition, & keyhole welding," Amada Miyachi, 19 Jan 2016. [Online]. Available: http://info.amadamiyachi.com/blog/conduction-transition-and-keyhole-welding-modes. [Accessed 4 Jun 2017].

[114] M. Tang and C. P. Pistorius, "Oxides, porosity and fatigue performance of AlSi10Mg parts produced by selective laser melting," *International Journal of Fatigue,* vol. 94, no. 2, pp. 192-201, 2017.

[115] D. B. F. B. H. M. F. B. M. Agarwala, "Direct selective laser sintering of metals," *Rapid Prototyping Journal,* vol. 1, no. 1, pp. 26-36, 1995.

[116] Y. Su, K. C. Mills and A. Dinsdale, "A model to calculate surface tension of commercial alloys," *Journal of Materials Science,* vol. 40, pp. 2185-2190, 2005.

[117] Lucefin, *Structure.*

[118] R. Cunningham, S. P. Narra, C. Montgomery, J. Beuth and A. D. Rollett, "Synchrotron-

Based X-ray Microtomography Characterization of the Effect of Processing Variables on Porosity Formation in Laser Power-Bed Additive Manufacturing of Ti-6Al-4V," *JOM*, vol. 69, no. 3, pp. 479-484, 2017.

[119] K. D. Ramkumar, Patel, S. Sri Praveen, Choudhury, Prabaharan, N. Arivazhagan and A. M. Xavior, "Influence of filler metals and welding techniques on the structure-property relationships of Inconel 718 and AISI 316L dissimilar weldments," *Materials and Design*, vol. 62, pp. 175-188, 2014.

[120] Stratasys Direct Inc., "Inconel 625 Direct Metal Laser Sintering Material Specifications," Stratasys Direct Inc., 2015.

[121] C. Hall and W. D. Hoff, Water Transfer in Brick, Stone, and Concrete, Boca Raton: Taylor and Francis, 2002.

[122] PWC, "3D Printing and the New Shape of Industrial Manufacturing," PricewaterhouseCoopers LLP, Delaware, 2014.

[123] K. M. Taminger, R. A. Hafley and D. L. Dicus, "Solid Freeform Fabrication: An Enabling Technology for Future Space Missions," in *Keynote Lecture for 2002 International Conference on Metal Powder Deposition for Rapid Manufacturing*, San Antonio, TX, April 8-10, 2002.

[124] K. M. Taminger and R. A. Hafley, "Electron Beam Freeform Fabrication for Cost Effective Near-Net Shape Manufacturing," in *NATO/RTOAVT-139 Specialist' Meeting on Cost Effective Manufacture via Net Shape Processing*, Amsterdam, Netherlands, 2006.

[125] J. W. Sears, "Direct Laser Powder Deposition- "State of the Art"," Schenectady, New York, 1999.

[126] A. B. Speirings, N. Herres and G. Levy, "Influence of the particle size distribution on surface quality and mechanical properties in additive manufacttured stainless steel parts," in *SFF*, Austin, TX, 2010.

[127] R. Grylls, "Laser Engineered Net Shapes," *Advanced Materials and Processes*, p. p. 45, 2003.

[128] C. K. Chua, K. F. Leong and C. S. Lim, Rapid Prototyping: Principles and Applications, 3rd ed., Hackensack, NJ: World Scientific Publishing Co. Pte. Ltd., 2010.

[129] J. -P. Kruth, B. Vandenbroucke, J. Van Vaerenbergh and P. Mercelis, "Benchmarking of Different SLS/SLM Processes as Rapid Manufacturing Techniques," in *Int. Conf. Polymers & Moulds Innovations (PMI)*, Gent, Belgium, 2005.

[130] Electro Optical Systems, "EOS M280 Datasheet," 2013. [Online]. Available: http://ip-saas-eos-cms.s3.amazonaws.com/public/b1a64caa0c54d208/bc2d30d3f7b4b821634dfafa303ee441/systemdatasheet_M280.pdf.

[131] G. Dongdong and S. Yifu, "Balling phenomena in direct laser sintering of stainless steel powder: Metallurgical mechanisms and control methods," *Materials and Design*, vol. 30, pp. 2903-2910, 2009.

[132] S. Rengers, "Electron Beam Melting vs Direct Metal Laser Sintering," 2012.

[133] L. E. Murr, S. M. Gaytan, D. A. Ramirez, E. Martinez, J. Hernandez, K. N. Amato, P. W. Shindo, F. R. Medina and R. B. Wicker, "Metal fabrication by additive manufacturing using laser and electron beam melting technologies," *JMST,* vol. 28, no. 1, pp. 1-14, 2012.

[134] E. Santos, F. Abe, Y. Kitamura, K. Osakada and M. Shiomi, "Mechanical properties of pure titanium models processed by selective laser melting," in *SFF,* Austin, TX, 2002.

[135] A. T. A. A. R. W. E. K. S. A. Khairallah, "Laser powder-bed fusion additive manufacturing: Physics of complex melt flow and formation mechanisms of pores, spatter, and denudation zones," *Acta Mater,* vol. 108, pp. 36-45, 2016.

[136] G. G. S. A. K. A. M. R. P. J. D. W. E. K. M. J. Matthews, "Denudation of metal powder layers in laser powder bed fusion processes," *Acta Mater,* vol. 114, pp. 33-42, 2016.

[137] P. A. K. a. S. L. Semiatin, "The Laser Additive Manufacture of Ti-6Al-4V," *Journal of Materials*, pp. 40-42, 2001.

[138] EOS GmbH, "Materials for Metal Additive Manufacturing," [Online]. Available: http://www.eos.info/materials-m. [Accessed 6 June 2017].

[139] V. Shankar, K. B. S. Rao and S. L. Mannan, "Microstructure and mechanical properties of Inconel 625 superalloy," *Journal of Nuclear Materials*, vol. 288, no. 2-3, pp. 222-232, 2001.

[140] EOS GmbH, "Additive Manufacturing, Laser-Sintering and industrial 3D printing -

Benefits and Functional Principle," Electro Optical Systems GmbH, [Online]. Available: https://www.eos.info/additive_manufacturing/for_technology_interested. [Accessed 10 6 2017].

[141] N. T. Aboulkhair, I. Maskery, C. Tuck, I. Ashcroft and N. M. Everitt, "On the formation of AlSi10Mg single tracks and layers in selective laser melting: microstructure and nano-mechanical properties," *Journal of Materials Processing Technology*, vol. 230, pp. 88-98, 2016.

Appendix A: Polishing and Etching Procedures

IN625 Polishing and Etching

	Surface	Abrasive/Size	Load (lbs)	Base Speed (rpm) and direction	Time (min:sec)
Polishing	CarbiMet 2	240 Grit SiC water cooled	6	300 >>	Until Plane
	Apex Hercules S	9-µm MetaDi Supreme Diamond	6	150 ><	5:00
	TriDent	3-µm MetaDi Supreme Diamond	6	150 >>	5:00
	ChemoMet	0.05-µm MasterMet Colloidal Silica	6	150 ><	2:00
	>> Denotes complimentary motion between specimen holder and platen >< Denotes contra motion				
Etching	**Oxalic Acid Etchant**				
	Chemical	**Amount**			
	Distilled Water	10% wt.			
	Oxalic Acid	90% wt.			
	Procedure: Electroetch samples at 1A for 30-60 seconds				

17-4 Stainless Steel Polishing and Etching

	Surface	Abrasive/Size	Load (lbs)	Base Speed (rpm) and direction	Time (min:sec)
Polishing	CarbiMet 2	320 Grit SiC water cooled	6	300 >>	Until Plane
	UltraPol Cloth	9-µm MetaDi Supreme Diamond	6	150 ><	5:00
	TriDent	3-µm MetaDi Supreme Diamond	6	150 >>	3:00
	MicroCloth	0.05-µm MasterMet Colloidal Silica	6	150 ><	2:00
	>> Denotes complimentary motion between specimen holder and platen >< Denotes contra motion				
Etching	**Oxalic Acid Etchant**				
	Chemical	**Amount**			
	Distilled Water	10% wt.			
	Oxalic Acid	90% wt.			
	Procedure: Electroetch samples at 1A for 90-120 seconds				

Appendix B: Effect of Powder Layer Thickness on Melt-Pool Width

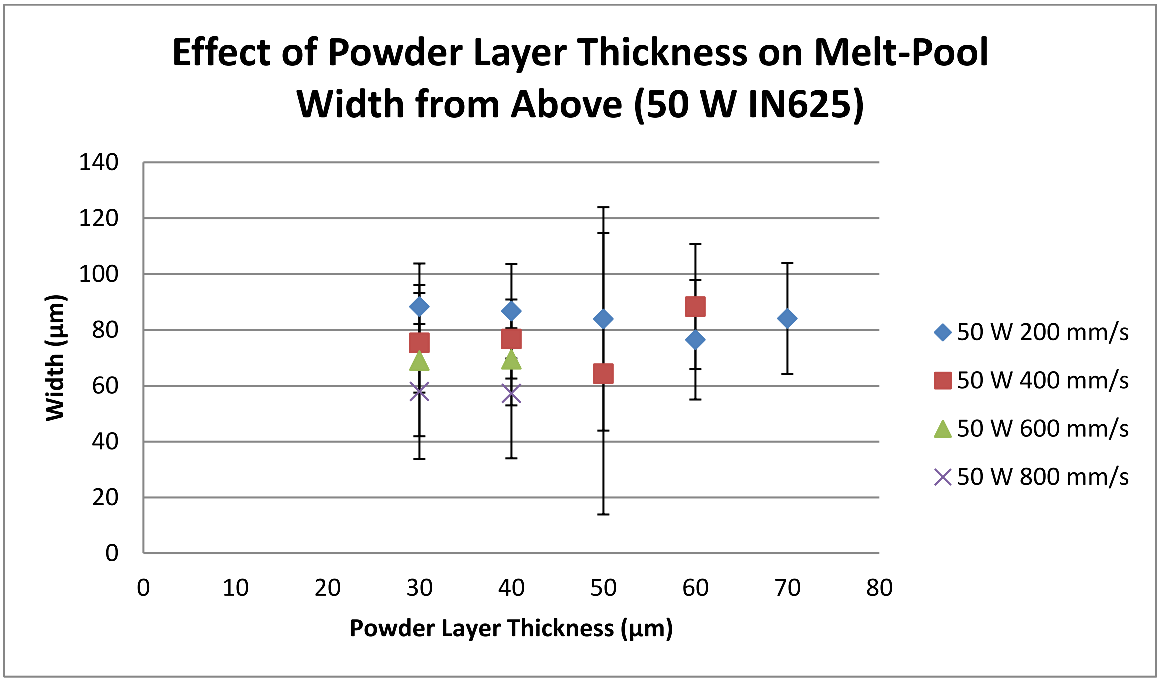

Appendix Figure 1: Effect of powder layer thickness on IN625 melt-pool width from above (50 W)

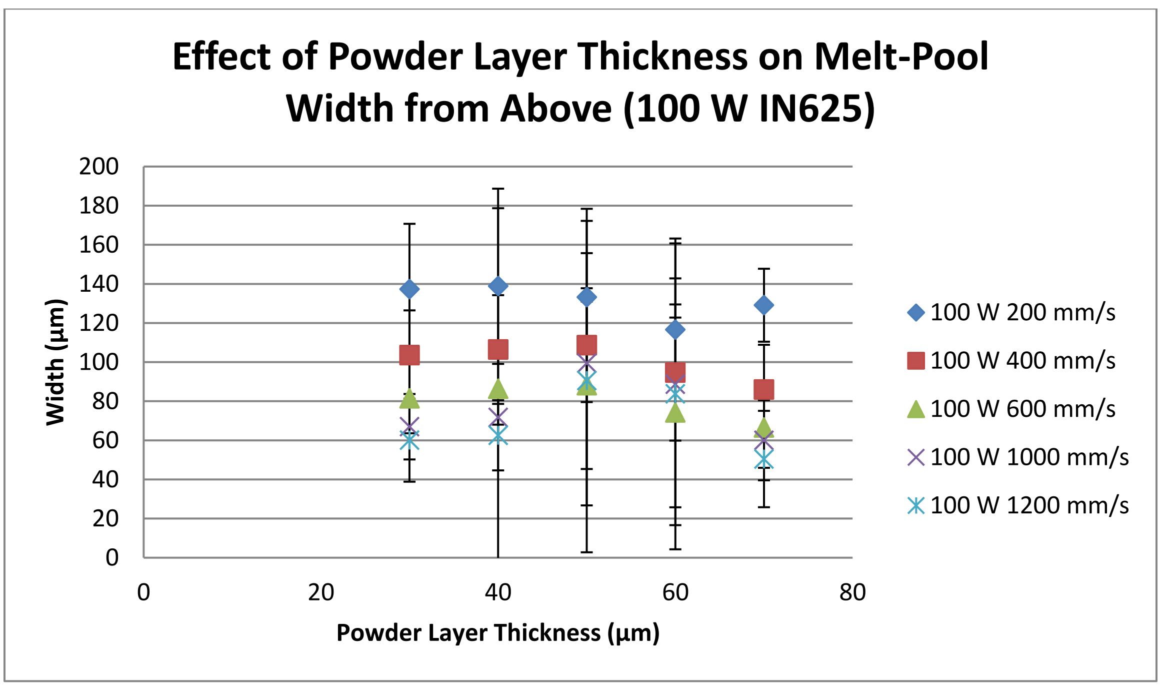

Appendix Figure 2: Effect of powder layer thickness on IN625 melt-pool width from above (100 W)

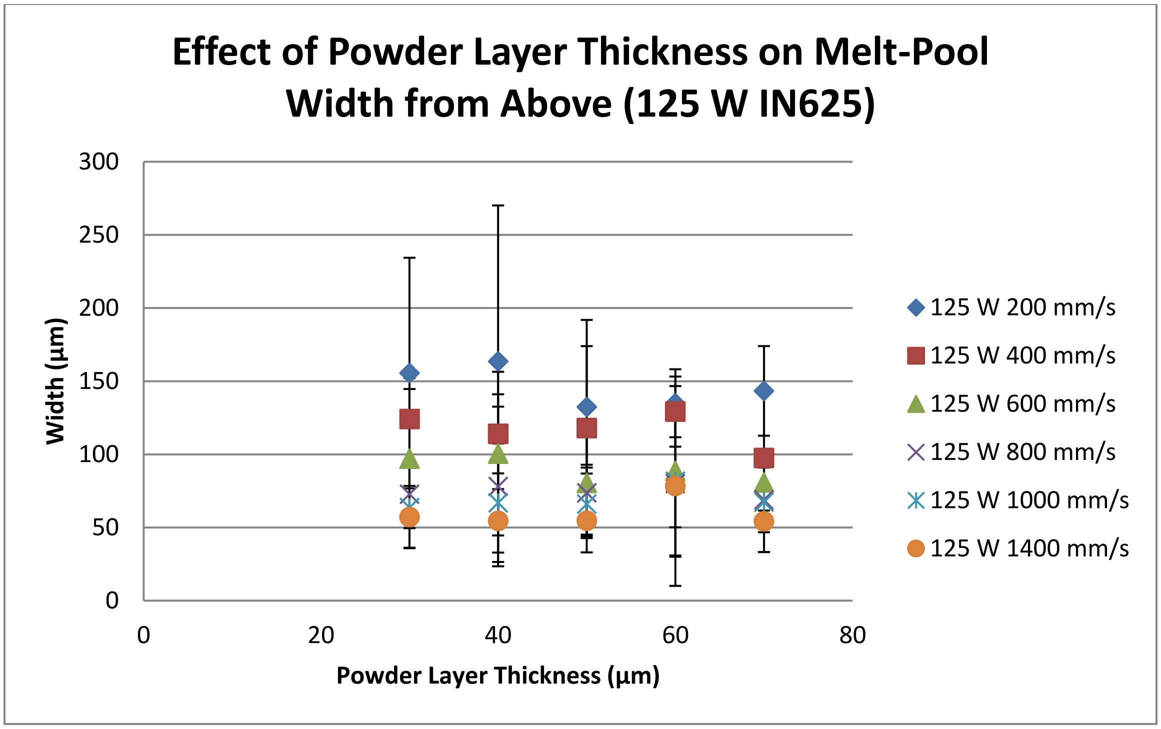

Appendix Figure 3: Effect of powder layer thickness on IN625 melt-pool width from above (125 W)

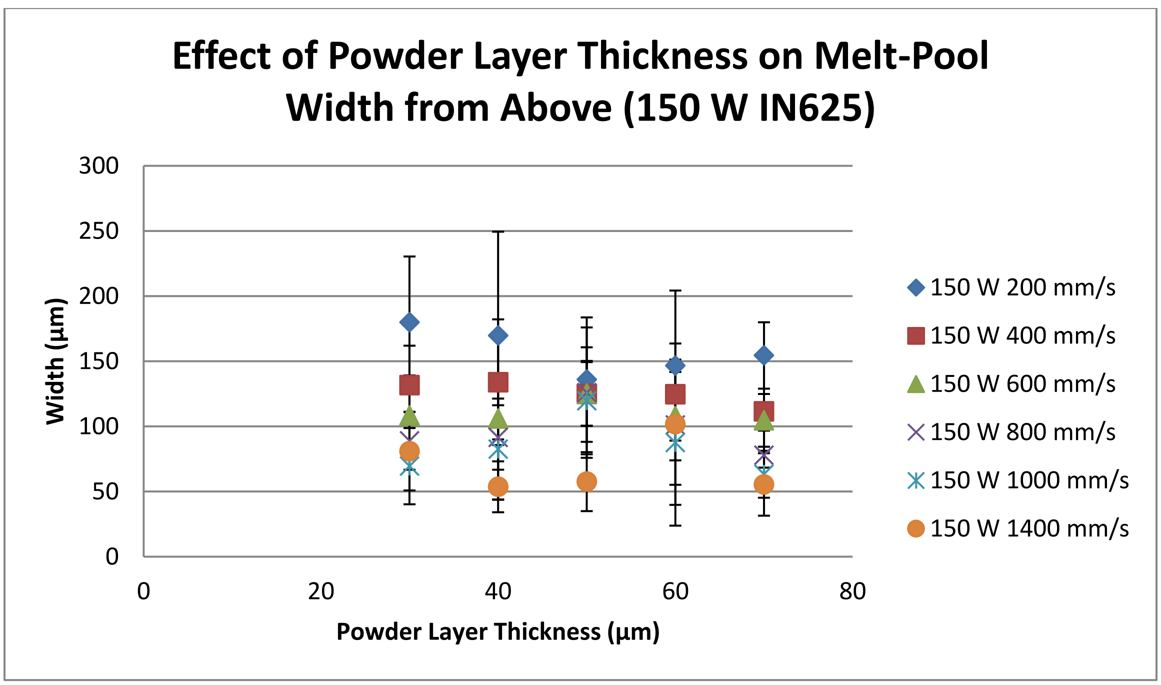

Appendix Figure 4: Effect of powder layer thickness on IN625 melt-pool width from above (150 W)

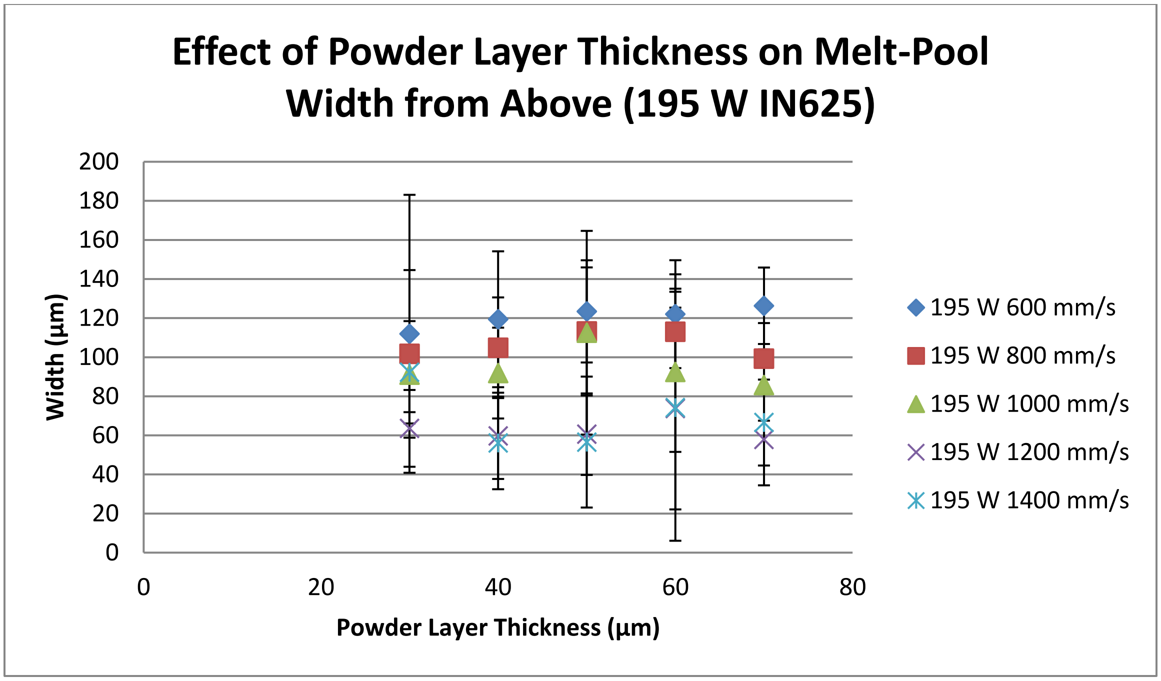

Appendix Figure 5: Effect of powder layer thickness on IN625 melt-pool width from above (195 W)

Appendix C: Effect of Powder Layer Thickness on Melt-Pool Depth

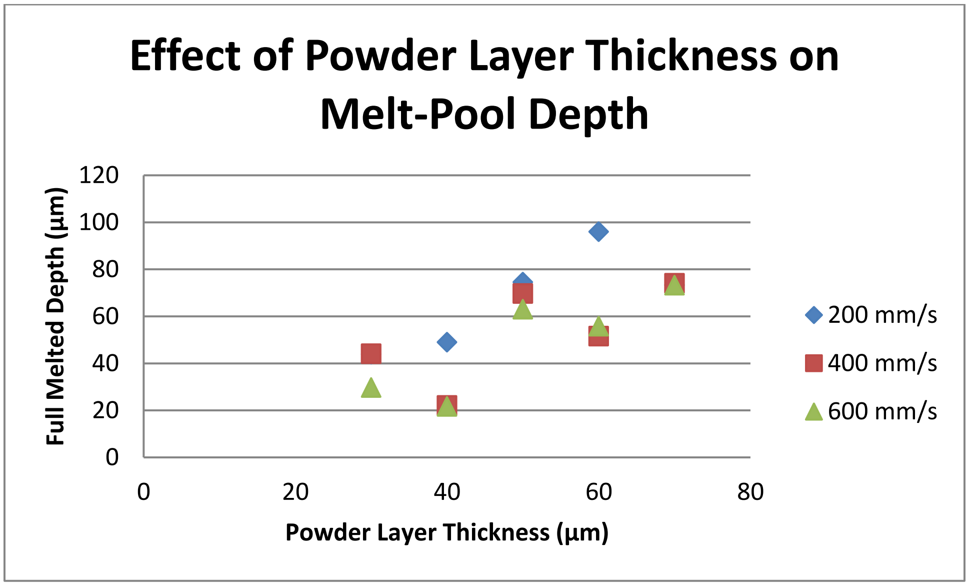

Appendix Figure 6: Effect of melt-pool depth with increasing layer thickness for 50 W

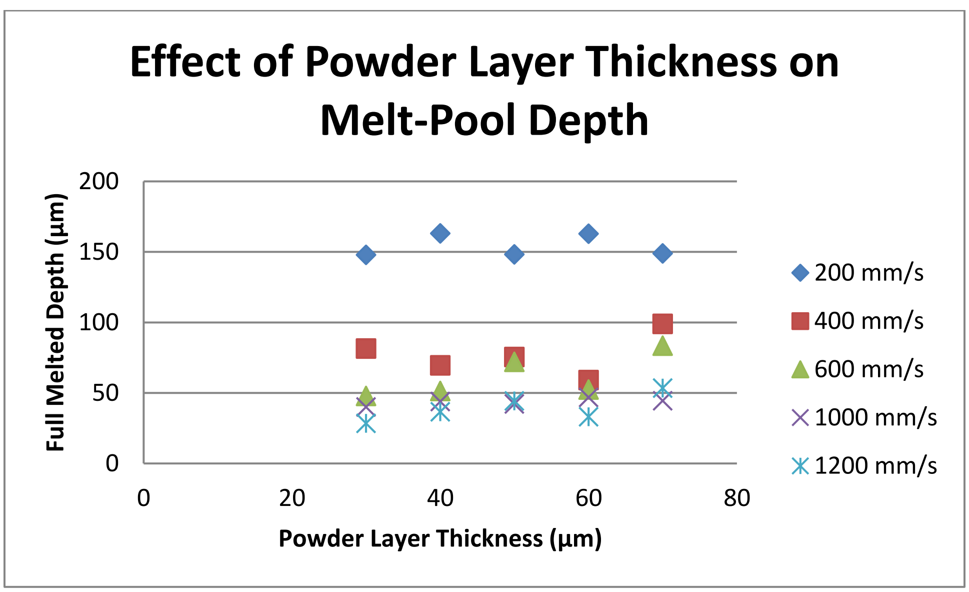

Appendix Figure 7: Effect of melt-pool depth with increasing layer thickness for 100 W

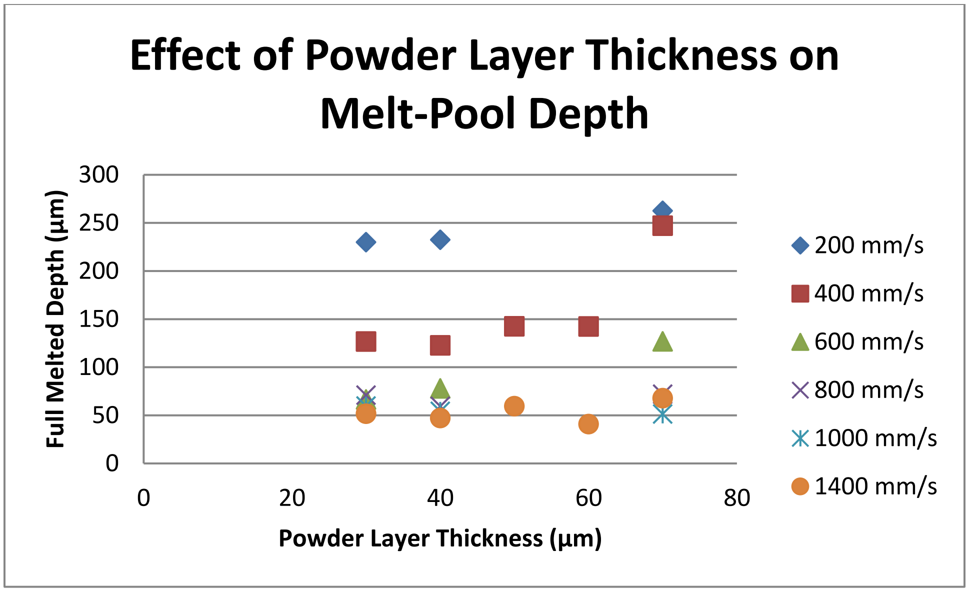

Appendix Figure 8: Effect of melt-pool depth with increasing layer thickness for 125 W

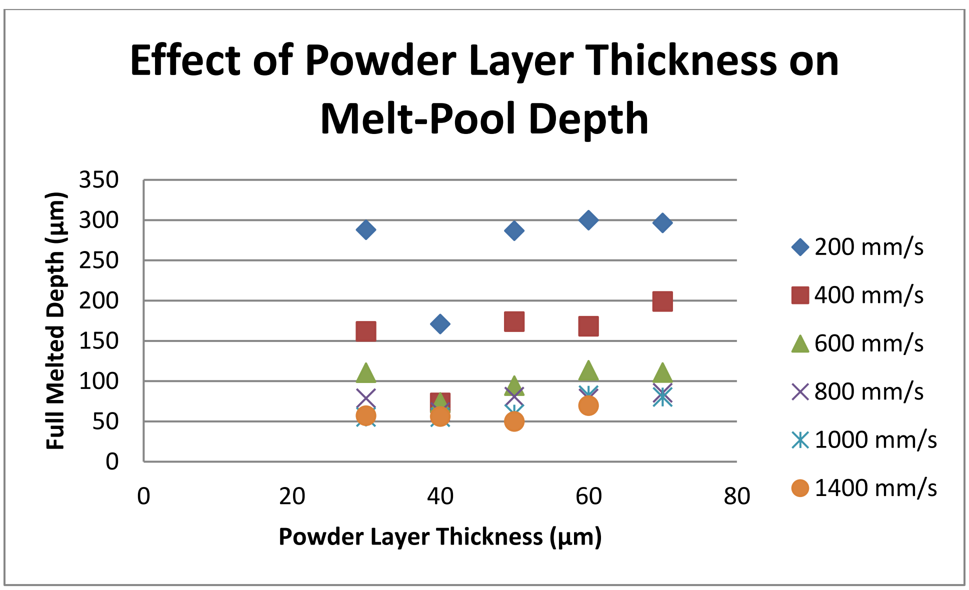

Appendix Figure 9: Effect of melt-pool depth with increasing layer thickness for 150 W

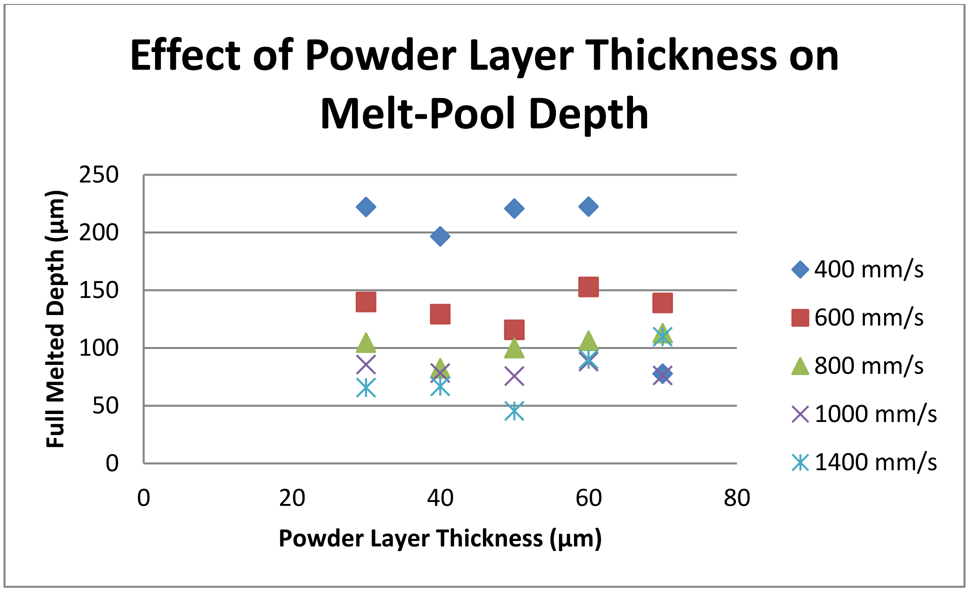

Appendix Figure 10: Effect of melt-pool depth with increasing layer thickness for 175 W